STRAIN ACTUATED AEROELASTIC CONTROL

Charrissa Y. Lin

B.S., Aeronautics and Astronautics
Massachusetts Institute of Technology, 1990

Submitted to the Department of Aeronautics and Astronautics
in Partial Fulfillment of the Requirements for the Degree of

MASTER OF SCIENCE in AERONAUTICS AND ASTRONAUTICS

at the

MASSACHUSETTS INSTITUTE OF TECHNOLOGY

February 1993

Signature of Author _____
Department of Aeronautics and Astronautics
January 15, 1993

Certified by _____
Professor Edward F. Crawley
Department of Aeronautics and Astronautics
Mac Vicar Faculty Fellow
Thesis Advisor

Accepted by _____
Professor Harold Y. Wachman
Chairman, Department Graduate Committee

STRAIN ACTUATED AEROELASTIC CONTROL
by

CHARRISSA Y. LIN

Submitted to the Department of Aeronautics and Astronautics
on January 15, 1993 in partial fulfillment of the requirements
for the Degree of Master of Science in Aeronautics and
Astronautics

ABSTRACT

The preliminary design of a wing with strain actuation and conventional flap actuation for vibration and flutter suppression experiments is completed. A two degree of freedom typical section model with steady aerodynamics is used to gain an understanding of the fundamentals of the strain actuated aeroelastic control problem. Actuation issues and the effects of fiber and geometric sweep are examined using the typical section. Controllers are designed using the Linear Quadratic Regulator (LQR) method and observers are designed using the Kalman filter. The results are verified through a series of parameter variations and the incorporation of unsteady aerodynamics. With the typical section analyses as a foundation, the actual design is begun. The functional requirements and the design parameters are explicitly outlined. Non-parametric studies are used to determine several of the geometric design parameters. Specifically, a scaling analysis is used to determine the piezoelectric thickness and the spar thickness. Three parametric trade studies are used to determine the remainder of the design parameters. A five mode Rayleigh-Ritz analysis with two dimensional unsteady strip theory aerodynamics is used for all of the parametric trade studies. The first trade study examines the interaction of the fiber and the geometric sweep. The effect of fiber and geometric sweep on the stability characteristics, the piezoelectric actuation, and the relative authority of LQR controllers using piezoelectric actuation or conventional flap actuation is observed. The second trade study consists of the design of a tip mass flutter stopper. The final trade study investigates the influence of taper on the dynamics of the wing.

Thesis Supervisor: Dr. Edward F. Crawley

Title: Professor of Aeronautics and Astronautics
MacVicar Faculty Fellow

Acknowledgements

Although there is only one author's name on the title page of this thesis, there are many people who have contributed greatly to its completion.

First I would like to thank my advisor, Professor Ed Crawley, for the countless discussions and meetings that have peppered the last two and a half years and that have aided my intellectual growth (or at least we hope so). In addition, I would like to thank Professor John Dugundji who has served as an unofficial co-advisor for the past half year for all of the time he has been willing to spend.

I also have to thank the National Science Foundation for their generous fellowship during my years of being a Master's student.

Next I would like to say thanks to all of the people of SERC - past and present (although I guess there aren't too many in the past category). Thanks for the technical discussions and the social ones, too. I'd especially like to mention my officemates who have had to put up with my idiosyncrasies, even if they haven't always turned up the heat.

To my parents who have always taught me that education is very important and to my sister - for always trying to understand me.

To Alissa Fitzgerald - whom I will always admire for her strength.

To "the gang" - for friendship and fun times.

To Mark Campbell - thank you for listening to me and keeping your cool when I was losing mine. Without you around, grad school would have been much less enjoyable. Go Penguins!

And finally, to Terry. I hope you will always know how much I appreciate your unflagging support. Thank you for always being there to listen to me vent my frustrations, for helping me find my strength when it didn't seem like I had any left, and for providing a safe harbor. I can't say enough about your role in my thesis, my sanity, and my life.

Table of Contents

List of Figures

List of Tables

Introduction

Chapter 1

In recent decades, one of the focuses of aeroelastic research has been the control of aeroelastic behavior. The objectives have included delaying the onset of instability, ride control or vibration suppression, and maneuver and performance enhancement. Many passive aeroelastic design techniques involving tailoring composite laminates have been used and, more recently, active control techniques have been developed.

Shirk, Hertz, and Weisshaar provided a historical background of aeroelastic tailoring and a survey of work in the field and defined aeroelastic tailoring as "the embodiment of directional stiffness into an aircraft structural design to control aeroelastic deformation, static or dynamic, in such a fashion as to affect the aerodynamic and structural performance of that aircraft in a beneficial way." [1984] Preliminary work examined the effect of bend-twist coupling on the in-vacuo structural dynamics of a wing and developed accurate analysis methods [Jensen, et al. 1982 and Weisshaar and Foist, 1985]. Wind tunnel tests of cantilevered bend-twist coupled plates were completed to verify analytically predicted flutter and divergence speeds [Hollowell and Dugundji, 1984]. Geometric sweep was subsequently added

[Landsberger and Dugundji, 1985] and, for completion, rigid body modes were implemented [Chen and Dugundji, 1987].

Concurrent to the development of aeroelastic tailoring techniques, active aeroelastic control techniques were beginning to be implemented. One of the earliest flutter suppression experiments involved a clean cantilevered delta-wing with a leading edge flap actuator and a trailing edge flap actuator [Sandford, et al. 1975]. Because the addition of wing-stores can drastically lower the flutter speed, an international investigation using a half-span YF-17 model developed and tested wing-store flutter suppression systems [Hwang, et al. 1980 and Hwang, et al. 1981]. One of the most recent series of flutter suppression experiments used the Active Flexible Wing model [Perry, et al. 1990]. The AFW model was a full span model with a rigid fuselage and highly flexible bend-twist stiffness coupled wings. The AFW also had two leading edge control surfaces and two trailing edge control surfaces, thereby integrating passive aeroelastic tailoring techniques and active control techniques. All of the above wind tunnel experiments were conducted in the Transonic Dynamics Tunnel at the NASA Langley Research Center.

To date, conventional flap actuation has been used in the majority of active control designs for flutter and vibration suppression. The main reason for the dominance of flap actuation is the presence of high authority trailing edge control surfaces on existing wings. Because flaps and ailerons were not originally designed for these purposes, they are not necessarily the optimal actuators for aeroelastic control. In general, flaps operate over a limited bandwidth which may not include all important aeroelastic modes. Because the flap actuation mechanism is typically hydraulic and a flap must generate aerodynamic forces to deform the wing, the complete actuation mechanism includes significant hydraulic and aerodynamic lags.

As an alternative to conventional flap actuation, strain actuation is being examined for use in aeroelastic control. The primary advantage to strain actuation is that the actuators affect the structure directly by inducing strain in the structure. An additional benefit is the bandwidth of strain actuators which is large compared to the frequencies of structural dynamic deformation. Since strain is induced in the structure directly, there are no associated lags. Because of their relatively recent development, strain actuators are still in the research and early development stages. Piezoelectric actuators, one type of strain actuator, have been characterized and modelled for incorporation into beams and plates [Crawley and Anderson, 1990 and Crawley and Lazarus, 1991]. The use of piezoelectric actuators to modify the static aeroelastic behavior has been examined analytically [Ehlers and Weisshaar, 1990] and a two degree of freedom wind tunnel model has been used to demonstrate strain actuated flutter suppression [Heeg, 1992]. The most sophisticated experimental model to date is a plate-like lifting surface with piezoelectric actuators, which has successfully demonstrated vibration and flutter suppression using multiple input/multiple output controllers [Lazarus and Crawley, 1992].

In the introduction of a new technology, such as strain actuated aeroelastic control, there are three essential phases: development, demonstration, and verification. The first phase introduces the new technology and shows that the concept is valid. The second phase incorporates the new technology into a more realistic environment while still focusing on the fundamentals. The final phase brings the new technology to maturation and prepares it for use on a full-size working system.

The development phase of strain actuation for aeroelastic control applications has already been completed. Lazarus, using the strain actuated

plate-like lifting surface mentioned earlier, demonstrated the use of piezoelectric strain actuation in aeroelastic control [Lazarus and Crawley, 1992]. The aeroelastic models tested were flat plates with a 6 in. chord and a 12 in. span. The piezoelectric actuators were grouped into three spanwise actuation areas for all three plates: one group covered the leading edge, one the middle, and one the trailing edge. The sensors used were laser displacement sensors placed in the walls of the wind tunnel.

The piezoelectric actuators used in these experiments are thin sheet piezoelectrics which exhibit in-plane isotropy. Because of the in-plane isotropy, these piezoelectrics can only induce bending or extensional strain and not shear strain. Since the torsional mode is important in aeroelasticity and is dominated by shear strain, a means for piezoelectric control over the torsional mode must be developed. To enhance torsional authority, Lazarus used both a graphite epoxy plate with bend-twist coupling and, as a reference, an isotropic aluminum plate.

Using the strain actuators, Lazarus demonstrated significant vibration suppression and flutter suppression. The vibration suppression experiments showed good reduction of the first bending mode, but the piezoelectrics did not demonstrate significant control of the torsional mode. Contrary to expectations, the bend-twist coupled graphite-epoxy plate did not enable more torsional control than the aluminum plate. This was likely due to piezoelectric groupings chosen inappropriately for independent control of the torsional mode. Lazarus also conducted flutter suppression experiments on a modified aluminum test article and was able to increase the flutter speed by 11%.

The objective of this study is to further demonstrate strain actuated aeroelastic control technology and compare the performance of the strain

actuators to that of the existing technology of conventional flap actuators. This study begins the demonstration phase of the use of strain actuation for aeroelastic control and constitutes the preliminary design phase of a research project conducted by M.I.T. in cooperation with the NASA Langley Research Center (LaRC). Following this preliminary design, a detailed hardware design will be conducted. Once the detailed design of the wing model is completed, the wing model will be built and tested in the Transonic Dynamics Tunnel at LaRC. The complete study and experiment will be the demonstration phase of the strain actuation technology for aeroelastic control. In this document, several issues in the design of the demonstration phase model will be studied to better understand the use of strain actuation.

The first section of this study examines the fundamentals of the strain actuation problem and will be used as the foundation for the remainder of the design. In Chapter 2, a typical section will be used as a low order model to isolate the underlying physical mechanisms. The actuators to be implemented on the typical section include a strain actuated force, a strain actuated moment, a leading edge flap, and a trailing edge flap. The dynamics of the typical section using steady aerodynamics and the interaction between plant, sensors, and actuators will be examined to understand the control challenges. Then, controllers will be designed using the strain actuators and flaps alone and in various combinations. The intent is to gain insight into the aeroelastic control problem for later use in the design. Having designed controllers and elucidated any guiding principles, the effects of introducing bend-twist coupling, or fiber sweep, and structural sweep will be examined. In this simple model, only their effect on stability characteristics will be studied. Finally, some parameter variations will be completed and unsteady

aerodynamics will be incorporated to examine the robustness of the qualitative results.

Having established the foundation, a preliminary design of the demonstration phase model will be conducted. The first step, discussed in Chapter 3, is to establish the functional requirements and the design parameters. The functional requirements determine the design's objectives [Suh, 1990]. The design parameters are those physical parameters which may be altered to meet the functional requirements [Suh, 1990]. The design parameters will be set through a series of non-parametric and parametric studies.

Chapter 4 summarizes the non-parametric studies which include a survey and a scaling analysis. A survey of current commercial aircraft will define the majority of geometric design parameters. A scaling analysis will compare the piezoelectric authority of the earlier development phase experiments to the piezoelectric authority expected in the current design. This scaling analysis will establish the nominal structural thickness and piezoelectric thickness.

The primary parametric study will be presented in Chapter 5 and examines the effects of fiber sweep and structural sweep on the aeroelastic behavior and on the use of piezoelectric actuators. Using a five mode Rayleigh-Ritz analysis and two-dimensional strip theory aerodynamics, the stability characteristics of the wing model for varying fiber and geometric sweep will be determined. The trade space will be narrowed to satisfy the functional requirements and further studies will focus on a region which is robust to minor changes in fiber and geometric sweep.

To evaluate the smaller trade space and choose design fiber and geometric sweeps, the effect on piezoelectric actuation authority will be

examined. Basic piezoelectric groups will be defined by strain contours to provide effective, independent control of the important modes. Controllers will be developed to compare the authority of the piezoelectric actuators and a trailing edge flap and ensure that they are fairly matched.

As a second parametric trade study, a tip mass flutter stopper will be designed in Chapter 6. The main purpose of the flutter stopper is to enable the wing model to be brought safely to a stable aeroelastic condition after the onset of flutter. The operating principle behind the design is to change the wing model properties in such a way that the deployment of the flutter stopper raises the flutter speed significantly. The hinge position, mass, and length of the flutter stopper will be varied to understand their effect on the flutter speed.

The final parametric trade study in Chapter 7 involves the taper ratio. Various taper ratios will be included in the wing model to examine their effect on the aeroelastic behavior and actuation of the wing model. Based on these studies and the survey completed earlier, a design taper ratio will be chosen.

The preliminary design and the scientific issues discussed during the design process will then be summarized. This document is the preliminary design documentation and the summary will include the baseline values for all of the design parameters. Detailed design, construction, and testing will follow during which these values may be incrementally altered.

Foundation for Design

Chapter 2: Typical Section Analyses

2.1 Introduction

Before beginning the process of design, it is important to understand the fundamental mechanisms of the problem. Engineers use simplified, low order models to gain an understanding of the essential physics of the problem. Aeroelasticians use the typical section. The typical section is a two-dimensional chordwise segment of a wing whose properties and parameters are thought to be representative of the wing as a whole. Normally, typical sections are taken at the 3/4 span point of a wing and include only two degrees of freedom: pitch and plunge.

In this design process, there are two important trends that need to be understood: the effect of strain actuation and of geometric and fiber sweep. This typical section analysis will be used to study these issues. First, the equations of motion for a typical section using steady aerodynamics will be derived and non-dimensionalized. Then a reference typical section will be developed and its dynamics with changing airspeed will be studied. Following this characterization, full-state feedback controllers will be developed using the Linear Quadratic Regulator (LQR) method with varying combinations of actuators. Next, output feedback controllers will be developed using the Linear Quadratic Gaussian (LQG) method. Once these actuation issues have been studied, the effect of geometric and fiber sweep on

the typical section dynamics will be examined. Finally, the robustness of the actuation and sweep results will be verified with parameter variations and the incorporation of full unsteady aerodynamics.

2.2 Description of model

In this section, the typical section will be introduced and its parametric equations of motion will be derived. The geometry of the typical section used in this analysis can be seen in Figure 2.1. This section closely resembles the section described by Bisplinghoff, Ashley, and Halfman [1955] with the addition of a leading edge flap. The two degrees of freedom of this section are pitch (α) and plunge (h). The distance of the elastic axis aft of the midchord is repesented by ab, where b is the semichord, and the distance of the center of gravity aft of the elastic axis is $x_\alpha b$. The actuators on this section are strain actuators and conventional flaps. Steady aerodynamics will be used and no aerodynamic or structural damping will be modelled. A time variation in the angle of attack, α_o, is the disturbance to the section.

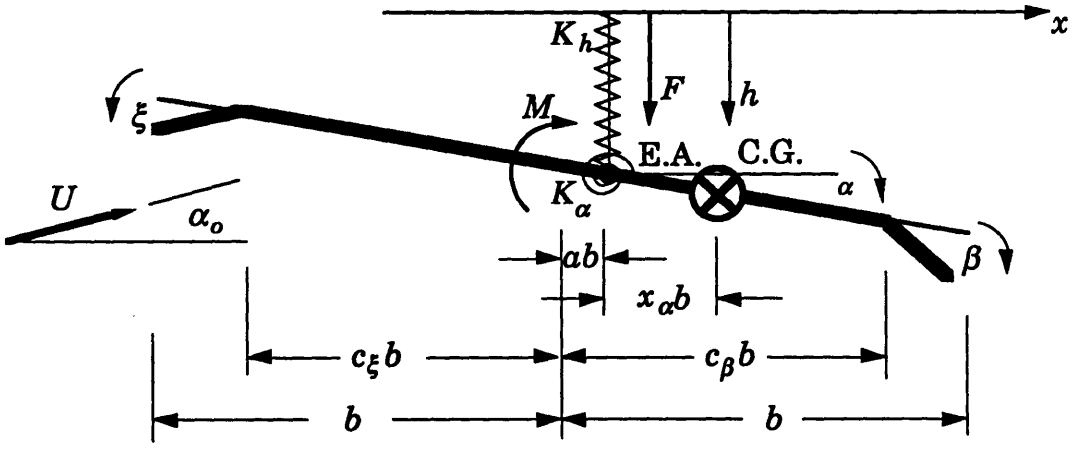

Figure 2.1 Typical section geometry

To represent the wing as a typical section, several modelling assumptions have been made. To approximate the stiffness of the rest of the

wing as it affects the typical section, two springs are placed at the elastic axis. Using uncoupled stiffnesses, a bending spring (K_h) models the wing bending stiffness and a torsional spring (K_α) models the wing torsional stiffness. Similarly, the strain actuation effect is modelled as a force (F) and a moment (M) at the elastic axis. The strain actuation force is approximated by equating the deflection at the typical section due to distributed strain actuators and the deflection due to a concentrated force acting at the section. Since the strain actuation mechanism for creating moment is not as clearly defined, the moment is estimated with half of the effect of the force [Lazarus and Crawley, 1992a]. The leading edge flap (ξ) and trailing edge flap (β) are modelled with no dynamics, thus allowing flap angles to be commanded directly.

The aerodynamic forces and moments generated by flap deflections must be calculated. While there exists much information on calculating the aerodynamic coefficients of trailing edge flap configurations, leading edge flap aerodynamics are not as well documented. The method chosen to obtain the aerodynamic coefficients is to transform the wing-aileron-tab combination, analyzed by Theodorsen and Garrick [1942], into a leading edge flap-wing-trailing edge flap combination (Figure 2.2). The transformation involves

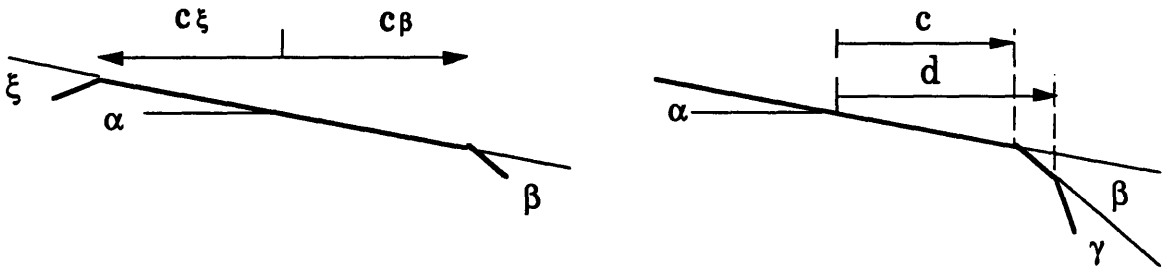

Figure 2.2 Transformation from Leading edge-Wing-Trailing Edge to Wing-Aileron-Tab for use in aerodynamic equations

simple angle and length conversions (Equations 2.1). These aerodynamic calculations were verified using thin airfoil theory [Kuethe and Chow, 1986].

$$\begin{aligned} \alpha_{eff} &= \alpha - \xi & c &= -c_\xi \\ \beta_{eff} &= \xi & d &= c_\beta \\ \gamma_{eff} &= \beta \end{aligned} \tag{2.1}$$

The equations of motion for this typical section can now be derived.

$$\begin{aligned} m\ddot{h} + x_\alpha bm\ddot{\alpha} + K_h h &= F - \rho U^2 bC_{L_\beta}\beta - \rho U^2 bC_{L_\xi}\xi - \rho U^2 bC_{L_\alpha}(\alpha + \alpha_o) \\ m\ddot{h}x_\alpha b + \left(I + x_\alpha^2 b^2 m\right)\ddot{\alpha} + K_\alpha \alpha &= M + \rho U^2 b^2 C_{M_\beta}\beta + \rho U^2 b^2 C_{M_\xi}\xi + \rho U^2 b^2 C_{M_\alpha}(\alpha + \alpha_o) \end{aligned} \tag{2.2}$$

These equations of motion describe the motion of the elastic axis and all moments have been evaluated about this point. Using the elastic axis as the reference point, the structural stiffness uncouples. However, the equations are coupled by the static imbalance in the mass matrix and also by the aerodynamic terms.

These equations are then non-dimensionalized using the semi-chord (b) as the characteristic length, the torsional frequency (ω_α) as the characteristic time, and the typical section mass (m) as the characteristic mass. A complete set of non-dimensional parameters is obtained.

Non-dimensionalized plunge	$\overline{h} = \dfrac{h}{b}$
Radius of gyration	$R_\alpha^2 = \dfrac{I_\alpha}{mb^2}$
Mass ratio	$\mu = \dfrac{m}{\pi \rho b^2}$
Frequency ratio	$\overline{\omega}_h = \dfrac{\omega_h}{\omega_\alpha}$
Non-dimensional airspeed	$U_\alpha = \dfrac{U}{\omega_\alpha b}$

Non-dimensional Laplace variable $p = \dfrac{\lambda}{\omega_\alpha}$

Strain actuation plunge control $u_h = \dfrac{Fb}{K_\alpha}$

Strain actuation pitch control $u_\alpha = \dfrac{M}{K_\alpha}$

Trailing edge flap control $u_\beta = \beta$

Leading edge flap control $u_\xi = \xi$

(2.3)

These parameters may then be used to non-dimensionalize the equations of motion.

$$\begin{bmatrix} 1 & \frac{x_\alpha}{R_\alpha^2} \\ \frac{x_\alpha}{R_\alpha^2} & 1 \end{bmatrix} \begin{Bmatrix} \bar{h}p^2 \\ \alpha p^2 \end{Bmatrix} + \begin{bmatrix} \frac{\bar{\omega}_h^2}{R_\alpha^2} & \bar{q}C_{L_\alpha} \\ 0 & 1-\bar{q}C_{M_\alpha} \end{bmatrix} \begin{Bmatrix} \bar{h} \\ \alpha \end{Bmatrix} =$$

$$\begin{bmatrix} 1 & 0 & -\bar{q}C_{L_\beta} & -\bar{q}C_{L_\xi} \\ 0 & 1 & \bar{q}C_{M_\beta} & \bar{q}C_{M_\xi} \end{bmatrix} \begin{Bmatrix} u_h \\ u_\alpha \\ u_\beta \\ u_\xi \end{Bmatrix} + \begin{bmatrix} -\bar{q}C_{L_\alpha} \\ \bar{q}C_{M_\alpha} \end{bmatrix} \alpha_o \qquad (2.4)$$

$$\text{where } \bar{q} = \frac{U_\alpha^2}{\mu \pi R_\alpha^2}$$

Having established the equations of motion and derived the appropriate aerodynamic forces, the equations will now be placed into state-space form. State-space is the simplest form for control design. The non-dimensional equations of motion (Equations 2.4) are of the following nature:

$$\mathbf{M}\begin{Bmatrix} \bar{h}p^2 \\ \alpha p^2 \end{Bmatrix} + \mathbf{K}\begin{Bmatrix} \bar{h} \\ \alpha \end{Bmatrix} = \mathbf{f}\begin{Bmatrix} u_h \\ u_\alpha \\ u_\beta \\ u_\xi \end{Bmatrix} + \mathbf{d}\alpha_o \qquad (2.5)$$

The transformation from these physical equations to state-space form is straightforward.

$$\dot{x} = \mathbf{A}x + \mathbf{B}u + \mathbf{L}\alpha_o$$
$$y = \mathbf{C}x \tag{2.6}$$

where

$$\mathbf{A} = \begin{bmatrix} \mathbf{0}_{(2x2)} & \mathbf{I}_{(2x2)} \\ -\mathbf{M}^{-1}\mathbf{K} & \mathbf{0}_{(2x2)} \end{bmatrix} \quad \mathbf{B} = \begin{bmatrix} \mathbf{0}_{(2x4)} \\ \mathbf{M}^{-1}\mathbf{f} \end{bmatrix} = [\mathbf{b}_h \quad \mathbf{b}_a \quad \mathbf{b}_b \quad \mathbf{b}_x]$$

$$\mathbf{L} = \begin{bmatrix} \mathbf{0}_{(2x4)} \\ \mathbf{M}^{-1}\mathbf{d} \end{bmatrix} \quad \mathbf{x} = \begin{Bmatrix} \bar{h} \\ \alpha \\ \dot{\bar{h}} \\ \dot{\alpha} \end{Bmatrix} \quad \mathbf{u} = \begin{Bmatrix} u_h \\ u_\alpha \\ u_\beta \\ u_\xi \end{Bmatrix}$$

here $\bullet$ refers to $\frac{\mathrm{d}}{\mathrm{d}\tau}$ where $\tau = t\omega_\alpha$

Clearly this transformation does not change the dynamics of the system; in fact, the equations of motion are reproduced exactly as two of the equations in this set. The remaining two equations are "dummy" equations used to complete the format.

2.3 Control analysis for the reference case

Now that the equations of motion have been placed in state-space form, the typical section will be analyzed from a control viewpoint. Before controllers are designed, a reference typical section will be established. Then the open loop behavior of the reference section will be characterized for varying speeds. Based on this analysis, two design speeds will be chosen and full state feedback controllers will be designed using the Linear Quadratic Regulator method. Finally, output feedback controllers will be designed using the Linear Quadratic Gaussian method to understand the effects of noise and partial state measurements.

The reference typical section is chosen to be representative of high performance, low aspect ratio wings, such as the development phase test

article. The wing mass is assumed to be evenly distributed so that the center of gravity lies at the midchord. In contrast, the elastic axis location is forward of the midchord by 20 % of the semichord, which is representative of a 4.5 degree forward fiber sweep. The flaps are both 10% of the chord. The remaining parameters are chosen as representative values (Appendix A).

Characterization of open loop plant

Before beginning the design of controllers, the open loop plant must be understood. The location and pattern of poles and zeros for the system are vitally important for control purposes. To find the poles and zeros, the appropriate transfer function, or input-output relation, must be found.

Using the state-space form, the output matrix C (Equation 2.6) may be chosen to select or combine any of the states in any ratio as outputs. The relation from the actuators to the measurements, or the transfer function, once the output matrix has been chosen is described as

$$\mathbf{y} = \mathbf{C}\Phi\mathbf{B}\mathbf{u} \qquad \text{where} \qquad \Phi = (\mathbf{p}\mathbf{I} - \mathbf{A})^{-1} \tag{2.7}$$

The poles of the system are the roots of the denominator of the transfer function. The location of these poles in the complex plane defines the stability and damping of the plant. The zeros, or roots of the numerator, define the interaction of the actuators and measurements with the plant dynamics.

By analyzing the poles as they migrate with change in airspeed, important properties of the open loop plant may be determined. The poles of the system may be found by taking the determinant of Φ (Equation 2.7). The determinant can be expressed in the form of the characteristic equation of the system.

$$\Delta(p)=\left[1-\frac{x_\alpha^2}{R_\alpha^2}\right]p^4+\left[\left(\overline{\omega}_h^2+1\right)-\overline{q}\left(C_{L_\alpha}x_\alpha+C_{M_\alpha}\right)\right]p^2+\left[\overline{\omega}_h^2\left(1-\overline{q}C_{M_\alpha}\right)\right] \tag{2.8}$$

The poles, or roots of the characteristic equation, are dependent on the section geometry, structural properties, and air speed. As Figure 2.3 shows, the poles begin on the imaginary axis and eventually coalesce with increasing airspeed. This point of coalescence is known as the flutter point and occurs for the reference section at U_α = 1.90. After the flutter point, the poles separate and become mirror images of each other, one in the left half plane, or stable, and one in the right half plane, or unstable. During this period, reversal of the trailing edge flap occurs at U_α = 2.40. Increasing the air speed past flutter drives the poles down to the real axis. The divergence point occurs for the reference section at U_α = 2.88.

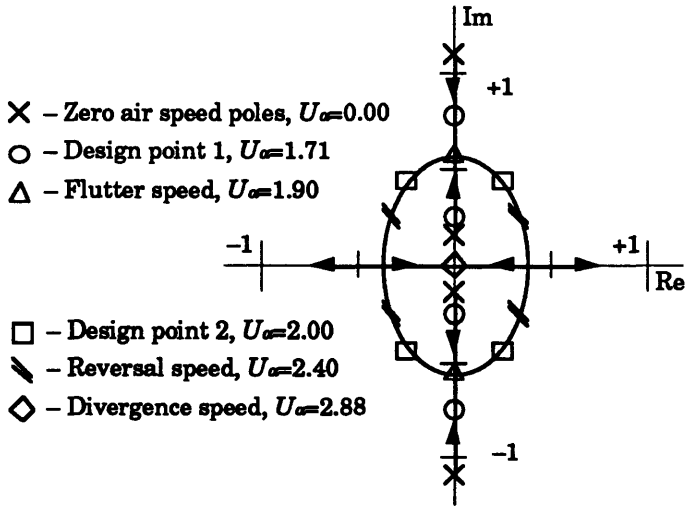

Figure 2.3 Pole movement for nominal typical section as airspeed changes

Because the poles travel a great deal with change in airspeed, representative airspeeds must be chosen as design points for control. Based on the pole movement, two design points are chosen as part of the reference case. Design point 1 at U_α = 1.71 was chosen to be 10% below flutter while the system is still marginally stable. Design point 2 at U_α = 2.00 was chosen

to be 5% above flutter when the system is unstable. Both design points are well before reversal and divergence so that the flutter phenomenon may be isolated and studied.

Having examined the poles of the plant, the zeros will now be studied. The zeros reflect the interaction of the actuators and measurements with the plant dynamics. The displacement states will be chosen as the measurements, or outputs, as the desired goal is to minimize the magnitude of the displacements. Choosing these outputs, the transfer function from each of the actuators to each of the measurements can be derived.

$$\begin{Bmatrix} \bar{h} \\ \alpha \end{Bmatrix} = \frac{R_\alpha^2}{\Delta(p)} \begin{bmatrix} n(p)_{hh} & n(p)_{h\alpha} & n(p)_{h\beta} & n(p)_{h\xi} \\ n(p)_{\alpha h} & n(p)_{\alpha\alpha} & n(p)_{\alpha\beta} & n(p)_{\alpha\xi} \end{bmatrix} \begin{Bmatrix} u_h \\ u_\alpha \\ u_\beta \\ u_\xi \end{Bmatrix} \tag{2.9}$$

where

$$n(p)_{hh} = p^2 + 1 - \bar{q} C_{M_\alpha}$$

$$n(p)_{\alpha h} = -\frac{x_\alpha p^2}{R_\alpha^2}$$

$$n(p)_{h\alpha} = -\frac{x_\alpha p^2}{R_\alpha^2} - \bar{q} C_{L_\alpha}$$

$$n(p)_{\alpha\alpha} = \frac{p^2}{R_\alpha^2} + \frac{\bar{\omega}_h^2}{R_\alpha^2}$$

$$n(p)_{h\beta} = \bar{q} C_{L_\beta} \left(\bar{q} C_{M_\alpha} \left(1 - \frac{C_{L_\alpha} C_{M_\beta}}{C_{M_\alpha} C_{L_\beta}} \right) - 1 - p^2 \left(1 + \frac{C_{M_\beta} x_\alpha}{C_{L_\beta} R_\alpha^2} \right) \right)$$

$$n(p)_{\alpha\beta} = \frac{1}{R_\alpha^2} \bar{q} C_{M_\beta} \left(p^2 \left(1 + \frac{C_{L_\beta} x_\alpha}{C_{M_\beta}} \right) + \bar{\omega}_h^2 \right)$$

$$n(p)_{h\xi} = \bar{q} C_{L_\xi} \left(\bar{q} C_{M_\alpha} \left(1 - \frac{C_{L_\alpha} C_{M_\xi}}{C_{M_\alpha} C_{L_\xi}} \right) - 1 - p^2 \left(1 + \frac{C_{M_\xi} x_\alpha}{C_{L_\xi} R_\alpha^2} \right) \right)$$

$$n(p)_{\alpha\xi} = \frac{1}{R_\alpha^2} \bar{q} C_{M_\xi} \left(p^2 \left(1 + \frac{C_{L_\xi} x_\alpha}{C_{M_\xi}} \right) + \bar{\omega}_h^2 \right)$$

Note that the denominator of each of the transfer functions is the characteristic equation.

By setting the transfer function numerators to zero, the zeros of each single input-single output system can be found and their behavior with change in airspeed studied. Figure 2.4 shows the movement of the zeros in relation to the poles with change in airspeed. The pole/zero pattern changes for different airspeeds which makes control over a range of airspeeds complicated. The intersection of all four plunge output zeros and the torsional pole at the same point indicates that the torsional mode can not be detected through plunge measurements at that particular airspeed; it is unobservable. The two design points chosen lie beyond the quintuple crossing point and all of the zeros are higher in frequency than both poles. Normally a pattern of pole-zero-pole is desirable for control and it can be seen that neither design point possesses that pattern [Lazarus and Crawley, 1992a]. Figure 2.4 also shows the zeros which do not lie strictly on the real axis for the pitch output transfer functions. None of these zeros move with airspeed although the pole/zero patterns do change with airspeed which would make robust control complicated.

Figures 2.5 and 2.6 allow a closer look at the individual pole/zero patterns for the two design points selected. As discussed earlier, none of the patterns have the desirable pole-zero-pole pattern. Additionally, several of the transfer functions show near pole-zero cancellations which would indicate that a mode may be nearly uncontrollable from a given actuator. This indicates that the actuators may be able to be grouped into those which primarily exert influence over the pitch mode and those which primarily exert influence over the plunge mode. This will become clearer when the controllers are designed. As a final point, the trailing edge flap has a zero in

the right half-plane, or non-minimum phase zero, at the first design point and both of the flaps show non-minimum phase zeros at the second design point. Non-minimum phase zeros add phase lag rather than decreasing phase lag, as a minimum phase, left half-plane, zero would. This tends to make systems controllable only for frequencies below that of the zero. Thus, non-minimum phase zeros impose a limit on performance and, therefore, may indicate a drawback to using flaps for flutter and vibration control.

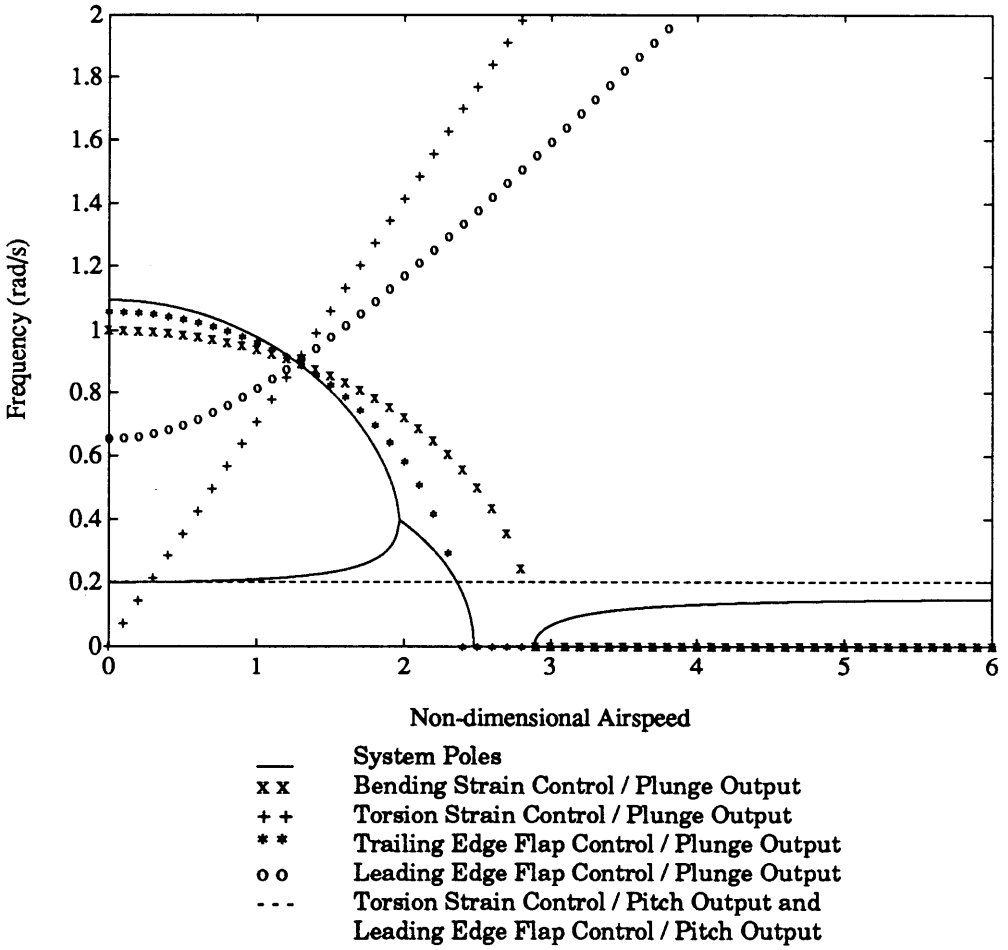

Figure 2.4 Pole and individual SISO transfer function zero frequencies versus non-dimensionalized airspeed U_α. Nominal parameters.

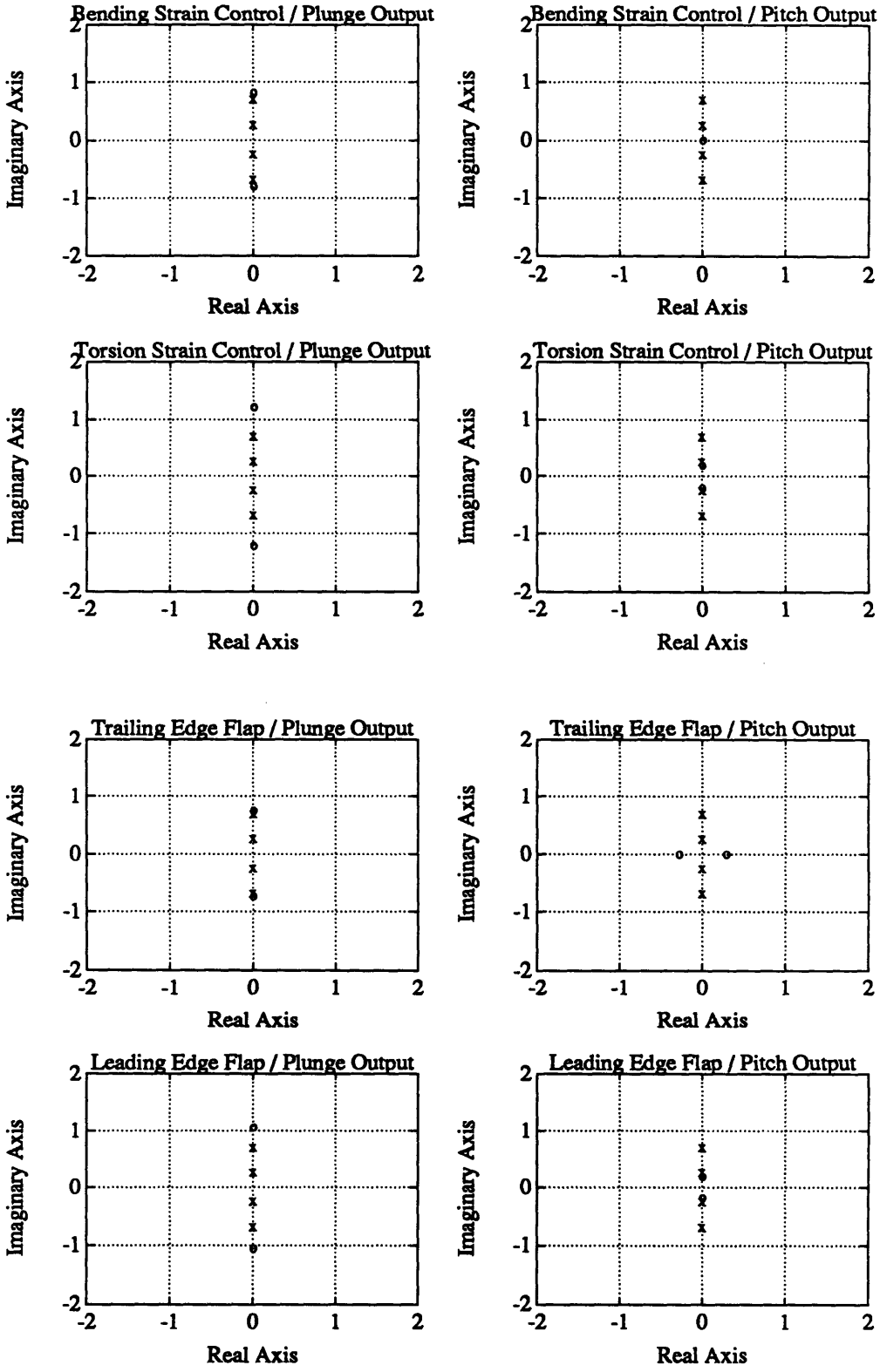

Figure 2.5 Pole and zero locations for the individual SISO transfer functions at design point 1 (U_α = 1.71)

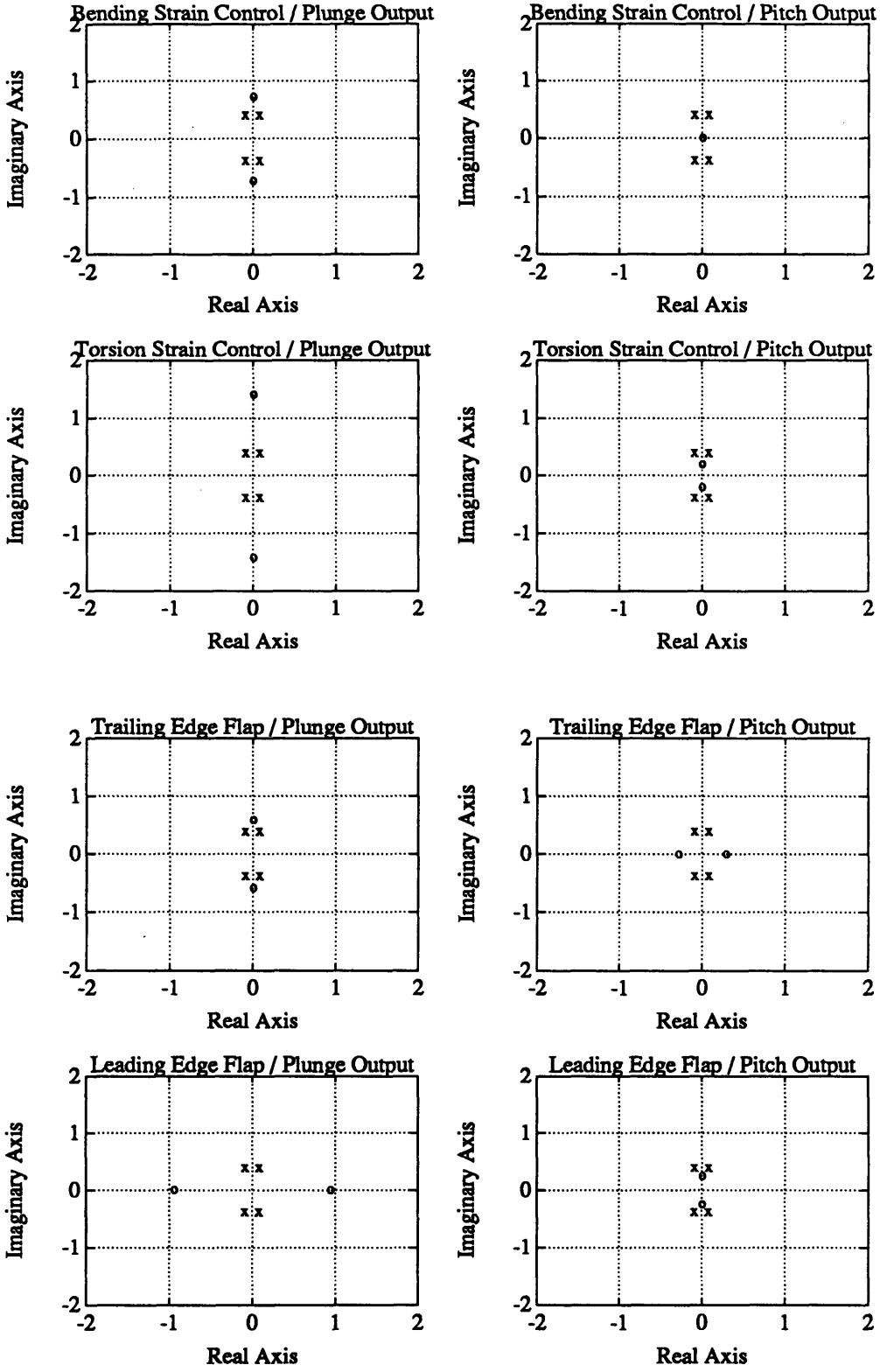

Figure 2.6 Pole and zero locations for the individual SISO transfer functions at Design Point 2 (U_α = 2.00)

Full State Feedback: Linear Quadratic Regulator

In this section, full state feedback controllers are designed. Full state feedback allows a controller to utilize displacement and rate information and to use combinations of these that do not appear on the physical airfoil. However, full state feedback is an idealization, as, most often, all states can not be measured for feedback. Following an explanation of the Linear Quadratic Regulator (LQR) method, controllers will be developed for design point 1. Then the different actuators will be compared. Finally, the results will be verified by evaluating controllers at design point 2.

The optimal gains for full state feedback can be found by solving the Linear Quadratic Regulator problem [Kwakernaak and Sivan, 1972]. The solution to this problem provides for a stable plant with relatively high damping. Solving the LQR problem entails minimizing the following scalar cost functional.

$$J = \int_0^\infty \left(x^T Q x + \rho u^T R u \right) dt \tag{2.10}$$

Minimizing this cost functional minimizes the states and controls used according to given weightings. Q, the state weighting matrix, is often chosen as the quadratic of some performance vector, with $Q = N^T N$ and $z = Nx$, where z is the performance vector. The performance vector defines which states the designer feels are important. R, the control weighting matrix, is often chosen to normalize the controls by their predetermined maximum values. ρ, the control weighting, weights the importance of keeping the controls low to the importance of minimizing the state variables, or maximizing performance. Letting ρ approach zero allows the system to use large amounts of control; this is known as the "cheap" control case. On the other hand, letting ρ approach infinity prohibits the system from using more

control than is necessary to stabilize the plant; this is known as the "expensive" control case.

For the problem at hand, the weightings are chosen to give the costs physical significance. The state weighting matrix is based on a performance metric which only weights the plunge and pitch displacements, not the rates. In addition, each of these states is normalized according to a maximum displacement for the state. The maximum pitch displacement is calculated by assuming one percent strain in the structure and calculating the resulting angle at the 3/4 span point; the maximum plunge displacement is calculated by assuming one half percent strain and calculating the resulting vertical displacement at the 3/4 span point.

Similarly, the control weighting matrix normalizes the controls by their assumed maximums. The strain actuators are assumed to have a maximum actuation strain of $300\mu\varepsilon$, the trailing edge flap to have a maximum flap deflection of 5 deg, and the leading edge flap to have a maximum flap deflection of 2.5 deg. The maximum actuation strain and the maximum trailing edge flap deflection are chosen to be typical values for these actuators. The leading edge flap deflection is chosen by calculating the hinge moment caused by a 5 deg trailing edge flap deflection and finding the leading edge flap angle which would cause an equivalent hinge moment (steady aerodynamics assumed).

For the LQR results, two main tools are used for the comparison of actuators. First, the locus of the closed loop poles are plotted, parameterized by the control weighting ρ. Each actuator's or actuator combination's effectiveness in manipulating the two modes may be determined from these loci. Second, a cost analysis of the different actuators is performed. The state cost and control cost of each actuator are calculated and their relationship is

plotted. The costs are functions of the state covariance due to the inflow angle disturbance. The disturbance is represented as a one degree broadband white noise. The state cost is the weighted covariance of the states and the control cost is the weighted covariance of the commanded controls. The weighting matrices are the same as those used in the LQ cost functional.

One of the most important results from the LQ analysis is the fundamental performance limitation of designs employing only a single actuator. Such restrictions become most apparent in the limiting case of "cheap" control. Lazarus showed that as the control weight ρ goes to zero, the closed loop poles go to the stable finite zeros of the full Hamiltonian system (Equation 2.11), if they exist, or to infinity along stable Butterworth patterns [Lazarus and Crawley, 1992a].

$$\mathbf{H}(p) = \left[\mathbf{N}\Phi(-p)\mathbf{B}\right]^T \left[\mathbf{N}\Phi(p)\mathbf{B}\right] \tag{2.11}$$

One of the poles will travel to the zero and, therefore, a very limited amount of damping will be introduced into the mode. This sets a finite limit on performance. Figure 2.7 shows the closed loop pole loci for the single actuator cases for a control weighting range of $\rho = 10^4$ to $\rho = 10^{-4.5}$. In each of the single actuator cases, only one of the poles may be effectively moved to infinity along a stable Butterworth pattern.

Since each single actuator is only capable of truly controlling one mode well, types of actuators may be defined: those which effectively control the plunge mode, "plunge" actuators, and those which effectively control the pitch mode, "pitch" actuators. Reviewing the single actuator pole loci, it becomes obvious that both the bending strain actuator and the trailing edge flap primarily control the plunge mode, as they are only able to move the plunge mode effectively. Thus, both the bending strain actuator and the trailing

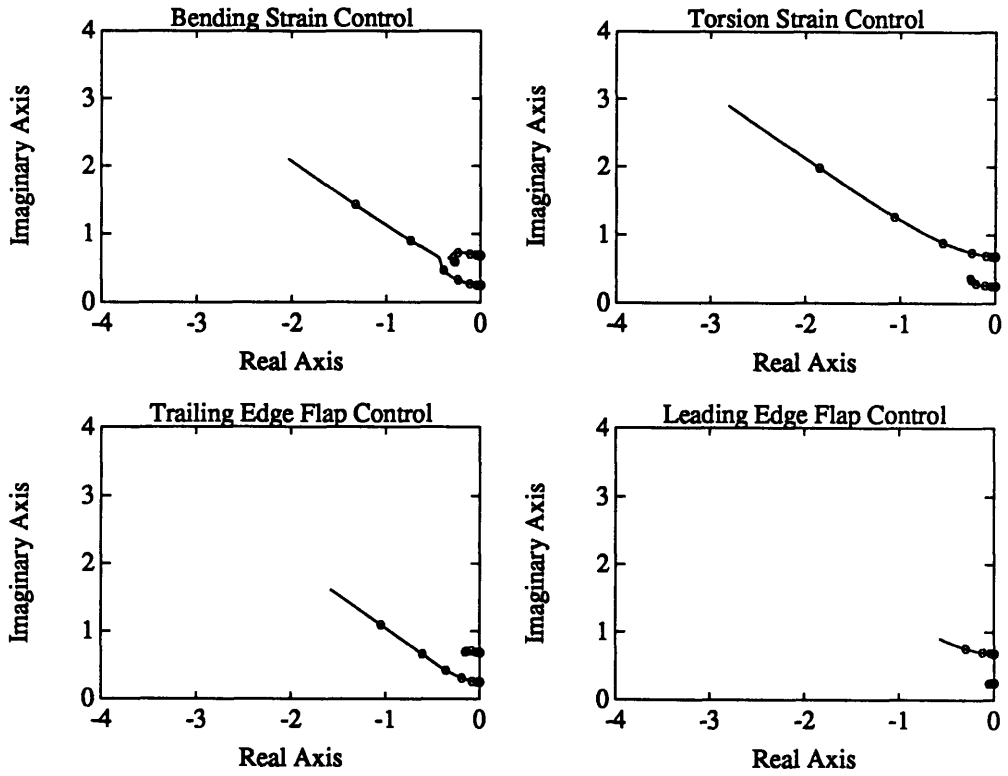

Figure 2.7 Loci of the LQR closed loop poles ($\rho = 10^4$ to $10^{-4.5}$) for the four actuators acting individually.

edge flap are "plunge" actuators. In a similar fashion, both the torsion strain actuator and the leading edge flap primarily control the pitch mode, or are "pitch" actuators.

These results can also be observed in the single actuator cost analyses (Figure 2.8). Each of the four single actuator curves approaches a horizontal asymptote as more control is applied; this implies that increasing the control does not lessen the state cost or improve the performance of the system. It is at this point that each actuator reaches its fundamental performance limit. The actuator has not saturated; it has driven one of the modes to the finite zero of the full Hamiltonian system and can not exert any further influence on the mode.

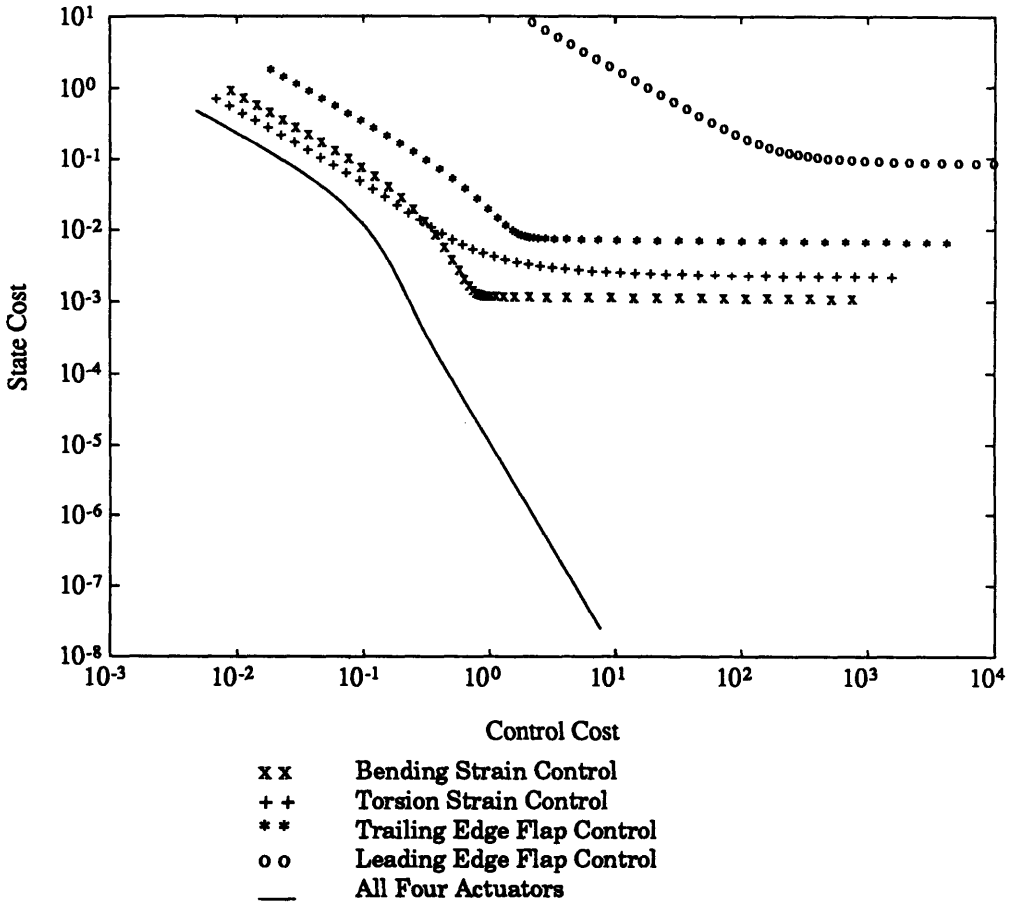

Figure 2.8 Cost curves for single actuator systems at design point 1 ($U_\alpha = 1.71$). System with all four actuators shown for comparison. ($\rho = 10^2$ to 10^{-8})

Since a lower state cost for a given control cost indicates superior performance, the relative performance of the different actuators can be seen. The bending strain actuator is a more effective actuator than the trailing edge flap, as the bending strain actuator's state cost is consistently lower than that of the trailing edge flap. The leading edge flap demonstrates its relative ineffectiveness as it evidences a significantly higher state cost than all of the other actuators for any given control cost.

The use of actuators in combination eliminates the performance limit that the single actuator controller designs experienced. All of the designs

which employ more than one actuator are capable of moving both of the poles along stable Butterworth patterns to infinity. Examples of the pole loci for combination designs are shown in Figure 2.9. This same result may be observed in the cost analysis (Figure 2.10). For all of the combinations, as the control effort is increased, the state cost continuously decreases. Notably, the combination of all four actuators does not perform significantly better than the best of the two actuator combinations. This result implies that an optimal number of well chosen actuators for this typical section with two modes is two actuators, or that it is important to have the same number of effective actuators as important modes, and not significant to use more.

While all of the pairs of actuators eliminate the performance limitation, certain pairs perform significantly better than other pairs. All of the pairs which include the leading edge flap perform rather poorly, as the leading edge flap in this example has proven to be a relatively ineffective actuator. As the other three actuators are nearly equal in effectiveness, the performance of their various combinations illuminate a basic guideline. An effective pair includes a "plunge" actuator and a "pitch" actuator, such that each important mode has an actuator which is capable of exerting considerable authority on it. This explains why the torsion strain actuator/trailing edge flap combination performs better than the bending strain actuator/trailing edge flap combination in all control regimes, even though the bending strain actuator is a slightly more effective single actuator than the torsion strain actuator in the "cheap" control regime. Likewise, it explains why the most effective "plunge" actuator and the most effective "pitch" actuator, the two strain actuators, when combined form the most effective pair which is essentially equivalent in performance to all four actuators together.

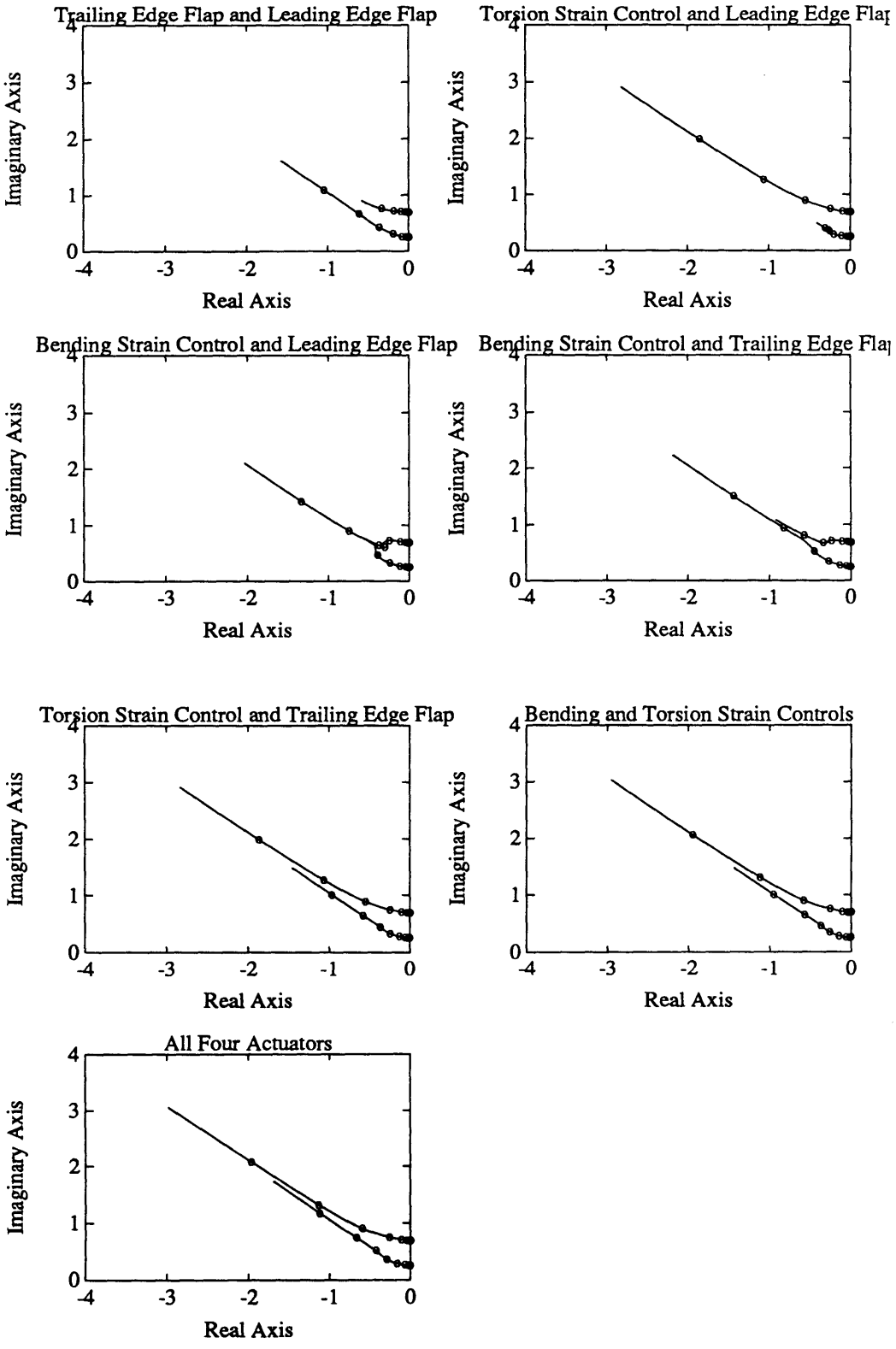

Figure 2.9 Loci of LQR closed loop poles for systems using multiple actuators ($\rho = 10^{4}$ to $10^{-4.5}$)

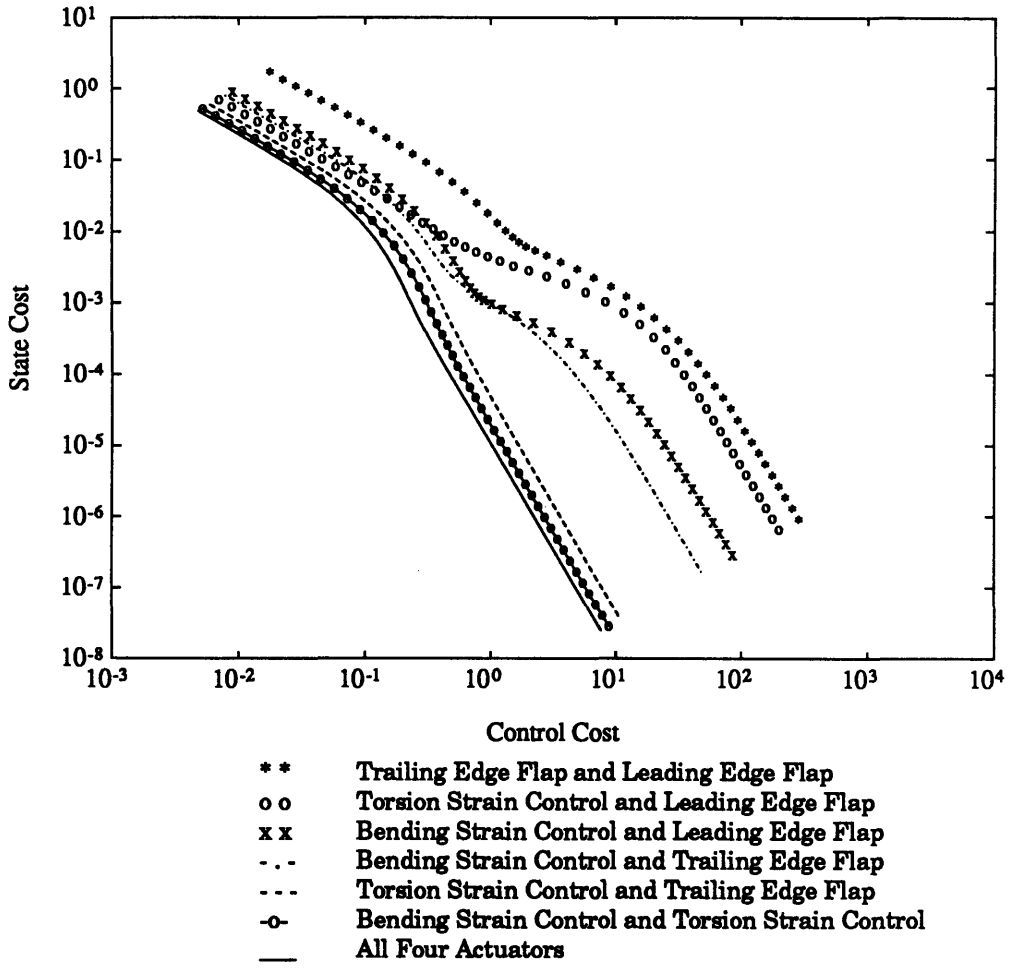

Figure 2.10 Cost curves for systems with multiple actuators. ($\rho = 10^{2}$ to 10^{-8})

To verify that these results are applicable to other airspeeds in addition to design point 1, design point 2 is analyzed in the same manner. The main difference between the two design points is the presence of an instability at design point 2. Since the leading edge flap has already been determined an ineffective actuator, it has been excluded from further consideration. All of the conclusions of the analysis of design point 1 are reiterated here: the limit on the performance of single actuators, the elimination of this limit in combinations of actuators, and the importance of including a "plunge" actuator and a "pitch" actuator (Figures 2.11 and 2.12).

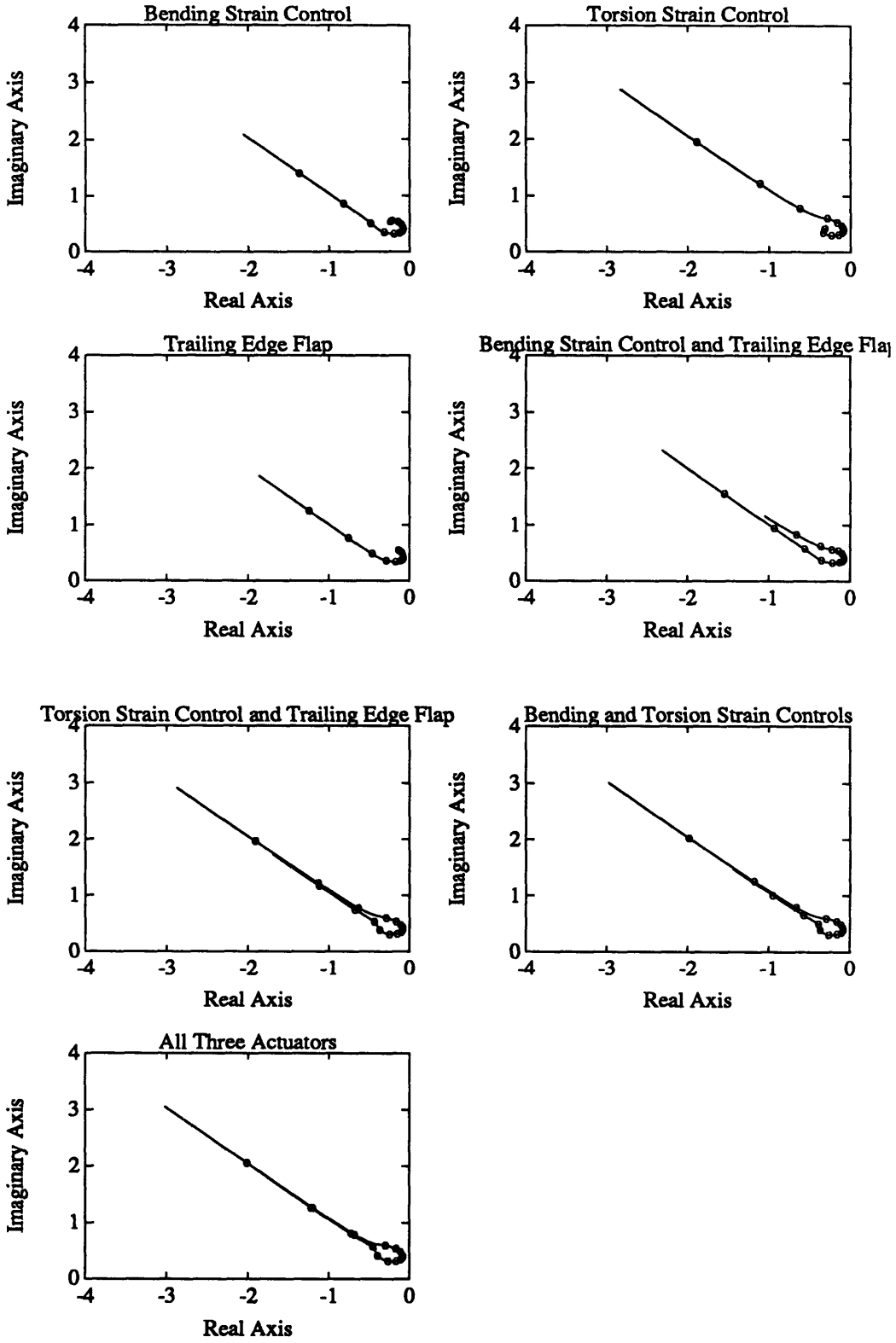

Figure 2.11 Loci of LQR closed loop poles for design point 2 ($U_\alpha = 2.00$), all actuator combinations. ($\rho = 10^4$ to $10^{-4.5}$)

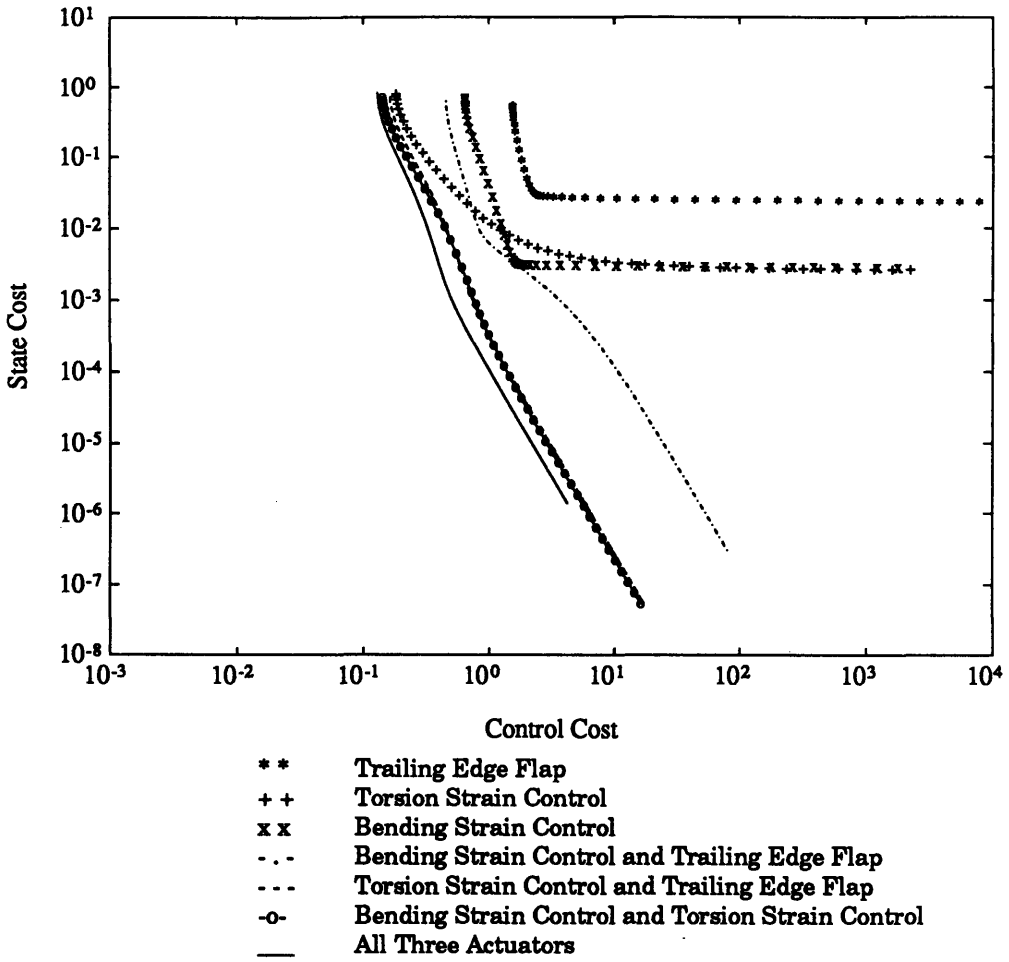

Figure 2.12 Cost curves for all actuator combinations for design point 2 ($U_\alpha = 2.00$). ($\rho = 10^2$ to 10^{-8})

The only new feature is the finite minimum control cost. Since the system is initially unstable and the LQR solution guarantees stability, the solution requires that a minimum amount of control be exerted to stabilize the system. In the cost curves (Figure 2.12), the vertical asymptote that all of the curves approach as control cost is decreased delineates the minimum control that must be exerted to stabilize the system.

Output feedback: Linear Quadratic Gaussian

In this section, the problems of noise and incomplete measurements will be addressed through the design of Linear Quadratic Gaussian (LQG) controllers [Kwakernaak and Sivan, 1972]. While full state feedback provides an optimal controller, realistically, all of the states will not be able to be measured. This leads to the design of output feedback controllers in which only certain combinations of the states are permissible for feedback. The optimal output feedback gains may be obtained through a Linear Quadratic Gaussian method, designing a Kalman filter for use in conjunction with the already designed optimal controller. The Kalman filter estimates the values of the states from the values of the measurements and a model of the plant. Using the state estimates, the controller may operate as though full state feedback has been achieved.

The design of the Kalman filter is the dual problem to the design of the full state feedback controller. In this case, rather than balancing the importance of the state cost against that of the control cost, the process noise is balanced against the measurement noise [Kwakernaak and Sivan, 1972]. If the measurement noise is set to be high relative to the process noise, the measurements will be of less value and the state estimates will be more heavily based on the plant model. In contrast, if the process noise is high compared to the measurement noise, the measurements will be emphasized.

There are three different sets of measurements provided to the system. These include a measurement of the plunge state alone, a measurement of the pitch state alone, and measurements of both the plunge and pitch states. Only displacement measurements are used. The disturbance to the inflow angle, a 1 degree broadband white noise signal, constitutes the process noise. The measurement noise is computed as a percentage of the maximum value

for the given state. Measurement noise levels of 1%, 5%, and 25% have been evaluated. Only the results from the 1% noise level cases are shown in this report, as all of the trends are applicable regardless of noise level. The only significant change between noise levels is that higher measurement noise levels degrade the performance of the entire system, thus having a higher state cost for a given control cost.

To compare and contrast the different measurement systems, the same type of cost analysis as used in the full state feedback case is completed. The state cost is based on the actual states while the control cost is based on the estimated states, as the commands would be based on the estimated states. The weightings and normalizations used for the Linear Quadratic Regulator problem are also used for the Linear Quadratic Gaussian problem.

The cost curves for the various LQG designs did not provide any significant additional information to aide in understanding aeroelastic control. In Figure 2.13, it can be seen that for each of the four actuators, bending strain control, torsion strain control, trailing edge flap, and leading edge flap, the systems which measured both plunge and pitch states consistently performed the best. This is fundamental to any system: the more well-chosen measurements that are available, the more accurate the estimates will be and the better the overall system will perform. Notice that for all four of the actuators, all of the measurement systems have the same low cost asymptote. As the control cost decreases, the system is able to exert decreasing amounts of control, the limiting case being when the controller is unable to exert any control. As the control cost approaches this limit, which measurement system is used will not alter the performance of the system.

If one is limited to using a single measurement, it is marginally better to match the sensor type with the chosen actuator type. For instance, if the

actuator chosen is the trailing edge flap or the bending strain control, the two "plunge" actuators, than it is marginally better to measure the plunge state, specifically at higher control costs. Likewise, the pitch sensor performs the best when used in conjunction with the torsion strain actuator, a "pitch" actuator, although this advantage is weak. Perhaps the most important effect of using a single measurement is that the single actuator curves asymptote to a higher value of state cost at high control costs than when multiple measurements are used. This indicates that the use of a single measurement further limits the performance of controllers using a single actuator.

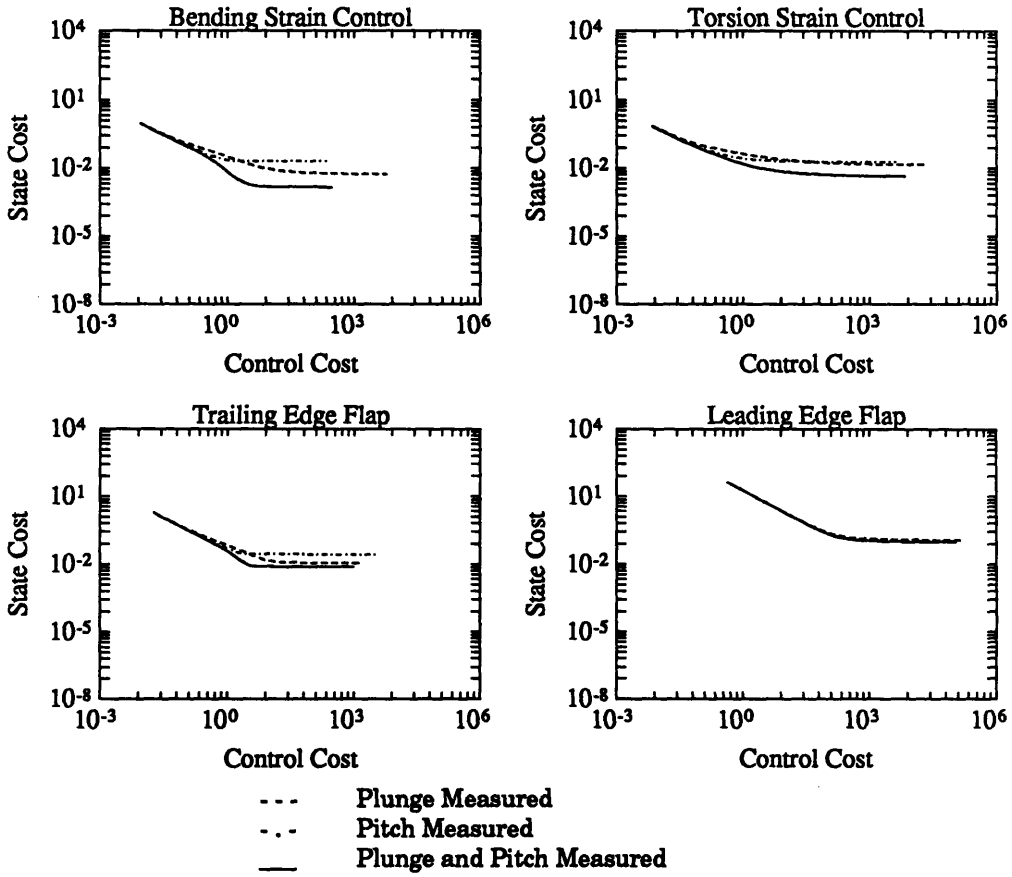

Figure 2.13 Cost curve comparison of different measurement schemes at 1% noise

The designs of controllers using both the Linear Quadratic Regulator method and the Linear Quadratic Gaussian method have revealed several important guidelines. First, controllers using a single actuator exhibit a inherent performance limitation. Second, this limitation is removed when two or more actuators are used. Finally, the use of a single measurement further degrades the performance limitation of the single actuator controllers.

2.4 Fiber vs. Geometric Sweep

In this section, fiber and geometric sweep will be incorporated into the typical section and their effects on the open loop behavior will be studied. To begin, a simple Rayleigh-Ritz formulation will be used to formulate the stiffness matrix with fiber sweep. A transformation will be derived to find the elastic axis location and the uncoupled stiffnesses for the typical section. To incorporate geometric sweep, a second transformation will be derived for the aerodynamic forces. The geometric sweep will only be incorporated into the aerodynamics. Finally, the flutter and divergence characteristics of the typical section with fiber sweep and geometric sweep will be examined.

The first step is to derive the stiffness matrix with fiber sweep. A simple two-mode Rayleigh-Ritz analysis will be used. The sign convention can be seen in Figure 2.14. The two modes are a simple parabolic bending mode and a linear torsional mode.

$$
\begin{aligned}
w(\bar{x},\bar{y},t) &= \sum_{i=1}^{2} \gamma_i(\bar{x},\bar{y}) q_i(t) \\
\gamma_1(\bar{x},\bar{y}) &= \frac{\bar{x}^2}{\tilde{l}^2} \\
\gamma_2(\bar{x},\bar{y}) &= \frac{\bar{x}}{\tilde{l}}\bar{y} \\
\text{where } \tilde{l} &= \frac{3}{4}\bar{l}
\end{aligned}
\tag{2.12}
$$

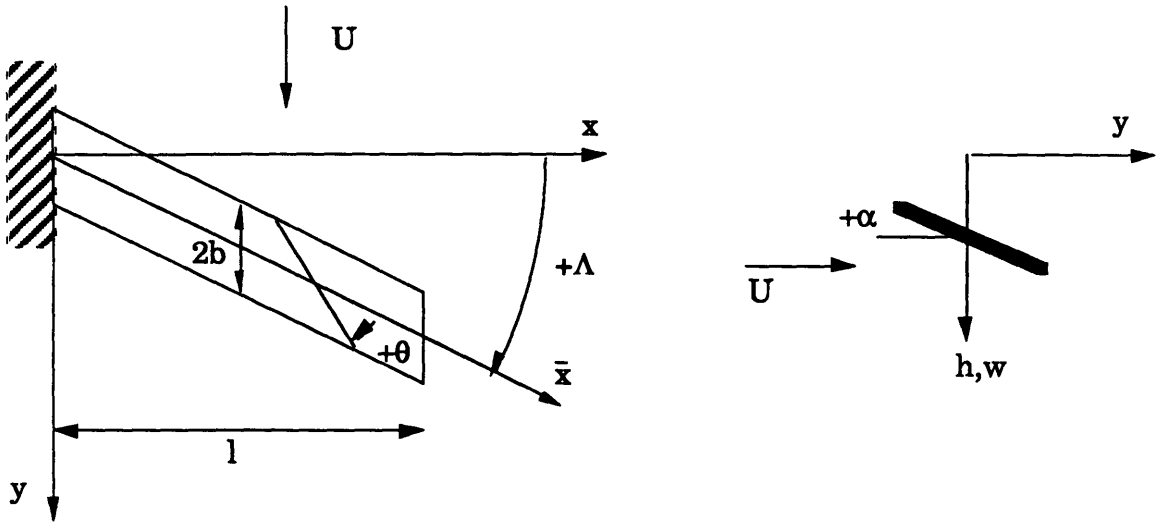

Figure 2.14 Sign convention for Rayleigh-Ritz modeshapes

Note that the barred coordinates are the wing fixed axes and the non-barred coordinates are the reference aerodynamic axes. When evaluated at the 3/4 span point (or $\tilde{l}$), these modes will have unit displacement and unit twist and will be equivalent to the midchord plunge and pitch of the typical section.

$$\begin{aligned} \bar{h}_c(t) &= w\left(\tilde{l},0,t\right) = q_1(t) \\ \frac{\partial \bar{h}_c}{\partial \bar{y}} &= \bar{\alpha}_c(t) = \frac{\partial w}{\partial \bar{y}}\left(\tilde{l},0,t\right) = q_2(t) \\ \frac{\partial \bar{h}_c}{\partial \bar{x}} &= \frac{\partial w}{\partial \bar{x}}\left(\tilde{l},0,t\right) \end{aligned} \tag{2.13}$$

The typical section defines displacement positive down and positive angle is leading edge up (Figure 2.14).

These modeshapes are then integrated over the wing to obtain the stiffness matrix.

$$\mathbf{K} = \begin{bmatrix} \frac{4\tilde{l}\bar{c}}{\tilde{l}^4} D_{11} & \frac{4\tilde{l}\bar{c}}{\tilde{l}^3} D_{16} \\ \frac{4\tilde{l}\bar{c}}{\tilde{l}^3} D_{16} & \frac{4\tilde{l}\bar{c}}{\tilde{l}^2} D_{66} \end{bmatrix} \tag{2.14}$$

where $D_{ij} = \frac{1}{3}\sum_{k=1}^{N}(Q_{ij})_k(z_k^3 - z_{k-1}^3)$

$(Q_{ij})_k$ is the modulus of the kth layer

z_k is the height of the kth layer

N is the total number of layers

No chordwise bending mode has been included and the stiffness matrix depends only on spanwise bending and torsional stiffnesses and their coupling term.

To incorporate this coupled stiffness matrix into the typical section equations, an elastic axis location and the corresponding uncoupled stiffness matrix must be found. The spring forces have been evaluated at the midchord and need to be transformed to the elastic axis location. The typical section equations are defined per unit span, so the stiffnesses in Equation 2.14 must first be divided by the span $\bar{l}$. Then, a transformation matrix is established between the displacements at the midchord and those at the elastic axis (Figure 2.1).

$$\begin{Bmatrix} q_1 \\ q_2 \end{Bmatrix} = \begin{Bmatrix} \bar{h}_c \\ \bar{\alpha}_c \end{Bmatrix} = \begin{bmatrix} 1 & -a\bar{b} \\ 0 & 1 \end{bmatrix} \begin{Bmatrix} \bar{h}_{E.A.} \\ \bar{\alpha}_{E.A.} \end{Bmatrix} = \mathbf{T} \begin{Bmatrix} \bar{h}_{E.A.} \\ \bar{\alpha}_{E.A.} \end{Bmatrix} \tag{2.15}$$

The distance of the elastic axis aft of the midchord, $a\bar{b}$, is unknown. The spring forces at the elastic axis are calculated through the appropriate transformation for equilibrium equations using the same transformation matrix **T** [Strang, 1986].

$$\begin{Bmatrix} \bar{F}_{E.A.} \\ \bar{M}_{E.A.} \end{Bmatrix} = \left(\frac{1}{\bar{l}}\right) \mathbf{T}^{\mathrm{T}} \mathbf{K} \mathbf{T} \begin{Bmatrix} \bar{h}_{E.A.} \\ \bar{\alpha}_{E.A.} \end{Bmatrix} \tag{2.16}$$

The transformation preserves the system dynamics. Eliminating the resulting cross stiffnesses provides the expression for the elastic axis location

and the uncoupled stiffnesses (Equation 2.17). By definition, the elastic axis is the position at which the stiffnesses uncouple. The location of the elastic axis and the uncoupled stiffnesses are found by setting the off-diagonal terms of $\mathbf{T}^{\mathbf{T}}\mathbf{K}\mathbf{T}$ to zero.

$$
\begin{aligned}
a &= \frac{K_{12}}{K_{11}\bar{b}} = \frac{3}{4}\frac{\bar{l}}{\bar{b}}\frac{D_{16}}{D_{11}} \\
K_h &= \frac{K_{11}}{\bar{l}} = \frac{4\bar{c}}{\bar{l}^4}D_{11} \\
K_\alpha &= \frac{K_{22}}{\bar{l}}\left(1-\frac{K_{12}^2}{K_{11}K_{22}}\right) = \frac{4\bar{c}}{\bar{l}^2}D_{66}\left(1-\frac{D_{16}^2}{D_{11}D_{66}}\right)
\end{aligned}
\tag{2.17}
$$

These uncoupled stiffnesses can be placed directly into the governing equations of motion for the typical section (Equation 2.2).

Using a simple six-ply laminate, the relationship between fiber sweep angle and elastic axis location can be shown. The stiffnesses are calculated using plates with six plies of AS4/3501-6 graphite epoxy with all plies at the fiber sweep angle (see Appendix B for material properties). Figure 2.15 shows the elastic axis location for varying fiber angle for a full span aspect ratio of 3.92, like the reference typical section, and for an aspect ratio of 8. Both aspect ratios show linear trends until a fiber sweep angle of approximately -55 degrees. At this point, bend-twist coupling is decreased for increasing fiber sweep angles. Eventually the fiber sweep angle will be 90 degrees with no bend-twist coupling. To achieve a reasonable level of bend-twist coupling, fiber sweep angles of +/- 15 to +/- 45 degrees should be used.

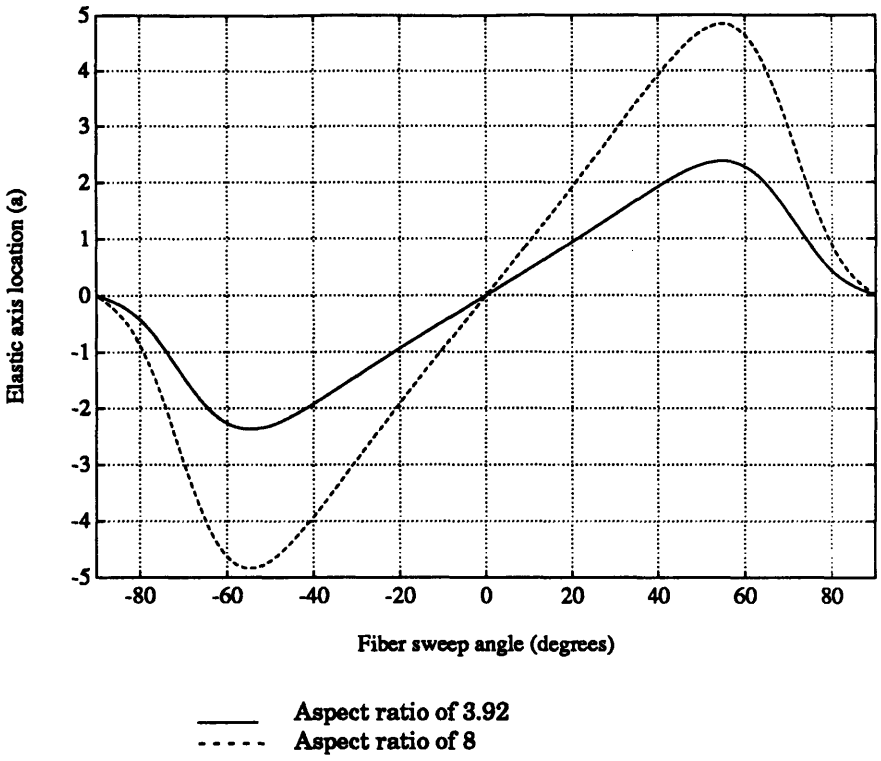

Figure 2.15 Location of elastic axis for varying fiber sweep angle. ab is the distance of the elastic axis aft of the midchord, where b is the semichord.

To incorporate geometric sweep into the aerodynamics, a correction must be made on the lift-curve slope and the aerodynamic coupling of bending and torsion must be included. Without any corrections for sweep, the static aerodynamic forces are only due to the twist angle or angle of attack.

$$\begin{Bmatrix} F_c \\ M_{c_y} \\ M_{c_x} \end{Bmatrix} = \begin{bmatrix} 0 & 0 & -\rho U^2 b C_{L_\alpha} \\ 0 & 0 & 0 \\ 0 & 0 & \rho U^2 e b C_{L_\alpha} \end{bmatrix} \begin{Bmatrix} h_c \\ \dfrac{\partial h_c}{\partial x} \\ \dfrac{\partial h_c}{\partial y} \end{Bmatrix} \tag{2.18}$$

where e is the distance from the aerodynamic center to the midchord

and $\alpha_c = \dfrac{\partial h_c}{\partial y}$

There are several corrections to the aerodynamic forces that must be made for the incorporation of geometric sweep. First, there is a cos Λ correction on the lift curve slope. Second, the geometry of the strip is altered. Spanwise dimensions are shortened and chordwise dimensions are lengthened. The chordwise dimensions in the aerodynamic strip forces are explicit, but, since the strip forces are calculated for a unit span, the spanwise dimension is implicit.

$$\begin{Bmatrix} F_c \\ M_{c_y} \\ M_{c_x} \end{Bmatrix} = \begin{bmatrix} 0 & 0 & -\rho U^2 \left(\frac{\bar{b}}{\cos\Lambda}\right)\left(C_{L_\alpha}\cos\Lambda\right)\left(\Delta\bar{x}\cos\Lambda\right) \\ 0 & 0 & 0 \\ 0 & 0 & \rho U^2 \left(\frac{\bar{e}}{\cos\Lambda}\right)\left(\frac{\bar{b}}{\cos\Lambda}\right)\left(C_{L_\alpha}\cos\Lambda\right)\left(\Delta\bar{x}\cos\Lambda\right) \end{bmatrix} \begin{Bmatrix} h_c \\ \frac{\partial h_c}{\partial x} \\ \frac{\partial h_c}{\partial y} \end{Bmatrix} = \mathbf{A} \begin{Bmatrix} h_c \\ \frac{\partial h_c}{\partial x} \\ \frac{\partial h_c}{\partial y} \end{Bmatrix}$$

where bars indicate dimensions in the wing fixed axes

$\Delta\bar{x} = 1$

and $\alpha_c = \frac{\partial h_c}{\partial y}$

(2.19)

The final correction to the aerodynamic forces for geometric sweep is a transformation of coordinates from the wind axes (x, y) to the wing axes $(\bar{x}, \bar{y})$ is shown in Figure 2.16 and Equations 2.20 .

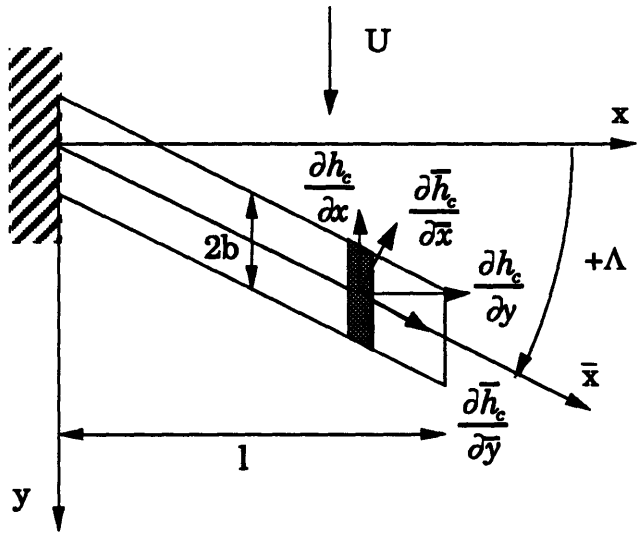

Figure 2.16 Transformation of coordinates for addition of geometric sweep

$$\begin{Bmatrix} h_c \\ \frac{\partial h_c}{\partial x} \\ \frac{\partial h_c}{\partial y} \end{Bmatrix} = \begin{bmatrix} 1 & 0 & 0 \\ 0 & \cos\Lambda & -\sin\Lambda \\ 0 & \sin\Lambda & \cos\Lambda \end{bmatrix} \begin{Bmatrix} \bar{h}_c \\ \frac{\partial \bar{h}_c}{\partial \bar{x}} \\ \frac{\partial \bar{h}_c}{\partial \bar{y}} \end{Bmatrix} = \mathbf{T}_\mathbf{A} \begin{Bmatrix} \bar{h}_c \\ \frac{\partial \bar{h}_c}{\partial \bar{x}} \\ \frac{\partial \bar{h}_c}{\partial \bar{y}} \end{Bmatrix} \tag{2.20}$$

The inclusion of geometric sweep couples the bending and twisting displacements in the wind axes. The aerodynamic transformation matrix, T_A, may now be used to transform the aerodynamic forces and moments to the wing fixed axes.

$$\begin{Bmatrix} \bar{F}_c \\ \bar{M}_{c_y} \\ \bar{M}_{c_z} \end{Bmatrix} = \mathbf{T}_\mathbf{A}^\mathbf{T} \mathbf{A} \mathbf{T}_\mathbf{A} \begin{Bmatrix} \bar{h}_c \\ \frac{\partial \bar{h}_c}{\partial \bar{x}} \\ \frac{\partial \bar{h}_c}{\partial \bar{y}} \end{Bmatrix} \tag{2.21}$$

The typical section equations of motion have only two degrees of freedom, a plunge motion (q_1) and a pitch motion (q_2). The displacement and slopes must be expressed in terms of the two degrees of freedom and the generalized aerodynamic forces on these two degrees of freedom must be found. Recalling Equations 2.13, the appropriate transformation matrix is

$$\begin{Bmatrix} \bar{h}_c \\ \frac{\partial \bar{h}_c}{\partial \bar{x}} \\ \frac{\partial \bar{h}_c}{\partial \bar{y}} \end{Bmatrix} = \begin{bmatrix} \gamma_1(\tilde{l},0,t) & 0 \\ \frac{\partial \gamma_1}{\partial \bar{x}}(\tilde{l},0,t) & 0 \\ 0 & \frac{\partial \gamma_2}{\partial \bar{y}}(\tilde{l},0,t) \end{bmatrix} \begin{Bmatrix} q_1 \\ q_2 \end{Bmatrix} = \mathbf{T}_\mathbf{M} \begin{Bmatrix} q_1 \\ q_2 \end{Bmatrix} \tag{2.22}$$

Consequently, the generalized aerodynamic forces on the plunge and pitch modes are

$$\begin{Bmatrix} Q_1 \\ Q_2 \end{Bmatrix} = \mathbf{T}_\mathbf{M}^\mathbf{T} \mathbf{T}_\mathbf{A}^\mathbf{T} \mathbf{A} \mathbf{T}_\mathbf{A} \mathbf{T}_\mathbf{M} \begin{Bmatrix} q_1 \\ q_2 \end{Bmatrix} \tag{2.23}$$

These transformations are only applied to the aerodynamic forces as the remainder of the forces are already defined in the wing axes on the plunge

and pitch displacements. Now the aerodynamic forces are described in the wing axes, defined about the midchord, and expressed in terms of the plunge and pitch displacements. The aerodynamic forces must now be transformed to the elastic axis location by the earlier transformation (Equation 2.15) from the midchord to the elastic axis to be consistent with the other forces in the equation of motion.

$$\begin{bmatrix} m & mx_\alpha b \\ mx_\alpha b & I_\alpha \end{bmatrix} \begin{Bmatrix} \ddot{\bar{h}}_{E.A.} \\ \ddot{\bar{\alpha}}_{E.A.} \end{Bmatrix} + \begin{bmatrix} K_{11} & 0 \\ 0 & K_{22}\left(1 - \dfrac{K_{12}^2}{K_{11}K_{22}}\right) \end{bmatrix} \begin{Bmatrix} \bar{h}_{E.A.} \\ \bar{\alpha}_{E.A.} \end{Bmatrix} + \mathbf{T}^{\mathrm{T}}\mathbf{T}_{\mathbf{M}}^{\mathrm{T}}\mathbf{T}_{\mathbf{A}}^{\mathrm{T}}\mathbf{A}\mathbf{T}_{\mathbf{A}}\mathbf{T}_{\mathbf{M}}\mathbf{T} \begin{Bmatrix} \bar{h}_{E.A.} \\ \bar{\alpha}_{E.A.} \end{Bmatrix} = \mathbf{0} \tag{2.24}$$

Now that the geometric and fiber sweep have been incorporated into the typical section equations, the stability behavior of the section for varying geometric and fiber sweep can be studied. Choosing realistic values of sweep, a trade space which includes geometric sweep angles of -30, 0, and 30 degrees and fiber sweep angles of -45, -30, -15, 0, 15, 30, and 45 degrees is established. Using a velocity iteration and solving for the roots of the characteristic equation, the stability characteristics of the trade space can be found by examining Figure 2.17.

To see the accuracy of the typical section analysis, the physical parameters used correspond to plates used in a study by Landsberger and Dugundji [1985]. Essentially the same trends appear using the typical section analysis as seen in Figure 7 of Landsberger and Dugundji, noting the different definition of positive fiber sweep angle. Wings with aft geometric sweep and negative fiber sweep show a remarkable robustness to change in fiber and geometric sweep. These sections all flutter and the variation in flutter speed is not large. In contrast, the forward swept wing with negative sweep angles is divergence prone and the speeds vary greatly for change in

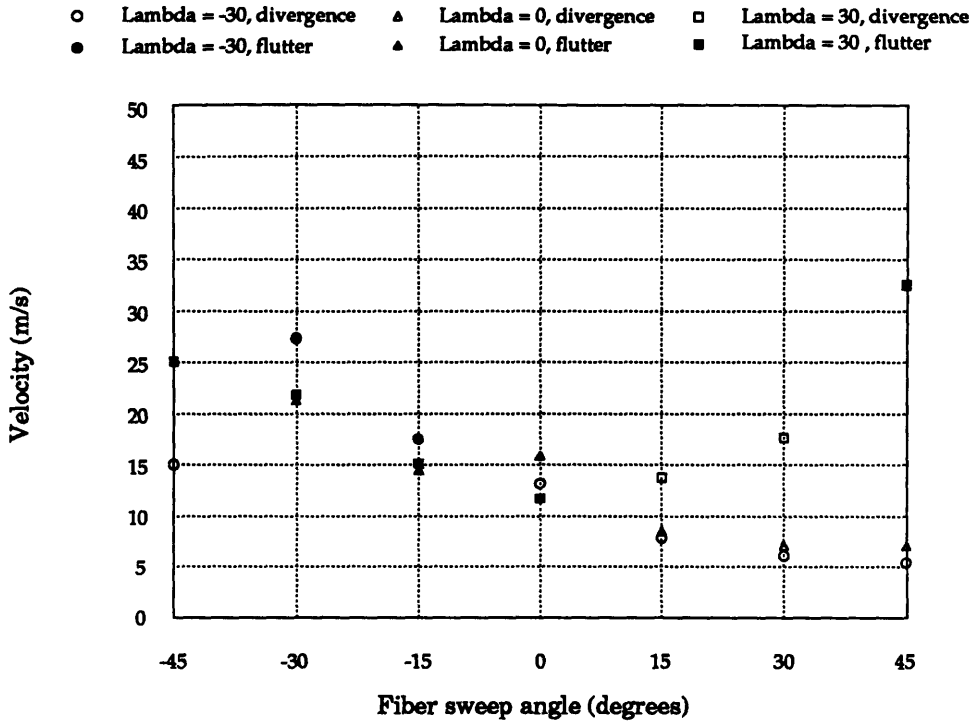

Figure 2.17 Typical section stability characteristics for varying geometric and fiber sweep angles. The data points for a fiber sweep angle of -45 degrees and geometric sweep angles of 0 and 30 degrees are superimposed.

fiber sweep. Likewise, the positive fiber sweep angles are also divergence prone.

The discrepancies between the typical section analysis and Landsberger and Dugundji's results are due to three modelling assumptions. First, and foremost, is the lack of chordwise bending modelled in the typical section. Jensen [1982] showed that the inclusion of a chordwise bending mode in a Rayleigh-Ritz anlaysis is significant in correctly determining the frequencies of bend-twist coupled plates. Second, only steady aerodynamics have been included in the typical section model. Finally, a minor difference is the fact that the laminates used in the typical section are $[\theta_6]$ and the laminates used in Landsberger and Dugundji are $[\theta/\theta/0]s$.

The simple two degree of freedom model used in this section to analyze the effects of fiber sweep and geometric sweep provided remarkably accurate results. The trends compared favorably with previous analytical and experimental results. A region in which the test article will consistently flutter and where the flutter speeds are robust to small changes in either fiber or geometrical sweep has been found.

2.5 Robustness of Qualitative Results: Parameter Variation

Since the main emphasis of the typical section exercise is to achieve better physical insight into the problem of aeroelastic control, it is important to check the robustness of the qualitative results to parameter variation. To a certain extent, this has already been completed, with the study of design point 2. This section will examine the change in the open loop plant to change in nominal physical parameters. The first change is to alter the spacing between the elastic axis and the center of gravity. The second is to alter the location of the elastic axis/center of gravity pair, holding their internal spacing constant.

For the first series of parameter variations, the spacing between the elastic axis and the center of gravity is changed. The parameters that must be consistently altered are x_α, the distance from the elastic axis to the center of gravity, which is non-dimensionalized by the semichord and the radius of gyration, R_α^2. The radius of gyration, much like a moment of inertia, is comprised of two components: one which represents the distribution of mass about the center of gravity and another which represents the parallel axis contribution of the distance from the center of gravity to the axis of rotation, or the elastic axis. Only the parallel axis portion is altered. This

parametrization corresponds to redistribution of mass in the wing while keeping the stiffness constant.

As can be seen from Figure 2.18, five different spacings, including the nominal case, are examined. The first alteration ($x_\alpha = -0.2$) has the center of gravity located ahead of the elastic axis. The second case ($x_\alpha = 0$) has the center of gravity superimposed on the elastic axis. The final two cases ($x_\alpha = 0.4$ and $x_\alpha = 0.6$) have the center of gravity located behind the elastic axis, similar to the nominal case.

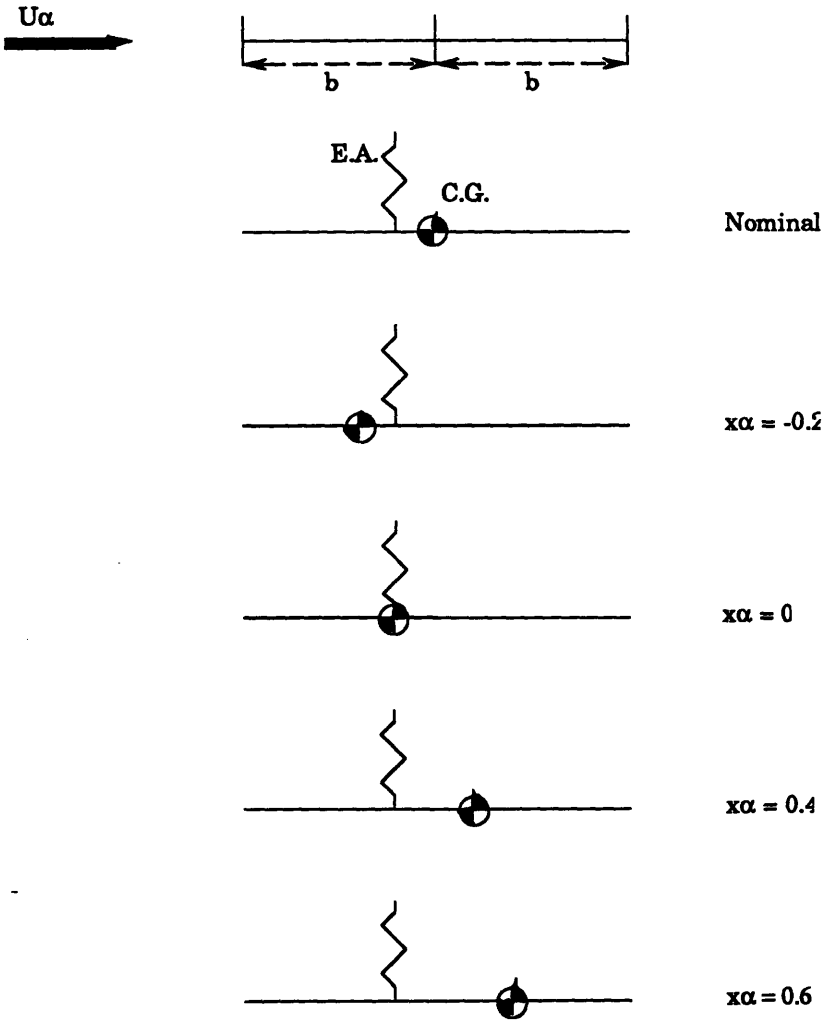

Figure 2.18 Parameter variation on the spacing between elastic axis and center of gravity

To examine the effects of these parameter changes on the open loop plant, the pattern of poles and zeros as they move with airspeed will be examined and qualitatively compared to the nominal case (Figure 2.19). For all of the cases in which the center of gravity is aft of the elastic axis, the pattern is qualitatively similar. The case in which the center of gravity is superimposed on the elastic axis shows a significantly different pattern. Since the two are superimposed and only steady aerodynamics are being used, the two modes are completely decoupled and flutter never occurs. Likewise, when the center of gravity is ahead of the elastic axis, flutter never occurs. Both of these cases are uninteresting in the design of aeroelastic control for flutter. These results are consistent with the typical section parameter variations in Bisplinghoff, Ashley, and Halfman [1955]

The second series of parameter variations involve the movement of the elastic axis/center of gravity pair. This parametrization reflects a change in stiffness and a change in mass distribution. The parameters that must be consistently altered are a, the distance from the midchord to the elastic axis, which is non-dimensionalized by the semichord and all of the aerodynamic moment coefficients, which change when a is changed. The five different locations tried are shown in Figure 2.20.

As before, the open loop plant with the varied parameters will be studied by observing the changing pole/zero pattern (Figure 2.21). The cases in which the elastic axis/center of gravity pair is located aft of the nominal case evidence patterns qualitatively similar to the nominal case (a = 0 and a = 0.2). With $a = -0.4$ and the elastic axis/center of gravity pair entirely ahead of the midchord, the pattern changes slightly with the trailing edge flap zero starting above both poles at zero velocity and crossing over to be between the two poles and finally to zero frequency before flutter. This would

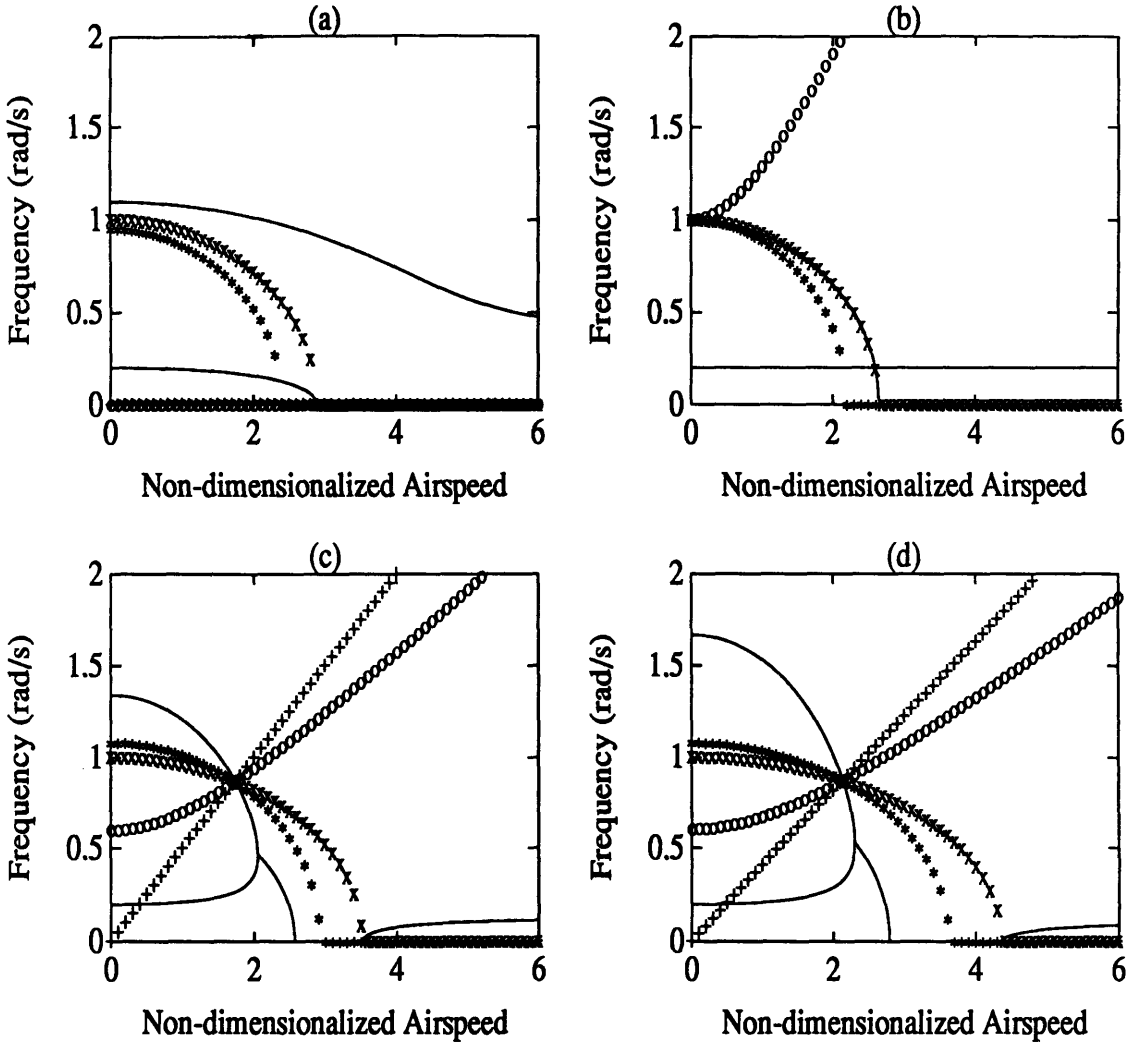

Figure 2.19 Pole/zero movement with respect to the non-dimensional airspeed, U_{α}, for the variation of the spacing between the elastic axis and the center of gravity. Cases are as follows: (a) x_{α} = -0.2, (b) x_{α} = 0, (c) x_{α} = 0.4, (d) x_{α} = 0.6

mean that the pole/zero pattern for the design points studied would be qualitatively different for this actuator; it also seems to indicate that aileron reversal occurs much earlier and may precede flutter. With $a = -0.6$ and the elastic axis ahead of the center of pressure, the same pattern occurs for the trailing edge flap zero, with reversal occurring well before flutter.

Additionally, the bending strain actuator zero continually increases in frequency as opposed to its normal decreasing behavior. However, the pole/zero patterns for this actuator do not change for either of the design points.

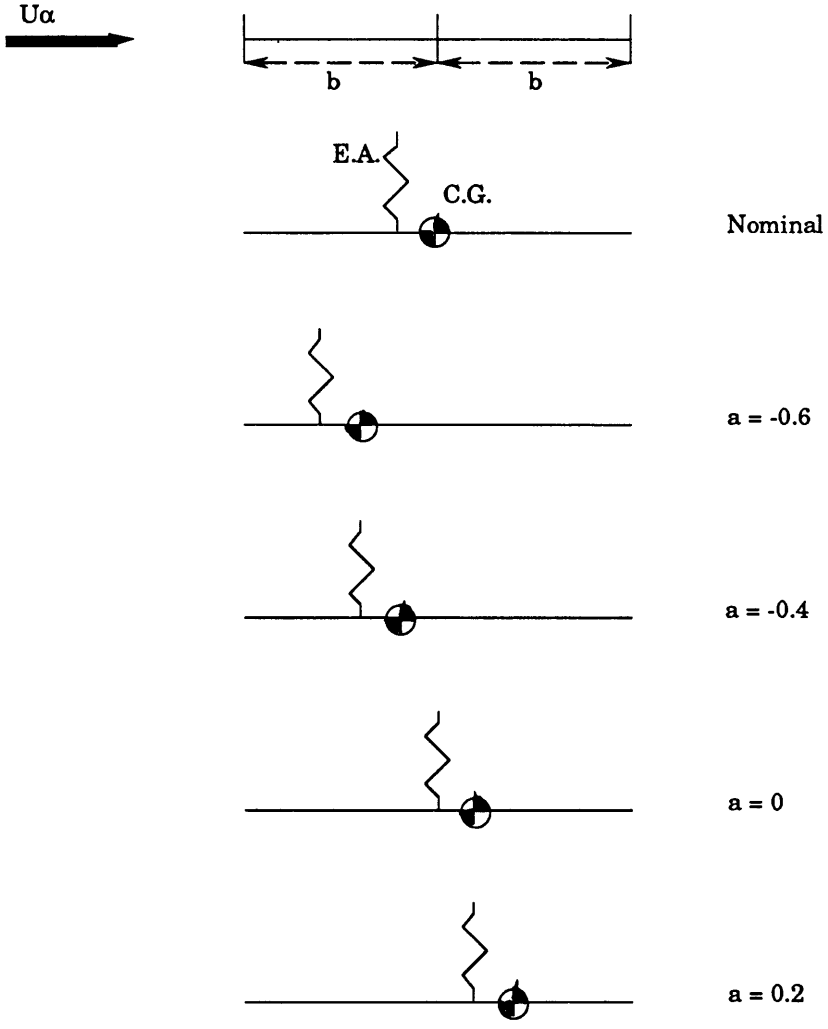

Figure 2.20 Parameter variation on location of elastic axis / center of gravity pair.

The parameter changes outlined in this section and the resulting changes in the open loop plant indicate that the lessons learned earlier from the reference case would be able to be applied to many typical sections. These typical sections must have the center of gravity located aft of the

elastic axis. Another constraint is that the elastic axis must be located aft of the center of pressure.

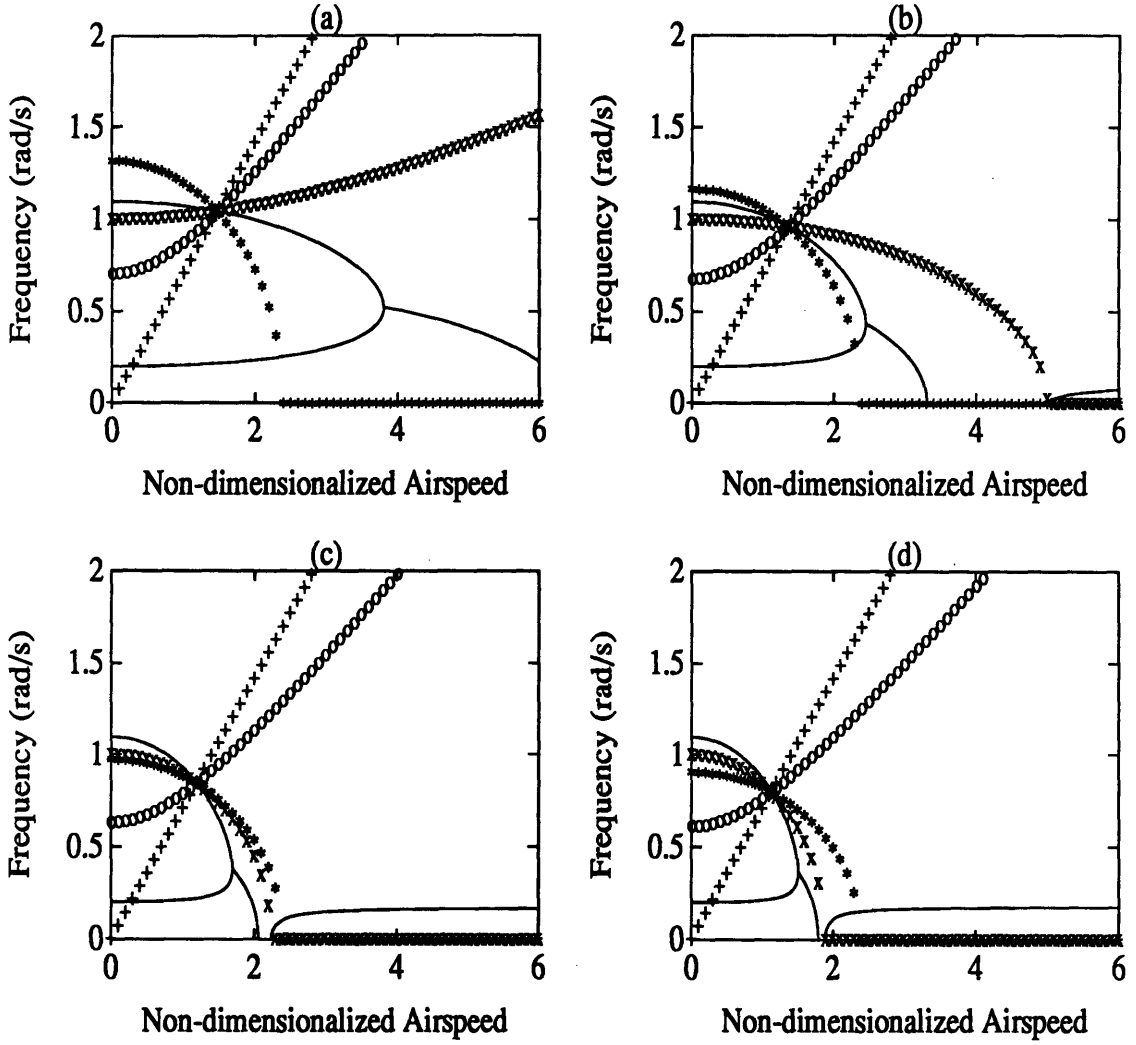

Figure 2.21 Pole/zero movement with respect to non-dimensional airspeed, U_α, for variation of location of elastic axis/center of gravity pair. Cases are as follows: (a) a = -0.6, (b) a = -0.4, (c) a = 0, (d) a = 0.2

2.6 Incorporation of unsteady aerodynamics

In a final attempt to verify the generality of the qualitative results, full unsteady aerodynamics will be incorporated. Returning to the full expressions for lift and moment, all of the non-circulatory terms as well as any circulatory rate or acceleration terms must now be included. In addition, Theodorsen's function, $C(k)$, must be implemented with its complex frequency dependent nature. To accomplish this, a rational approximation will be used.

For the present purposes of control design, the simplest rational approximation is a one pole approximation matched exactly to the tabular values for Theodorsen's function at a reduced frequency of $k = 0.5$.

$$C(s) = 1 + \frac{-0.4544s}{s + 0.1902} \tag{2.25}$$

This reduced frequency corresponds to design point 1. The fit of this approximation to the tabular values can be seen in Figure 2.22.

By representing Theodorsen's function by a pole approximation, new states must be added to the system. These states act as aerodynamic lags, or lag states. The new states are defined as follows

$$\begin{aligned} \hat{x} &= \frac{s}{s + 0.1902} x \qquad \text{or} \\ \hat{x}p &= xp - 0.1902 U_\alpha \hat{x} \end{aligned} \tag{2.26}$$

Only one additional lag state is required for each displacement state, so the total number of states is increased to six. Once these lags are incorporated, the aerodynamic coefficients for displacements, rates, and accelerations can be derived and these are shown, along with their values for the nominal typical section in Appendix A.

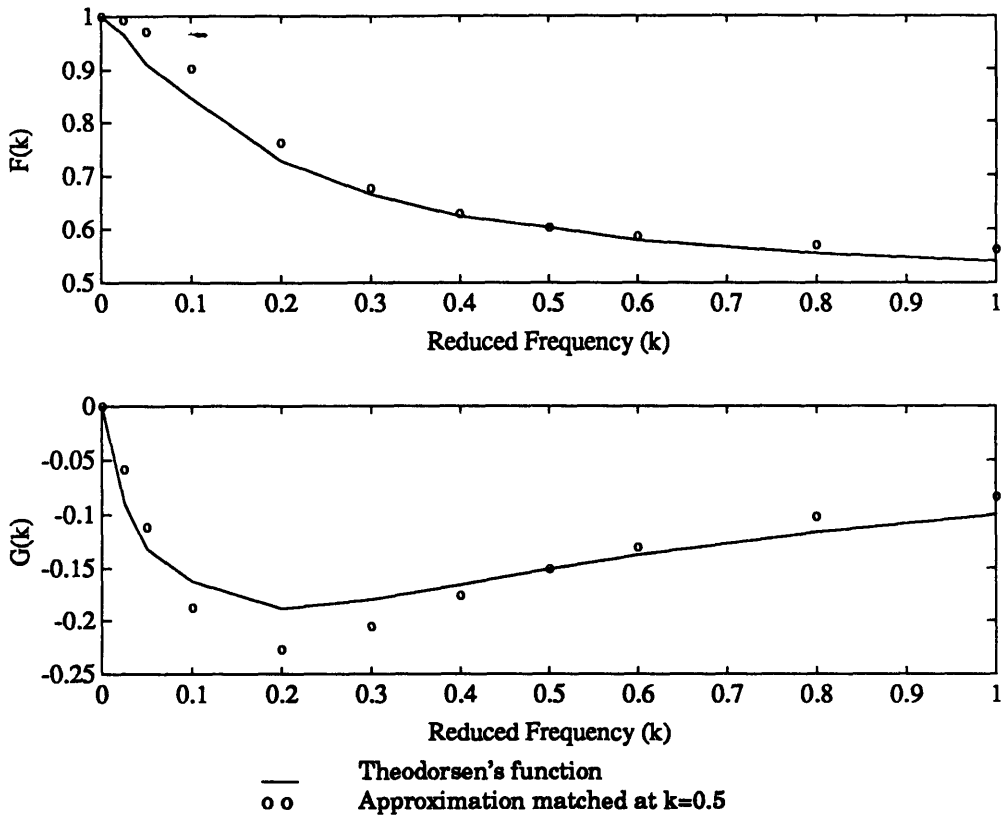

Figure 2.22 Comparison of one-pole approximations to the tabulated values of Theodorsen's function

To implement the lag state and to provide rate and acceleration terms for the trailing edge flap angle, the trailing edge flap has to be given some dynamics. A simple model of the trailing edge flap is created, a 2 d.o.f. spring-mass-dashpot system with critical damping and a natural frequency 100 times greater than the torsional mode of the typical section. In this manner, the flap dynamics will not interfere with the main flutter phenomenon.

$$\ddot{\beta} + 98.994\dot{\beta} + 4900\beta = 4900\beta_o \qquad (2.27)$$

where β_o is the commanded flap angle

The aerodynamic lag for the flap is implemented in exactly the same manner as the aerodynamic lags on the displacement states. The addition of the flap

dynamics and lag state completes the full nine state system. The full matrix equation of motion may be seen in Appendix A.

Solving the matrix eigenvalue problem, the plunge and pitch mode poles may be plotted as the airspeed varies (Figure 2.23). The flutter point, when one of the poles crosses into the right half plane, is clearly visible. The modes have essentially coalesced and the mode which eventually goes unstable is a combination of both the bending mode and the torsion mode.

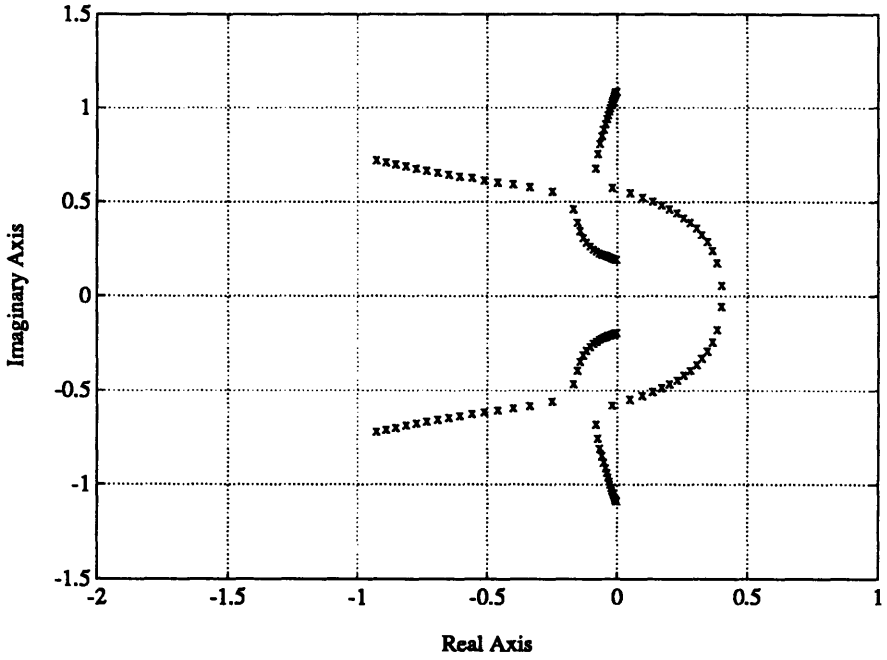

Figure 2.23 Pole movement with change in airspeed for nominal typical section, unsteady aerodynamics.

The movement of the open loop single input-single output poles and zeros as airspeed varies with unsteady aerodynamics can be compared to the steady case (Figure 2.4 and Figure 2.24). The most obvious difference is that two of the zeros from the pitch output transfer functions move with change in airspeed when unsteady aerodynamics are included. The second notable difference is the trailing edge flap input/plunge output zero. It follows the same pattern that it did for sections with the elastic axis/center of gravity

pair ahead of the midchord: it begins initially above both poles and then crosses to lie between the poles before flutter. Overlooking these two disparities, the unsteady case and the steady case do look remarkably similar. They both follow the same general pattern and the multiple crossing point is again evident and indicates unobservability of the torsional mode with plunge measurement at that velocity. To see how the disparities effect control design, LQR designs are created for the different actuation schemes with unsteady aerodynamics.

The LQR designs for the unsteady case closely parallel those for the steady case. The same states are weighted in the cost functionals and the same normalizations are used for both the states and the controls. Looking at the closed loop pole loci, many of the same qualitative characteristics are evident (Figure 2.25). For example, all of the single actuator designs show the same performance limitation as before. Each single actuator moves one pole along a stable Butterworth pattern and the other pole is pushed toward a finite location in the left half plane, the location of a finite zero of the full Hamiltonian system. A difference here is that the same pole is always moved along the Butterworth pattern, regardless of actuator. This behavior obscures any "typing" of actuators. In addition, the pole loci of the multiple actuator designs demonstrate the same removal of any performance limitations. Both of the poles may now be moved along stable Butterworth patterns. As before, the combination of all actuators does not perform significantly better than the best pair of actuators, indicating that two well chosen actuators control the section effectively.

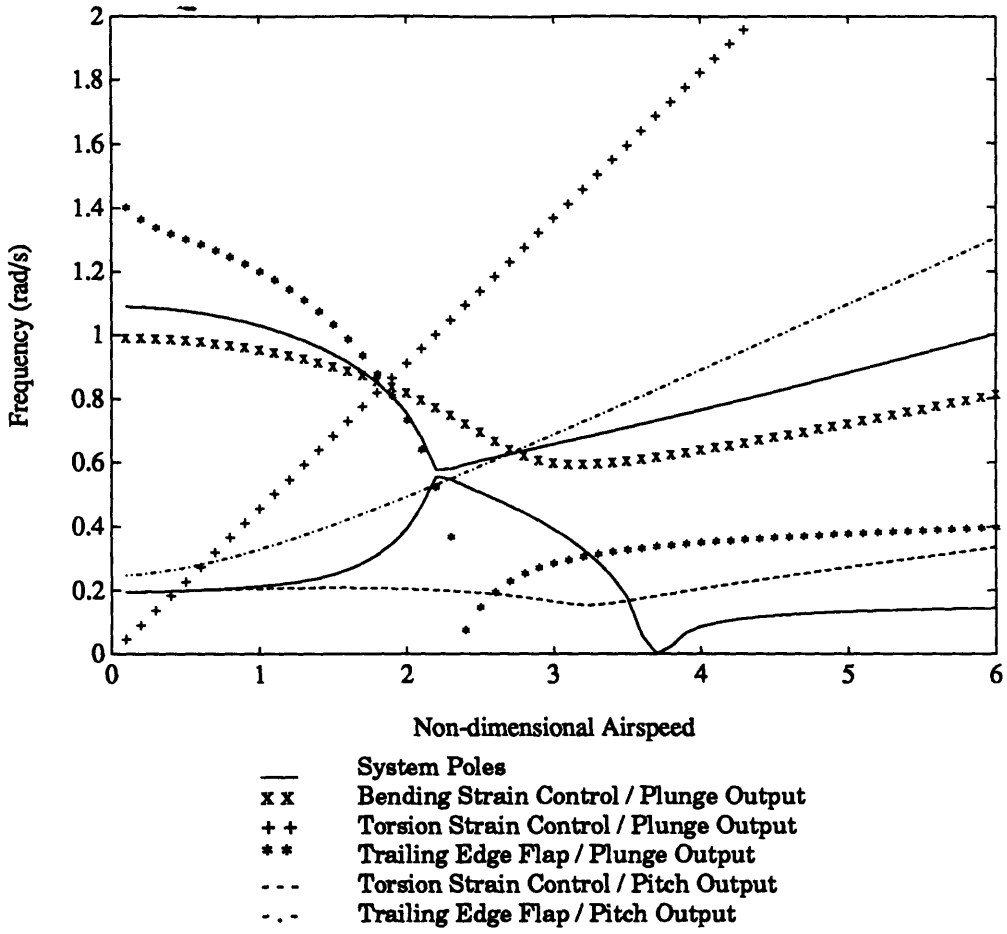

Figure 2.24 Pole/zero movement with respect to non-dimensional airspeed, U_α, for nominal typical section with unsteady aerodynamics.

These same results are echoed in the cost analysis of the unsteady aerodynamics controller designs (Figure 2.26). The performance limitation of the single actuator systems again appears as the single actuator curves asymptote out to a finite state cost for increasing control cost. The bending strain actuator proves to be the most effective of the three actuators, although all three are relatively close. As seen repeatedly before, the multiple actuator combinations do not exhibit the performance limitation. All of the curves also approach a low control cost horizontal asymptote indicating that the system's state cost will never increase above that level, regardless of

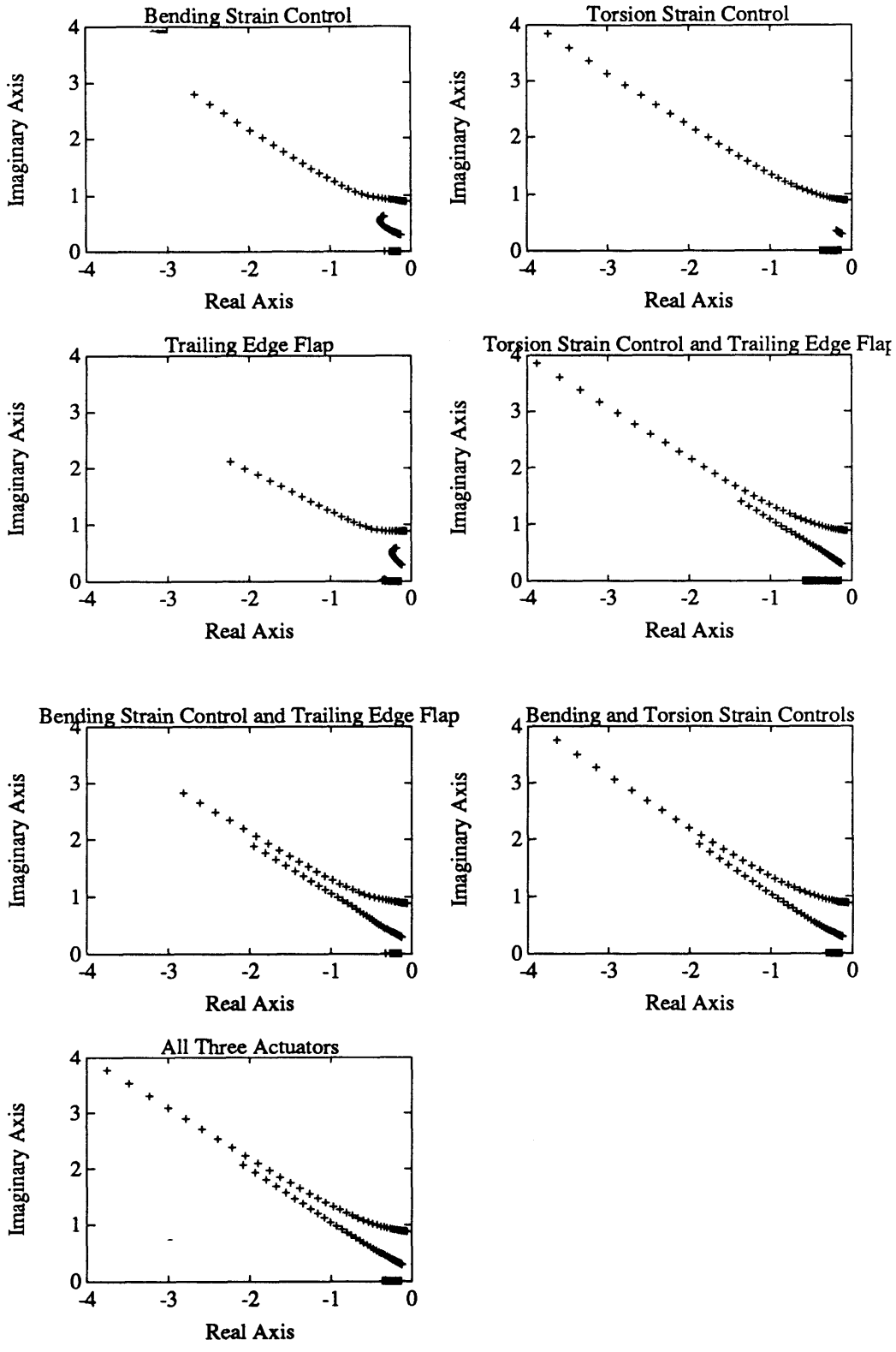

Figure 2.25 Loci of LQR closed loop poles for all combinations of actuators at design point 1, unsteady aerodynamics.

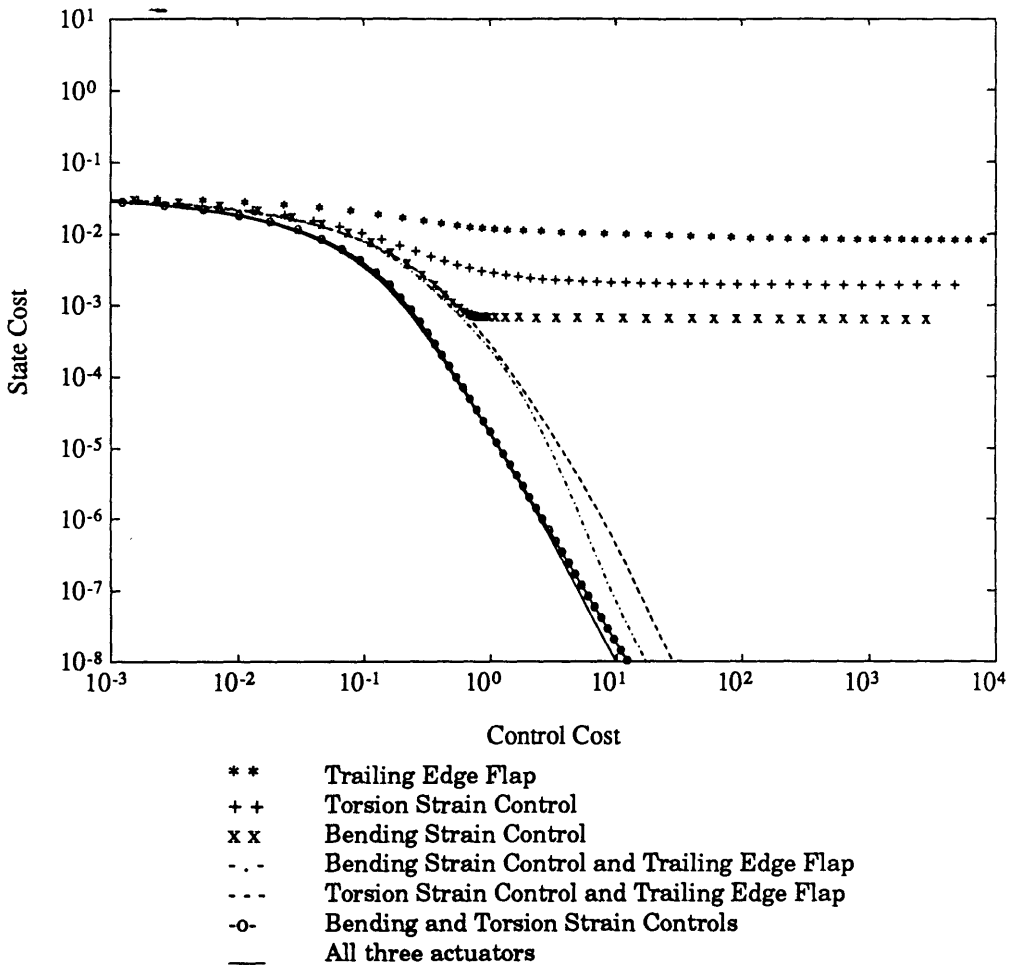

Figure 2.26 State cost vs. Control cost for nominal plant with unsteady aerodynamics at design point 1.

how little control is used. This is due to the presence of a finite amount of damping in the unsteady aerodynamics case.

Overall, the same qualitative trends seem to hold for the unsteady aerodynamics case as compared to the steady aerodynamics case. The same fundamental principle is observed: it is important to have as many effective actuators as vital modes and any additional actuators will show a greatly decreased return. In addition to the parameter variations described earlier, this comparison verifies the generalities of the results achieved.

2.7 Summary

In this chapter, strain actuation for aeroelastic control has been studied through the use of a typical section. The parametric equations of motion have been derived using two degrees of freedom: pitch and plunge. Strain actuators and conventional flap actuators have been modelled and controllers designed using these actuators in various combinations. It has been shown that single actuator designs reach a fundamental performance limit when controlling this two degree of freedom system. In addition, controllers using more than two actuators did not perform significantly better than the best combination of two actuators. Therefore, as a guiding principle, it is important to have as many effective actuators as important modes. As for the individual actuators, all of the actuators, save the leading edge flap, demonstrated nearly equivalent performance levels. The leading edge flap proved to be an ineffective actuator.

Following the controller analysis, the effect of geometric and fiber sweep on the open loop stability characteristics of the typical section was shown. The elastic axis location demonstrated essentially linear behavior for change in fiber sweep angle up to 55 degrees. Negative fiber sweep angles (forward with reference to the wing fixed axes) and aft geometric sweep angles guaranteed flutter as the first instability and showed small variances in flutter speed.

Finally, the results were verified using simple parameter variations and unsteady aerodynamics. The open loop behavior was consistent throughout the parameter changes so long as the center of gravity is aft of the elastic axis and the elastic axis is aft of the center of pressure. Likewise, the incorporation of unsteady aerodynamics did not affect the actuation trends derived earlier using steady aerodynamics.

Building the Design

Chapter 3: Functional Requirements and Design Parameters

3.1 Introduction

The previous chapter provides the foundation for the design of the demonstration phase test article. The typical section analyses show that piezoelectric actuators are a viable alternative to conventional flap actuators. In addition, the typical section analyses demonstrate that at least as many actuators as there are important aeroelastic modes are necessary for effective control. These guidelines will now be applied to the design of the demonstration phase test article.

In a rigorous design process, preliminary design is preceded by the establishment of the working requirements for the device. Oftentimes, for smaller projects, this step need not be explicit; instead, the requirements are internalized by a single designer. For larger projects with design teams, the requirements must be formalized. The first section of this chapter identifies the functional requirements of the demonstration phase test article. Once these requirements have been determined, the next step is to enumerate the design parameters. The design parameters are those parameters which can be varied so that the design meets the functional requirements [Suh, 1990].

The process of preliminary design is to establish the values of these parameters. These values will be arrived at by non-parametric studies and parametric trades in subsequent chapters.

3.2 Functional Requirements

The principle engineering science objective of this project is to demonstrate the viability of strain actuation for aeroelastic control and to compare the effectiveness of strain actuation with conventional control surface actuation. Using these actuators, controllers shall be developed to demonstrate significant vibration suppression and bending/torsion flutter suppression.

The functional requirements for the test article which derive from the engineering science objective, can be separated into three categories, tunnel constraints, performance requirements, and safety and regulatory requirements, and are presented below.

Tunnel Constraints

When designing any aerodynamic experiment, compatibility with the tunnel selected for testing must be ensured. This flutter model will be flown in the Transonic Dynamics Tunnel (TDT) at the NASA Langley Research Center (LaRC). Although the wing is not intended to be tested at transonic speeds, this tunnel has been selected because of its accessibility and its adaptation to flutter testing. The test section of the tunnel is sixteen foot square. Air or freon may be used as the working fluid in the tunnel. The selection of the tunnel imposes the following constraints.

TC1. The model must be sized for the test section such that an infinite medium may be assumed.

TC2. The cantilevered wing model must be able to be mounted to either the wall or ground mounting devices.

TC3. All design airspeeds must be well within the tunnel operating envelope. [LWP-799]

TC4. For ease and safety, testing will be conducted using air as the working fluid.

Performance Requirements

Numerous models can be built that will satisfy the limitations of the tunnel, without actually accomplishing the stated project objective. To ensure that the objective is met, specific performance requirements must be established. Since this is a research project, these performance requirements can be interpreted as goals and further divided into three sections: physical model goals, field of view goals, and controller goals. Physical model goals define geometrical, mass, and power requirements of the model. Field of view goals have been set so that the unique advances of this project may be isolated and enumerated. Finally, the controller goals establish desired levels of control authority.

Physical Model Goals

The wing model must be representative of current and near future aircraft wings in which bending/torsion flutter is critical.

PR1. The geometry must be representative of such aircraft.

PR2. The actuation mass, authority, and power requirements must be realistic when scaled to full size.

PR3. Sensor location, quantity, type, and range must be realistic for such aircraft.

PR4. The model must be designed such that flutter will occur below static divergence and reversal.

PR5. The flutter mechanism should be a coalescence of the first two modes.

Field of View Goals

Since the technology of strain actuation is currently in its development stage, the following design goals have been established to focus resources on the advances of the planned demonstration phase.

PR6. The model shall be designed to flutter well below the transonic speed range, before compressibility becomes a significant factor.

PR7. To simplify the model characterization, only one model will be used for all testing: vibration suppression and flutter suppression.

PR8. To introduce structural thickness and the possibility of bend-twist coupling without introducing the complications of a monocoque wing structure, the internal structure shall be a sandwich spar construction.

PR9. To introduce representative aerodynamic thickness, a high performance, symmetrical airfoil shape shall be chosen for an aerodynamic shell to surround the internal structure.

PR10. The airfoil shape will provide zero lift at zero angle of attack.

PR11. The aerodynamic shell shall not add appreciable stiffness to the spar.

PR12. The flap stiffness will be high enough to assume chordwise rigidity.

Control Goals

Recalling that the principle objectives of this project are to prove the viability of strain actuation for aeroelastic control and to compare strain

actuation to conventional flap actuation, the following requirements are established.

PR13. Both the strain actuators and the conventional flap actuator will be pushed to their current technical limit.

PR14. The model will be designed to enable independent control of the first two modes by the strain actuation.

PR15. Developed controllers should improve performance by 20 dB in vibration suppression.

PR16. Developed flutter suppression controllers should show a marked increase in the flutter speed.

Safety and Regulatory Requirements

The three main categories here are safety issues, cost, and schedule.

SR1. A flutter stopper mechanism must be designed to ensure that a fluttering model can be brought to a stable aeroelastic condition before structural failure occurs.

SR2. The wing should be manufactured and mounted in such a manner that bench top vibration tests will not endanger equipment or operators and wind tunnel tests will not endanger the tunnel or its operators.

SR3. A stress analysis will be completed to ensure that maximum stresses lie within material specifications and to satisfy all applicable safety documents. [LHB 1710.15, May 1992]

SR4. Wing design, fabrication, and testing shall meet established budget constraints.

SR5. Wing design, fabrication, and testing shall meet established schedule constraints.

Because the remaining chapters summarize the scientific issues involved in the preliminary design process, several of the functional requirements will not be directly addressed. For example, PR3, PR11, and PR12 will be addressed during the detailed design process. Likewise, several of the control goals, PR15 and PR16, will be satisfied when the actual controllers are designed and implemented. Of the safety and regulatory requirements, only SR1, dealing with the design of a flutter stopper, will be addressed in this chapter.

3.3 Design Parameters

Design parameters are those dimensions, values, or shapes over which the designer has control. When these design parameters are properly chosen, the design will meet the functional requirements. The design parameters may be separated into three categories: geometrical, structural, and actuation. These parameters will be selected to satisfy the requirements and objectives outlined in Section 3.2.

Table 3.1 Design Parameters

Geometrical	Span
	Aspect ratio
	Geometrical sweep angle
	Airfoil shape
	Aerodynamic thickness ratio
	Aerodynamic taper ratio
Structural	Spar thickness ratio
	Spar taper ratio
	Laminate layup

	Fiber sweep angle
	Facesheet material
	Core material
Actuation	Flap chord ratio
	Flap span ratio
	Flap location
	Piezoceramic area coverage
	Piezoceramic thickness
	Piezoceramic sectioning

In addition to the design parameters listed above, a flutter stopper must be designed. Because the mechanism of the flutter stopper has yet to be determined, specific design parameters can not be listed. In Chapter 6, the design principle and mechanism of the flutter stopper will be determined and parametric trades will be completed on the appropriate design parameters.

There are two main methods of selecting values for these design parameters. The first of these methods is non-parametric study. For example, reference values for some parameters will be established based on previous experience, "common knowledge," and manufacturing contraints. These parameters include the span, the airfoil shape, and the materials. Another set of parameters will be determined by a survey of transport aircraft. The survey will set the aspect ratio and aerodynamic thickness and provide target values for the geometric sweep and taper ratios. The final non-parametric study is a scaling analysis comparing the current design to the earlier development phase test article. This scaling analysis will determine the piezoceramic thickness and the spar thickness ratio. All of the non-parametric studies will be presented in Chapter 4.

The remaining parameters will be determined by in-depth parametric trade studies. The first parametric study, discussed in Chapter 5, involves a trade between the fiber sweep angle and the geometric sweep angle. In conjunction with this study, the piezoceramic area coverage and sectioning and the flap parameters will be determined. The second parametric study, discussed in Chapter 6, determines the parameters for the tip mass flutter stopper. The final parametric study, discussed in Chapter 7, will examine the effect of varying taper ratios.

Chapter 4: Non-Parametric Studies

4.1 Introduction

This chapter marks the beginning of the design process, in which several of the design parameters will be determined. The first set of parameters will be established based on previous experience and "common knowledge." Others will be set through a survey of transport aircraft to satisfy the requirement for similarity to aircraft in which bending/torsion flutter is critical or PR1. The final study to be discussed in this chapter is a scaling analysis which will determine the piezoceramic thickness and the spar thickness ratio.

Values for the span, airfoil shape, materials, and laminate layup will first be chosen to satisfy certain of the functional requirements based on previous experience with the construction of laminated wings and model testing at the Transonic Dynamics Tunnel. A 48 inch half-span will be established as a reference, which fulfills the sizing requirement for the tunnel, or TC1, as well as manufacturing constraints on the largest laminate which can be cured at MIT. Following the guidelines of PR9 for representative aerodynamic thickness and PR10 for zero lift at zero angle of attack, the airfoil shape is baselined as a NACA 64-012 which is a high-performance, no camber airfoil. As used in this document, "reference" denotes values which are established but may be varied, re-examined, or altered before being fully established; "baselined" denotes the final choice of that parameter for the preliminary design. The baseline facesheet material will be graphite-epoxy (AS4/3501-6), a typical intermediate-modulus

aerospace material, and the baseline laminate layup is [θ / θ / 0]s, where θ is not zero. For θ = 0, the middle layers will be placed at an angle of 90 degrees in order to provide transverse strength. The baseline laminate incorporates bend-twist coupling to enable independent piezoelectric control of the first two modes as required by PR14. The core material will be an aluminum honeycomb to complete the sandwich construction required by PR8.

4.2 Survey of commercial aircraft

To choose values for several of the geometrical and aerodynamic parameters, a survey was completed of transport aircraft (Table 4.1). The survey included the 727, 737, 747, 757, 767, DC9, and DC10 (series 30,40). The aspect ratio is a full span aspect ratio and the thickness ratio (t/c) is an estimated average.

Table 4.1 Transport aircraft geometric parameters. 1/4 chord sweep angle is in degrees. (* indicates estimated value, all other values from Jane's All the World's Aircraft [1991])

	727	737	747	757	767	DC9	DC10
Aspect Ratio	7.07	8.83	---	---	7.9	8.71	7.5
1/4 chord sweep	32	25	37.5	25	31.5	24.5	35
Thickness ratio (avg)	11 %	13 %	10 %	---	13 %	11 %	10 %
Taper ratio	0.30	0.34	0.29 *	0.16 *	0.27	---	0.25

Using the table as a guideline, the wing model will have a reference full span aspect ratio of 8, or a half span aspect ratio of 4. The aerodynamic thickness ratio of the wing model will be baselined at 12%. The sweep angle values listed in the above table provide a reference geometric sweep angle of 30 degrees. However, the effect of sweep angle on the aeroelastic stability of the

wing needs to be investigated so that the aeroelastic requirements on the wing model may also be satisfied (PR4, PR5, PR6).

Similarly, the taper ratio values provide guidance for selecting a possible range of taper ratio down to 0.16. However, it should be noted that many of these aircraft have root chords significantly larger than would be obtained by a straight line extension of the outboard portion of the trailing edge. This added wing root chord, thickness, and corresponding area provides for increased fuel capacity, landing gear storage, and root thickness, but does not significantly affect the aeroelastic behavior of the wing. Therefore, for a straight trailing edge model, the taper ratio could be significantly greater than 0.16.

4.3 Scaling analysis

To extrapolate the strain actuation authority from the earlier development phase test article to the present design, and to determine an appropriate spar thickness ratio and piezoelectric thickness, a scaling analysis has been completed. One of the most important differences between the development phase experiments and the current investigation is the increase in the structural thickness of the test article and its effect on the piezoelectric authority. In this section, the governing authority parameter will be identified and scaled appropriately.

Using energy methods, the governing differential equation for an anisotropic plate-like lifting surface with piezoelectric layers is derived [Jones, 1975, Meirovitch, 1986, and Lazarus and Crawley, 1989].

$$-\rho h\frac{\partial^2 w}{\partial t^2}+D_{11}\frac{\partial^4 w}{\partial x^4}+2D_{12}\frac{\partial^4 w}{\partial x^2\partial y^2}+4D_{16}\frac{\partial^4 w}{\partial x^3\partial y}+D_{22}\frac{\partial^4 w}{\partial y^4}+4D_{26}\frac{\partial^4 w}{\partial x\,\partial y^3}+$$

$$4D_{66}\frac{\partial^4 w}{\partial x^2\partial y^2}+m_{\Lambda_{11}}\frac{\partial^2 \Lambda_x}{\partial x^2}+m_{\Lambda_{12}}\frac{\partial^2 \Lambda_y}{\partial x^2}+m_{\Lambda_{12}}\frac{\partial^2 \Lambda_x}{\partial y^2}+m_{\Lambda_{22}}\frac{\partial^2 \Lambda_y}{\partial y^2}=\text{Aero. Forces}$$

where: ρ is the plate area density
h is the plate thickness
w is the vertical displacement
D_{ij} is the bending stiffness
$m_{\Lambda_{ij}} = \int_{z_L}^{z_U} Q_{ij}^a z dz$
is the piezoelectric actuation moment
Q_{ij}^a is the modulus of the actuator layer
z_U, z_L are the heights of the upper and lower surfaces of each actuator layer
Λ is the actuation strain

(4.1)

For a box beam, $m_{\Lambda_o} = 2E_a z_m t_a$,
where E_a is the actuator modulus
z_m is the height of the actuator midline
t_a is the actuator thickness

(4.2)

The aerodynamic forces would include the typical lift and moment expressions. They have not been shown in Equation 4.1 for clarity.

Non-dimensionalizing the plate equation (Equation 4.1) will provide the appropriate scaling parameter. The dimensions will be non-dimensionalized in the following manner: the spanwise dimension x by the span L, the chordwise dimension y by the semichord b, the vertical displacement w by a reference displacement w_0, the time t by a reference frequency ω, all of the substrate stiffnesses D_{ij} by a reference stiffness D_0, all of the piezoelectric moment terms $m_{\Lambda ij}$ by a nominal reference $m_{\Lambda 0}$, and the piezoelectric strains Λ_x and Λ_y by a reference strain Λ_0. The resulting equation is

$$-\rho h w_o \omega^2 \frac{\partial^2 \overline{w}}{\partial \overline{t}^2} + \frac{D_o w_o}{L^4} \overline{D}_{11} \frac{\partial^4 \overline{w}}{\partial \overline{x}^4} + 2\frac{D_o w_o}{L^2 b^2} \overline{D}_{12} \frac{\partial^4 \overline{w}}{\partial \overline{x}^2 \partial \overline{y}^2} + 4\frac{D_o w_o}{L^3 b} \overline{D}_{16} \frac{\partial^4 \overline{w}}{\partial \overline{x}^3 \partial \overline{y}}$$
$$+ \frac{D_o w_o}{b^4} \overline{D}_{22} \frac{\partial^4 \overline{w}}{\partial \overline{y}^4} + 4\frac{D_o w_o}{L b^3} \overline{D}_{26} \frac{\partial^4 \overline{w}}{\partial \overline{x} \partial \overline{y}^3} + 4\frac{D_o w_o}{L^2 b^2} \overline{D}_{66} \frac{\partial^4 \overline{w}}{\partial \overline{x}^2 \partial \overline{y}^2} + \frac{m_{\Lambda_o} \Lambda_o}{L^2} \overline{m}_{\Lambda_{11}} \frac{\partial^2 \overline{\Lambda}_x}{\partial \overline{x}^2} \quad (4.3)$$
$$+ \frac{m_{\Lambda_o} \Lambda_o}{L^2} \overline{m}_{\Lambda_{12}} \frac{\partial^2 \overline{\Lambda}_y}{\partial \overline{x}^2} + \frac{m_{\Lambda_o} \Lambda_o}{b^2} \overline{m}_{\Lambda_{12}} \frac{\partial^2 \overline{\Lambda}_x}{\partial \overline{y}^2} + \frac{m_{\Lambda_o} \Lambda_o}{b^2} \overline{m}_{\Lambda_{22}} \frac{\partial^2 \overline{\Lambda}_y}{\partial \overline{y}^2} = \text{Aero. Forces}$$

To complete the non-dimensionalization, the governing plate equation of motion (Equation 4.3) is divided by the dimensional portion of the second term. The second term is used since the dynamics of a wing are referenced to its fundamental, usually a spanwise bending mode [Crawley and Dugundji, 1980].

Non-dimensional groups which emerge are the traditional non-dimensionalized frequency $\frac{\rho h L^4 \omega^2}{D_o}$ and the aspect ratio $\frac{L}{b}$. Had the aerodynamic forces been shown explicitly, the mass ratio and reduced velocity would have appeared as well. The newly identified non-dimensional parameter, which expresses the relative strain actuator authority, is

$$c_r = \frac{m_{\Lambda_o} L^2 \Lambda_o}{D_o w_o} \quad (4.4)$$

In order to make the non-dimensional group above useful in scaling, the length to be used for the reference vertical displacement, w_O, must be chosen. There are three possible choices: the span (L), the semichord (b), and the thickness (h). Table 4.2 shows the scaling parameter for each of the choices as well the simplified scaling parameter for a sandwich or box beam construction. The simplified parameter for sandwich construction assumes that the facesheets and piezoelectric actuators are all located at the same height (h/2) from the neutral axis.

It is apparent that the nature of the parameter changes with the dimension chosen for w_0. For beam-like problems, L might be the appropriate choice. For plate analysis of large deflections, h might be appropriate. But for aeroelastic problems in which the fundamental interest is in controlling the angle attack of the wing, the choice of b is the natural one, since it equates the non-dimensional parameter with the ability to induce a given twist in the wing.

Table 4.2 Scaling parameters for three choices of reference vertical displacement, w_0. E_s and t_s are properties of the substrate layers, E_a and t_a are properties of the actuator layer.

w_0	General Parameter	Box Beam Parameter
L	$\frac{m_{\Lambda_o} L^2 \Lambda_o}{D_o L}$	$2\left(\frac{L}{h}\right)\left(\frac{1}{1+\Psi}\right)\Lambda_o$
b	$\frac{m_{\Lambda_o} L^2 \Lambda_o}{D_o b}$	$2\left(\frac{L}{h}\right)\left(\frac{L}{b}\right)\left(\frac{1}{1+\Psi}\right)\Lambda_o$
h	$\frac{m_{\Lambda_o} L^2 \Lambda_o}{D_o h}$	$2\left(\frac{L}{h}\right)^2\left(\frac{1}{1+\Psi}\right)\Lambda_o$

$$\text{where } \Psi = \frac{E_s t_s}{E_a t_a}$$

Examining the piezoelectric authority parameter, the methods which can increase the piezoelectric authority are clear. In most problems the substrate modulus and the structural aspect ratio will be predetermined. Likewise, the modulus and actuation strain of the piezoelectrics is established by the current material technology. Therefore, the thickness of the actuator layer, t_a, and the slenderness ratio, $\frac{L}{h}$, are the two terms which can be altered to increase the piezoelectric authority.

Having determined the piezoelectric scaling law, the analysis logically proceeds to a comparison of the development and demonstration phase test articles. Two different cases will be examined: the first, a bending authority case, which utilizes the bending stiffness for the nominal stiffness, and the second, a torsional authority case, which utilizes the effective stiffness for bend-twist for the nominal stiffness (see Chapter 2).

$$\text{Bending Authority Effective Stiffness} \quad D_o = D_{11}$$
$$\text{Torsional Authority Effective Stiffness} \quad D_o = \frac{D_{11}D_{66} - D_{16}^2}{D_{16}} \tag{4.5}$$

These effective stiffnesses have also been derived using a three-mode static Rayleigh-Ritz analysis, which used extension, bending, and twist assumed shapes [Lazarus and Crawley, 1989]. The bending and torsion effective stiffnesses relate the bending and twist displacements to the piezoelectric bending moment, respectively. The torsional authority effective stiffness is not synonymous with the torsional stiffness, because the in-plane isotropic piezoelectric actuators can not provide shear strain. For the piezoelectric actuators to gain authority over torsional motion, they must take advantage of bend-twist coupling.

The most significant difference between the development phase test article and the current design is the spar thickness ratio. To incorporate representative structural thickness and satisfy PR8, the reference thickness ratio will be increased by a factor of 4 from 0.5 % in the development phase test article to 2 % in the current design. A 2 % thickness is chosen to introduce significant thickness without surpassing current strain actuation peformance. Because the half-span aspect ratio also increases from 2 to 4, the slenderness ratio ($\frac{L}{h}$) increases only from 0.25 % to 0.5 %. In addition, the current design is a sandwich spar construction with two six-ply plates

surrounding a layer of aluminum honeycomb as compared to the single six-ply plate of the development phase test article. The comparison of the different test articles can be seen in Table 4.3.

To examine the effect of increasing the piezoelectric thickness, which is the only remaining term in the relative strain authority parameter, the piezoelectric thickness will be varied from 0.010 in. to 0.020 in. to 0.040 in. The development phase experiment had a 0.010 in. piezoelectric thickness. To isolate the effect of the geometrical changes on the relative strain authority parameter, the laminate

Table 4.3 Geometrical comparison of development phase and demonstration phase test articles

	Development Phase	Demonstration Phase
Span	12 in.	48 in.
Aspect ratio (half-span)	2	4
Thickness ratio	0.5 %	2 %
Slenderness ratio	0.25 %	0.5 %

and material properties of the development phase test article are also assumed for the demonstration phase test article. The laminate of the development phase test article is [30/30/0]s and will be used for each facesheet of the demonstration phase test article. The material of the development phase test article was graphite epoxy AS1/3501-6 with a nominal ply thickness of 0.0053 in.

The bending authority comparison, seen in Table 4.4, shows that the demonstration phase test article will achieve authority equal to that of the development phase test article for sufficiently thick piezoelectrics. For t_a = 0.010 in., the bending authority for an equal amount of piezoelectric coverage

is less for the demonstration phase than for the development phase. This is understandable as the demonstration phase test article is a much stiffer structure having double the wing "skin" thickness and wing "skins" placed off of the neutral axis. However, increasing the piezoelectric thickness provides increasing strain authority and the loss can be regained. Notice that doubling the piezoelectric thickness from 10 mils to 20 mils nearly doubles the authority, while doubling the thickness from 20 mils to 40 mils does not. The cause of this diminishing return is that adding piezoelectrics adds incrementally more stiffness than authority, as can be seen from the $\frac{1}{1+\Psi}$ term in the Box Beam relative strain authority parameter of Table 4.2.

Table 4.4 Comparison of piezoelectric scaling parameters for development phase and demonstration phase test articles.

BENDING AUTHORITY		
Configuration	Parameter	% of Dev. Phase
Development Phase	824.8	
Demonstration Phase - 0.010 in.	361.3	43.8 %
0.020 in.	589.7	71.5 %
0.040 in.	823.0	100.6 %
TORSIONAL AUTHORITY		
Configuration	Parameter	% of Dev. Phase
Development Phase	317.6	
Demonstration Phase - 0.010 in.	371.6	117.0 %
0.020 in.	401.0	126.2 %
0.040 in.	312.9	98.5 %

The torsional authority case exhibits even more interesting behavior. For a piezoelectric thickness of 0.010 in., the demonstration phase test article has greater authority than the development phase. This is due to the increase in aspect ratio and an increase in the overall bend-twist coupling which arises due to the sandwich or box-beam construction. The bending stiffnesses of a laminated plate can be expressed as

$$D_{ij} = \sum_{k=1}^{N} \left(Q_{ij}\right)_k \left(t_k z_k^2 + \frac{t_k^3}{12} \right)$$

where $\left(Q_{ij}\right)_k$ is the modulus of the kth layer
t_k is the thickness of the kth layer
z_k is the height of the midline of the kth layer
N is the total number of layers (4.6)

The relative contribution of any given layer is weighted by the thickness of the layer and the square of its distance from the neutral axis. The thicknesses of the layers do not change from the development to the demonstration phase so the important variable is the distance from the neutral axis. In the development phase test article, the neutral axis is the midline of the plate. Therefore, the isotropic piezoelectric layers are relatively much further from the neutral axis than the anisotropic plate and their isotropy is heavily weighted. In contrast, the sandwich construction of the demonstration phase test article places all of the material at essentially the same displacement from the neutral axis. Due to this construction, the piezoelectric isotropy is less heavily weighted in the demonstration phase test article than in the development phase test article.

The other principle trend observed in Table 4.4 is that there exists an optimal thickness for torsional authority. Unlike the bending authority comparison, the 0.040 in. piezoelectric layer is less effective than the 0.020 in.

layer for torsional authority. This is due to the fact that increasing the piezoelectric thickness increases the weighting of the piezoelectric isotropy relative to the anisotropic laminates and the overall isotropy is increased. Increasing the overall isotropy reduces the bend-twist coupling. Since the piezoelectric actuators are isotropic and only have torsional authority through the bend-twist coupling, their torsional authority is reduced. Note that the appearance of this maximum is in contrast to the optimization for bending of a piezoelectrically actuated beam, which finds no optimum thickness for a fixed height, but does find an optimum height for a fixed thickness [Lazarus and Crawley, 1992a].

Having completed this scaling analysis, important insight has been obtained. Clearly, the demonstration phase test article must have a thicker piezoelectric coverage than the development phase experiments had. However, the torsional authority analysis indicates that for a 2 % thickness and the proposed laminate, 0.020 in. of coverage is optimum and recovers the authority of the development test article. Therefore, a piezoelectric thickness of 0.020 in. and a structural thickness of 2 % will be used as baselines for the remainder of the analysis.

The non-parametric studies are now concluded. The following list recapitulates the design parameter list and the reference and baseline values which have been established in this chapter.

Table 4.5 Summary of current reference and baseline values for design parameters. **Bold** indicates a baseline value.

Geometrical	Span (half)	48 in.
	Aspect ratio (full span)	8
	Geometric sweep angle	30 deg.
	Airfoil shape	**NACA 64-012**
	Aerodynamic thickness ratio	**12 %**
	Aerodynamic taper ratio	> 0.25
Structural	Spar thickness ratio	**2 %**
	Spar taper ratio	> 0.25
	Laminate layup	**[θ / θ / 0]s**
	Fiber sweep angle	---
	Facesheet material	**AS4/3501-6**
	Core material	**Aluminum honeycomb**
Actuation	Flap chord ratio	---
	Flap span ratio	---
	Flap location	---
	Piezoceramic area coverage	---
	Piezoceramic thickness	**0.020 in.**
	Piezoceramic sectioning	---

Chapter 5: Design Trade 1: Geometric vs. Fiber Sweep

5.1 Introduction

Geometric sweep and fiber sweep are two of the most influential parametric trades to be made in this design. Together, they affect the open loop stability and the authority of the strain and flap actuators. The two parameters must be examined simultaneously due to their interactive nature and baselined before the other parametric trades are conducted. The motivating requirements are that the wing model must flutter before it diverges [PR4] and the flutter speed must be within the tunnel operating envelope [TC3] and within the incompressible region [PR6]. Additionally, a coalescence of the first two modes has been specified as the desired flutter mechanism [PR5]. As discussed in Chapter 4, the geometric sweep should be representative of transport aircraft [PR1]. Enabling independent control of the first two modes by strain actuation is the main actuation requirement which affects the sweep trades [PR14]. This chapter will investigate the effects and interaction of these two parameters.

In order to examine these trades, a model will be developed using the Rayleigh-Ritz assumed modes method and two-dimensional strip theory aerodynamics. Following the model development, the model will be verified by comparison with experimental data for a rectangular plate specimen. Based on the trends for these plates, the trade space will be reduced to focus on regions with desirable aeroelastic characteristics. Then a model of a built up wing will be developed and analyzed using the same technique, examining

only the reduced trade space. The aeroelastic characteristics will be examined. The flap and piezoelectrics will be modelled and their baseline placement will be established. Finally, the effect of ply fiber angle and structural sweep on controllers utilizing these actuators will be investigated.

5.2 Model Development

This section describes the methods and equations used to model the aeroelastic behavior of the rectangular plates and the wing design. To begin, the structural model will be developed using the Rayleigh-Ritz method with five assumed shapes. The structural dynamics will be referenced to the wing fixed axes $(\bar{x},\bar{y})$ and will treat the wing as a rectangular plate even when swept (see Figure 5.1). Following the structural development, the aerodynamics will be added. The aerodynamics will use the full unsteady two dimensional strip theory with a one pole approximation of Theodorsen's function. The aerodynamic forces are naturally calculated in the wind axes (x,y) and will be transformed to the wing fixed axes $(\bar{x},\bar{y})$ to coincide with the structural dynamics. The sign convention and method of sweep can be seen in Figure 5.1.

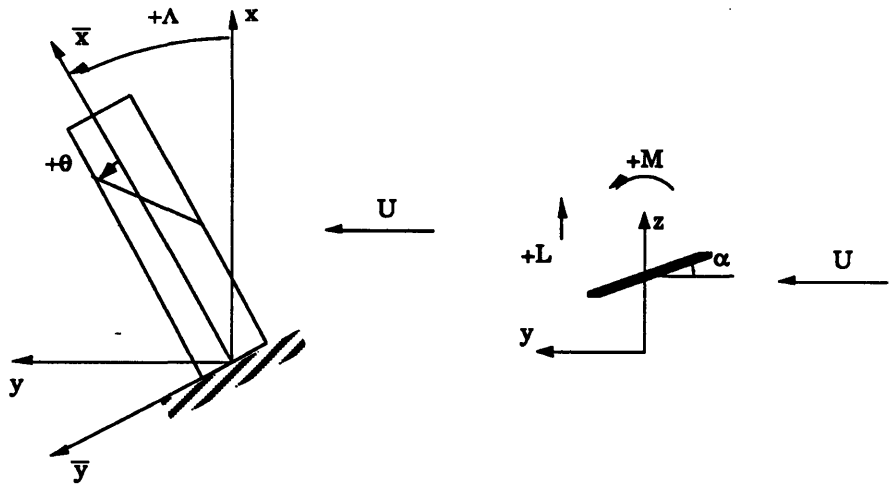

Figure 5.1 Sign convention for Rayleigh-Ritz and aerodynamic analysis.

Structural Dynamics

A Rayleigh-Ritz method is used to determine the natural frequencies and eigenvectors of the in vacuo structural plant [Meirovitch, 1986]. The displacements are assumed to have the following form.

$$\bar{w}(\bar{x},\bar{y},t) = \sum_{i=1}^{N} \bar{\gamma}_i(\bar{x},\bar{y}) q_i(t)$$

$$\text{where } \bar{\gamma}_i(\bar{x},\bar{y}) = \bar{\phi}_i(\bar{x})\bar{\psi}_i(\bar{y}) \qquad (5.1)$$

N = total number of assumed shapes

To obtain accurate natural frequencies using the Rayleigh-Ritz method, appropriate assumed Ritz shape functions (γ_i) are chosen with some prior knowledge of the structural dynamics of the plant. Five shapes are used: two beam bending shapes, two plate torsional shapes, and a chordwise bending shape (see Appendix C). The two beam bending shapes are the natural modes of a cantilevered beam [Blevins. 1984]. The chordwise bending shape is a free-free beam bending mode in the chordwise direction with a parabolic spanwise distribution. Jensen demonstrated the importance of including a chordwise bending shape for the accuracy of the first three modes when using bending-torsion stiffness coupled plates [Jensen, et al. 1982]. The plate torsional shapes are the torsional modes derived by a partial ritz method described in Crawley and Dugundji [1980] in the spanwise direction and are linear in the chordwise direction.

Using these assumed shape functions, the resulting equations of motion in the structural axes can be derived.

$$\mathbf{M}\ddot{\mathbf{q}}(t) + \mathbf{K}\mathbf{q}(t) = \mathbf{Q}(t) \qquad (5.2)$$

Unless the assumed shapes are the exact orthogonal modes of the test specimen, these equations will be fully coupled through the mass and stiffnes

matrices. The generalized forces (Q) will be defined below in terms of the aerodynamic forces. The homogeneous problem is evaluated to find the natural modes, **E**, which are mass normalized and transformed to modal form.

$$\mathbf{E}^T\mathbf{M}\mathbf{E}\ddot{\eta}(t)+\mathbf{E}^T\mathbf{K}\mathbf{E}\eta(t)=\mathbf{E}^T\mathbf{Q}\mathbf{E}\eta(t)$$
$$\text{where } \mathbf{q}=\mathbf{E}\eta,\ \mathbf{E}^T\mathbf{M}\mathbf{E}=\mathbf{I},\ \text{and } \mathbf{E}^T\mathbf{K}\mathbf{E}=\begin{bmatrix}\omega_1^2 & 0\\ 0 & \ddots\end{bmatrix} \tag{5.3}$$

The uncoupled modes of the test specimen, E, are found to be a linear combination of the assumed modes, γ.

Aerodynamics

Now that the structural dynamics have been defined, the aerodynamic forces due to the deflections of the wing will be incorporated into the model. In this section, expressions for the two dimensional strip theory generalized aerodynamic forces will first be derived in the wind axes. Following this derivation, the generalized aerodynamic forces will be transformed into the wing fixed axes for compatibility with the structural equation.

For incorporation into the modal equations of motion, the aerodynamic force on each generalized coordinate must be found. The generalized aerodynamic forces integrate the pressure distribution weighted by the different assumed shape functions.

$$Q_i=\iint \gamma_i(x,y)p(x,y)dydx \tag{5.4}$$

It is important to note that these are the generalized aerodynamic forces in the wind axes due to the pressure distribution expressed in the wind axes and weighted by the assumed shape functions referenced to the wind axes.

The assumed shape functions here are the assumed shape functions of Equation 5.1 transformed from the wing fixed axes to the wind axes. The details of this transformation will be discussed later in this section.

To avoid the complications of unsteady aerodynamics due to camber, the chordwise mode will not be included in the aerodynamics. Now that the camber mode has been removed, the remaining four assumed shapes may be represented in the wind axes by the deflection of the wing centerline and the twist angle about that centerline.

$$\gamma_i(x,y) = \gamma_{o_i}(x) - (y - y_c)\alpha_{o_i}(x)$$
$$\text{where } y_c \text{ is the } y \text{ location of the wing centerline} \tag{5.5}$$

Again, these are the assumed shapes referenced to the wind axes and their relation to the assumed shapes referenced to the wing fixed axes will be shown later in this section.

The familiar aerodynamic lift and moment can be derived as portions of the generalized aerodynamic forces when the new representation of the assumed shapes in the wind axes (Equation 5.5) is substituted into the generalized aerodynamic force expression (Equation 5.4).

$$Q_i = \int \gamma_{o_i}(x) L dx + \int \alpha_{o_i}(x) M_c dx$$
$$\text{where } L = \int p(x,y) dy \tag{5.6}$$
$$M_c = \int -(y - y_c) p(x,y) dy$$

The lift, L, is a concentrated force in the wind axes acting at the centerline of the wing and the moment, M_C, is a concentrated moment in the wind axes about the x axis evaluated at the centerline of the wing.

To develop expressions for sectional lift and moment, 2D strip theory aerodynamics will be used. Like the typical section analysis, a one-pole

rational approximation for Theodorsen's function is used. In contrast to the typical section analysis, the approximation will not be matched for one reduced frequency, but will be a best fit over a reduced frequency range of 0 to 1. The resulting approximation is

$$C(\bar{p}) = \frac{0.55\bar{p} + 0.15}{\bar{p} + 0.15} \tag{5.7}$$

The full unsteady lift and moment expressions for 2D strip theory have damping and apparent mass terms as well as the lag terms and the steady aerodynamic terms.

$$L = \sum_{j=1}^{N} \frac{\rho U^2}{2} b \left\{ \begin{array}{l} \left[B_{2A}\bar{p}^2 + B_{1A}\bar{p} + B_{0A} + \dfrac{B_{3A}\bar{p}}{\bar{p}+0.15} \right] \dfrac{\gamma_{o_j}}{b} + \\ \left[B_{2B}\bar{p}^2 + B_{1B}\bar{p} + B_{0B} + \dfrac{B_{3B}\bar{p}}{\bar{p}+0.15} \right] \alpha_{o_j} \end{array} \right\} \cos\Lambda$$

$$M_c = \sum_{j=1}^{N} \frac{\rho U^2}{2} b^2 \left\{ \begin{array}{l} \left[B_{2C}\bar{p}^2 + B_{1C}\bar{p} + B_{0C} + \dfrac{B_{3C}\bar{p}}{\bar{p}+0.15} \right] \dfrac{\gamma_{o_j}}{b} + \\ \left[B_{2D}\bar{p}^2 + B_{1D}\bar{p} + B_{0D} + \dfrac{B_{3D}\bar{p}}{\bar{p}+0.15} \right] \alpha_{o_j} \end{array} \right\} \cos\Lambda \tag{5.8}$$

where $\bar{p} = \dfrac{\lambda b}{U}$

N = total number of assumed shapes
(4 for aerodynamics)

Each of the four remaining assumed shapes contributes to the lift and moment and the summation of their individual contributions is the total lift and moment. The cos Λ in both terms is a correction on the lift curve slope for geometrical sweep. The values of the coefficients (B's) are listed in Appendix C. The two dimensional strip theory expressions for lift and moment (Equations 5.8) are then substituted into the generalized aerodynamic forces (Equation 5.6) and rearranged.

$$Q_i = \frac{1}{2}\rho U^2 \sum_{j=1}^{N}\left[\overline{p}^2 A_{2_{ij}} + \overline{p}A_{1_{ij}} + A_{0_{ij}} + \frac{\overline{p}}{\overline{p}+0.15}A_{3_{ij}}\right]q_j \tag{5.9}$$

where

$$A_{2_{ij}} = \int_0^l \begin{bmatrix}\gamma_{o_i} & \alpha_{o_i}\end{bmatrix}\begin{bmatrix}B_{2A}\cos\Lambda & bB_{2B}\cos\Lambda \\ bB_{2C}\cos\Lambda & b^2 B_{2D}\cos\Lambda\end{bmatrix}\begin{Bmatrix}\gamma_{o_j} \\ \alpha_{o_j}\end{Bmatrix} dx$$

similar for $A_{1_{ij}}$, $A_{0_{ij}}$, and $A_{3_{ij}}$

Now the generalized aerodynamic forces have been expressed in terms of the wing centerline displacement and twist angle of the assumed shapes in the wind axes.

For simplification, vector/matrix manipulation will be used in place of the integration of the generalized aerodynamic force components over the wing (Equation 5.9). The wing will be evenly divided into ten spanwise sections and the distributed aerodynamic forces will be modelled as concentrated forces acting at the center of these sections; therefore, the assumed shapes will only need to be evaluated at these points. To obtain the concentrated force, the magnitude of the distributed force on a given section must be multiplied by the spanwise length of the section (Δx). Now the integration of the generalized aerodynamic force components in Equation 5.9 may be approximated by a series of matrix multiplications.

$$A_{2_{ij}} = \left[\gamma_{o_{i_1}} \quad \cdots \quad \gamma_{o_{i_{10}}} \quad \alpha_{o_{i_1}} \quad \cdots \quad \alpha_{o_{i_{10}}} \right] \left[\begin{array}{ccc|ccc} B_{2A}\Delta x\cos\Lambda & & 0 & bB_{2B}\Delta x\cos\Lambda & & 0 \\ & \ddots & & & \ddots & \\ 0 & & B_{2A}\Delta x\cos\Lambda & 0 & & bB_{2B}\Delta x\cos\Lambda \\ \hline bB_{2C}\Delta x\cos\Lambda & & 0 & b^2B_{2D}\Delta x\cos\Lambda & & 0 \\ & \ddots & & & \ddots & \\ 0 & & bB_{2C}\Delta x\cos\Lambda & 0 & & b^2B_{2D}\Delta x\cos\Lambda \end{array} \right] \left\{ \begin{array}{c} \gamma_{o_{j_1}} \\ \vdots \\ \gamma_{o_{j_{10}}} \\ \alpha_{o_{j_1}} \\ \vdots \\ \alpha_{o_{j_{10}}} \end{array} \right\}$$

similar for $A_{1_{ij}}$, $A_{0_{ij}}$, and $A_{3_{ij}}$

where $\gamma_{o_{i_n}}$ = centerline displacement of the ith assumed shape evaluated at the midpoint of strip n

$\alpha_{o_{i_n}}$ = centerline twist angle of the ith assumed shape evaluated at the midpoint of strip n

Δx = spanwise length of each strip

(5.10)

Equation 5.10 assumes that the strips are all of equal semichord (b) and spanwise length (Δx). It is important to note that all quantities in Equation 5.10 are referenced to the wind axes.

Since the structural equation is referenced to the wing fixed axes ($\bar{x}, \bar{y}$), the generalized aerodynamic forces (Equations 5.9 and 5.10) must also be placed in terms of these axes. The inclusion of sweep introduces an aerodynamic bend-twist coupling. The angle of attack in the wind axes is a combination of the twist angle in the wing fixed axes and the spanwise slope in the wing fixed axes. The wing centerline displacement and twist angle in the wind axes may be expressed in terms of the wing centerline displacement and twist angle in the wing fixed axes.

$$\gamma_{o_i} = \bar{\gamma}_{o_i}$$

$$\alpha_{o_i} = -(\sin\Lambda)\frac{\partial\bar{\gamma}_{o_i}}{\partial\bar{x}} + (\cos\Lambda)\bar{\alpha}_{o_i}$$

$$\text{where } \alpha_{o_i} = -\frac{\partial\gamma_{o_i}}{\partial y} \text{ and } \bar{\alpha}_{o_i} = \frac{\partial\bar{\gamma}_{o_i}}{\partial\bar{y}} \tag{5.11}$$

bars indicate quantities referenced to the wing fixed axes

other quantities are referenced to the wind axes

The sweep affects only the local angle of attack, with the vertical displacement remaining the same in both axes. To transform the generalized aerodynamic forces (Equations 5.9 and 5.10) into the wing fixed axes, Equations 5.11 must be substituted for all of the wind axes assumed shape functions in Equations 5.9 and 5.10. These substitutions into Equation 5.9 duplicate the aerodynamic transformation in Section 2.4 if the two simple modes are used.

Finally, the generalized aerodynamic forces, which are fully transformed into the wing fixed axes, are mass normalized and incorporated into the mass normalized modal equations of motion.

$$\ddot{\eta}(t) + \mathbf{E}^T\mathbf{K}\mathbf{E}\eta(t) = \frac{1}{2}\rho U^2\left(\frac{b}{U}\right)^2\mathbf{E}^T\mathbf{A}_2\mathbf{E}\ddot{\eta}(t) + \frac{1}{2}\rho U^2\left(\frac{b}{U}\right)\mathbf{E}^T\mathbf{A}_1\mathbf{E}\dot{\eta}(t) + \frac{1}{2}\rho U^2\mathbf{E}^T\mathbf{A}_0\mathbf{E}\eta(t) + \frac{1}{2}\rho U^2\mathbf{E}^T\mathbf{A}_3\mathbf{E}\hat{\mathbf{y}}(t) \tag{5.12}$$

$$\dot{\hat{\mathbf{y}}}(t) + 0.15\frac{U}{b}\hat{\mathbf{y}}(t) = \dot{\eta}(t)$$

The second equation represents the dynamics of the first order lag states introduced by the approximation of Theodorsen's function. The vector $\hat{\mathbf{y}}$ has one additional lag state for every mode. The aerodynamic forces have now been transformed into the structural coordinates and the time domain so that they appear to act as modal forces on the natural, uncoupled modes. It is

important to recall that the semichord, b, and the section length, Δx, are referenced to the wind axes and can be transformed to the wing fixed axes semichord, $\bar{b}$, and section length, $\Delta\bar{x}$.

$$b = \frac{\bar{b}}{\cos\Lambda} \quad \text{and} \quad \Delta x = \Delta\bar{x}\cos\Lambda \tag{5.13}$$

For the stability analysis, these equations are manipulated into the state space form.

$$\begin{Bmatrix} \dot{\eta} \\ \ddot{\eta} \\ \dot{\hat{y}} \end{Bmatrix} = \begin{bmatrix} \mathbf{0} & \mathbf{I} & \mathbf{0} \\ -\mathbf{M}^{*-1}\mathbf{K}^{*} & -\mathbf{M}^{*-1}\mathbf{B}^{*} & -\mathbf{M}^{*-1}\mathbf{G}^{*} \\ \mathbf{0} & \Gamma & -0.15\frac{U}{b}\mathbf{I} \end{bmatrix} \begin{Bmatrix} \eta \\ \dot{\eta} \\ \hat{y} \end{Bmatrix} \tag{5.14}$$

$$\text{where } \mathbf{M}^{*} = \mathbf{I} - \frac{1}{2}\rho U^2\left(\frac{b}{U}\right)^2 \mathbf{E}^{T}\mathbf{A}_2\mathbf{E}$$

$$\mathbf{K}^{*} = \mathbf{E}^{T}\mathbf{K}\mathbf{E} - \frac{1}{2}\rho U^2\mathbf{E}^{T}\mathbf{A}_0\mathbf{E}$$

$$\mathbf{B}^{*} = -\frac{1}{2}\rho U^2\left(\frac{b}{U}\right)\mathbf{E}^{T}\mathbf{A}_1\mathbf{E}$$

$$\mathbf{G}^{*} = -\frac{1}{2}\rho U^2\mathbf{E}^{T}\mathbf{A}_3\mathbf{E}$$

$$b = \frac{\bar{b}}{\cos\Lambda}$$

Equation 5.14 represents the final 12 state homogenous aeroelastic model used for the stability analysis in this and subsequent chapters. Five assumed shapes, two spanwise bending, two torsional, and one chordwise bending, have been used in a Rayleigh-Ritz analysis to find the first five natural modes. The highest, predominantly chordwise mode, has been truncated and the aerodynamic forces acting on the remaining modes have been fit with a first order lag, yielding a model with eight structural modes and four aerodynamic lags.

5.3 Application to simple rectangular plates

Before modelling and analyzing the actual built-up wing design, the aeroelastic stability of simple rectangular plates will be examined. The purpose is twofold. First, the aeroelastic stability of plates such as these have already been predicted and experimentally confirmed by Landsberger and Dugundji [1985] and will serve as a verification of the model. Second, the plate analysis will be used to select portions of the overall trade space on which to focus in subsequent analyses.

A wide trade space will be examined for this initial study. The aspect ratio of these plates is the same as the reference aspect ratio of the wing model. The physical dimensions are 3" by 12". The trade space includes the ply fiber angles of -45, -30, -15, 0, 15, 30, and 45 degrees and the structural sweep angles of -30, -15, 0, 15, and 30 degrees. Like the wing model, the baseline layup is [θ / θ / 0]s except for a ply fiber angle of zero degrees. When the ply fiber angle is zero degrees, the middle layers will be placed at 90 degrees to maintain some chordwise stiffness. The material is graphite epoxy, AS1/3501-6, and the elastic moduli are the "flexural" moduli taken from Landsberger and Dugundji [1985](Appendix B).

Using the Rayleigh-Ritz approach described earlier, the natural modes for the different ply fiber angles can be found (Table 5.1). Frequencies for the negative ply fiber angles are the same as for their positive counterparts. The natural modes are exactly the assumed shape functions for the $[0_2/90]$s laminate. For all other laminates the natural modes are linear combinations of the assumed shapes. Labelling a mode first bending indicates that the first assumed shape (first beam bending) dominates that mode. The classification of the second natural mode as first torsion or second bending is more problematic [Jensen, et al., 1982]. For zero ply fiber angle, the second mode

is clearly first torsion. As the ply fiber angle increases, the contribution of second bending to this mode increases until the second natural mode more closely resembles second bending than first torsion for a ply fiber angle of 45 degrees.

Table 5.1 Calculated natural frequencies for first three modes of 3" by 12" plates. (Hz)

Mode	[0/0/90]s	[15/15/0]s	[30/30/0]s	[45/45/0]s
1B	11.1	9.0	6.4	5.0
2B	69.3	65.3	41.1	33.0
1T	39.6	44.1	63.8	60.9

Adding the aerodynamics, the stability characteristics can be examined. Using a velocity iteration and finding the eigenvalues of the state space system, the speed at which the first instability occurs is found. Figure 5.2 shows the trends for ply fiber angle and structural sweep. For clarity, only structural sweep angles of -30, 0, and 30 degrees have been shown. This figure matches Landsberger's predicted stability speeds precisely and shows good correlation with the experimental data of Figure 7 in Landsberger and Dugundji [1985].

The flutter and divergence boundaries in Figure 5.2 are defined by the interaction of the geometric sweep and the fiber sweep. Forward geometric sweep (Λ negative) and aft fiber sweep (θ positive) both create a "wash-in" effect, in which the wing twists to increase the angle of attack as the wing deflects upward. "Wash-in" wings are, therefore, more susceptible to divergence. Conversely, aft geometric sweep (Λ positive) and forward fiber sweep (θ negative) create a "wash-out" effect, in which the wing twists to

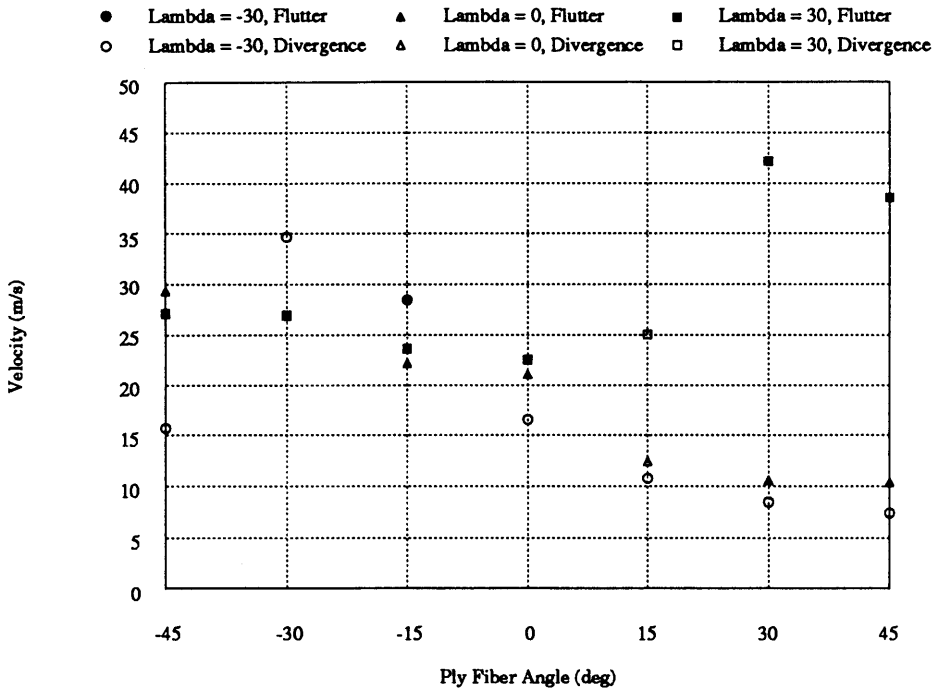

Figure 5.2 Calculated flutter and divergence speeds for the ply fiber angle vs. structural sweep angle trade . 3" by 12" plates.

decrease the angle of attack as the wing deflects upward. "Wash-out" wings have significantly higher divergence speeds than "wash-in" wings and normally flutter first. When simultaneously varying the geometric sweep and the fiber sweep, the nature of the first instability will depend on the relative strength of the different sweep-induced effects.

Combining forward geometric sweep (Λ negative) and aft fiber sweep (θ positive) produces wings which consistently diverge first. The divergence speeds are also robust to small changes in either geometric or fiber sweep. In this case, the "wash-in" effect caused by the aft fiber sweep is augmented by a similar effect due to the forward geometric sweep. When the geometric sweep is zero, the aft fiber sweep "wash-in" effect still dominates and these wings also diverge first.

Similarly, aft geometric sweep (Λ positive) augments the "wash-out" effects of forward fiber sweep (θ negative). All of the wings in this portion of the trade space flutter first. In addition, the flutter speeds are robust to small changes in either geometric or fiber sweep. When the geometric sweep is zero, the forward fiber sweep "wash-out"effect dominates and these wings also flutter first.

When the two sweep effects oppose each other, the nature of the first instability and the speed at which it occurs vary for small changes in geometric or fiber sweep. The "wash-in" due to forward geometric sweep (Λ negative) counteracts the "wash-out" due to forward fiber sweep (θ negative) and the stability boundary for these sweeps is composed of a flutter boundary and a divergence boundary. The same is true when aft geometric sweep is used with aft fiber sweep.

Based on these trends, a portion of the trade space may be chosen for further examination. The wing is required to flutter before it diverges [PR4]. In addition, it is desirable to have a region in which the nature of the first instability and its speed are robust to small changes in geometric and fiber sweep. This reduces the trade space to non-forward geometric sweeps (Λ positive or zero) and non-aft fiber sweeps (θ negative or zero), the only region in which flutter is consistently the first instability and in which the flutter speeds are robust to small variations in geometric or fiber sweep. The numerical values of the flutter and divergence speeds and flutter frequencies can be seen in Appendix C. Figure 5.3 shows a representative pole locus of one design case in the remaining trade space. The case has a fiber sweep angle of -15 degrees and a geometric sweep angle of 30 degrees and demonstrates a classical first-second mode coalescence flutter. The poles on

the real axis are the lag states and do not become complex until after flutter has occurred.

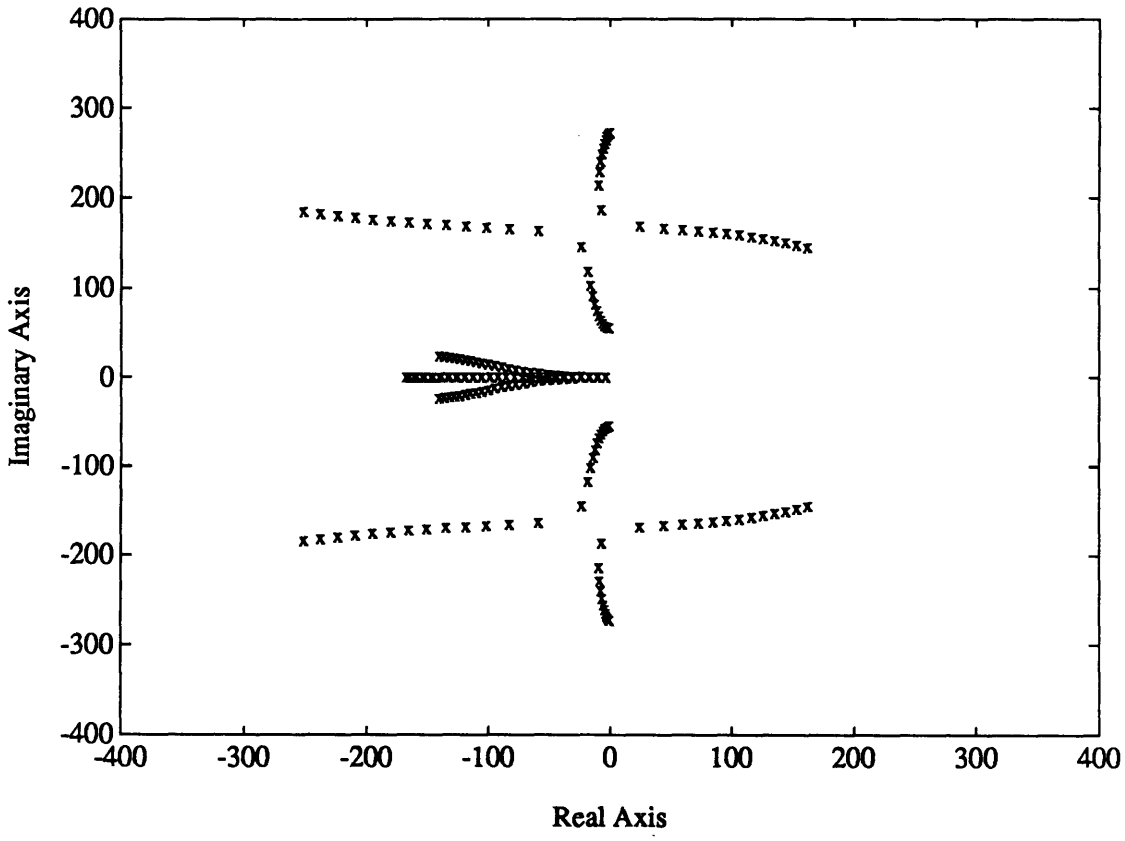

Figure 5.3 Pole locus for a ply fiber angle of -15 degrees and a structural sweep angle of 30 degrees. U = 0 to 50 m/s.

5.4 Application to Wing Model: Aeroelastic Behavior

Now that the aeroelastic model has been verified and a design subspace identified, a more complete wing model will be analyzed. First a model of the wing will be created which will include actuators, flutter stopper mass, and other masses as appropriate. Following the model development, the aeroelastic stability characteristics will be studied and the trends

compared to those of the simpler rectangular plates for the reduced trade space.

Figure 5.4 shows the simplified model developed of the built-up wing. The structural box has a span of 48 in. and a chord of 12 in. The baseline structural thickness ratio of 2% gives a box thickness of 0.24 in. The same six-ply layups $[\theta_2/0]s$ will be used for each facesheet for a total of 12 plies, but the graphite epoxy used will be AS4/3501-6 (Appendix B). An aluminum honeycomb serves as the core between the two facesheets and will be modelled as an isotropic material with an elastic modulus two orders of magnitude smaller than the longitudinal modulus of the graphite epoxy.

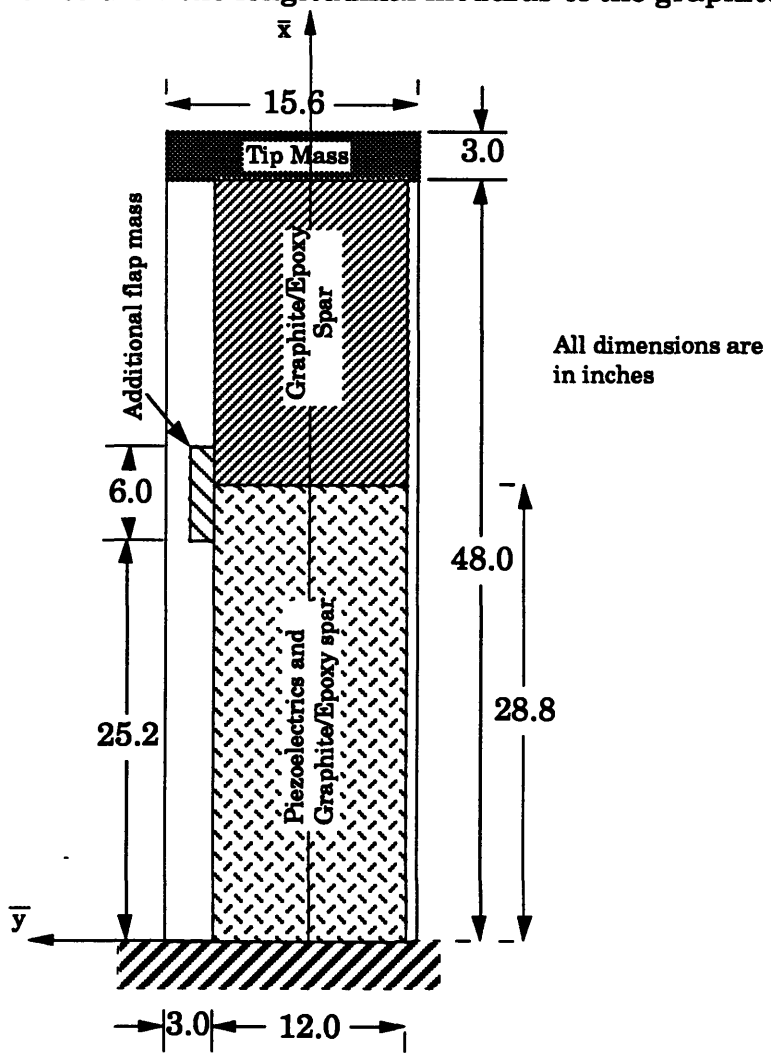

Figure 5.4 Schematic of wing model used in analysis

In addition to the changes in the structural core, there are several new features. A fiberglass aerodynamic shell has been modelled. It covers a span of 48 in. and a chord of 15.6 in. The symmetric airfoil chosen is a NACA 64-012. In this analysis the skin will be modelled with mass only. Aerodynamically, the wing will be considered to be a flat plate. A 20 mil layer of piezoelectrics has also been added to the outside of each facesheet. The piezoelectrics cover the entire chord of the structural box, but only 60 % of the structural box span, or 28.8 in, and have been modelled with stiffness and mass. An extra mass section has been added to represent the additional mass of flap bearings and supports. This section has been indicated in Figure 5.5 and has been modelled with an evenly distributed weight of 0.5 lbs. A tip mass has been added to provide for the tip mass flutter stopper to be discussed in Chapter 6. It has the same aerodynamic chord as the wing and adds an extra 3 in. to the span. For the current purposes it will be modelled as an evenly distributed 2.2 lb weight. The properties for materials used in the model are listed in Appendix C.

The natural modes are calculated using the Rayleigh-Ritz procedure of Section 5.2 and are listed in Table 5.2.

Table 5.2 Natural frequencies for first three modes of wing model. (Hz)

Mode	[0/0/90]s	[15/15/0]s	[30/30/0]s	[45/45/0]s
1B	3.3	3.5	3.2	3.0
2B	18.8	20.3	16.9	16.5
1T	14.4	15.9	19.8	19.2

Because of the mass nonuniformity and fiber sweep, all of the modes are linear combinations of the assumed Ritz shapes. In particular, the second

and third modes for all of the ply fiber angles except for zero degrees are highly coupled versions of first torsion and second bending.

Incorporating the aerodynamics, aeroelastic trends similar to those for the simpler rectangular plates appear and are shown in Figure 5.5. Ignoring the numerical values for flutter speed, this plot replicates the left half of Figure 5.2 for aft and zero geometric sweep angles. As was found for the simple rectangular plates, the nature of the first instability and its speed are robust to changes in geometric and fiber sweep for this subspace; therefore, a geometric sweep angle and a fiber sweep angle may be chosen within this subspace to satisfy other requirements.

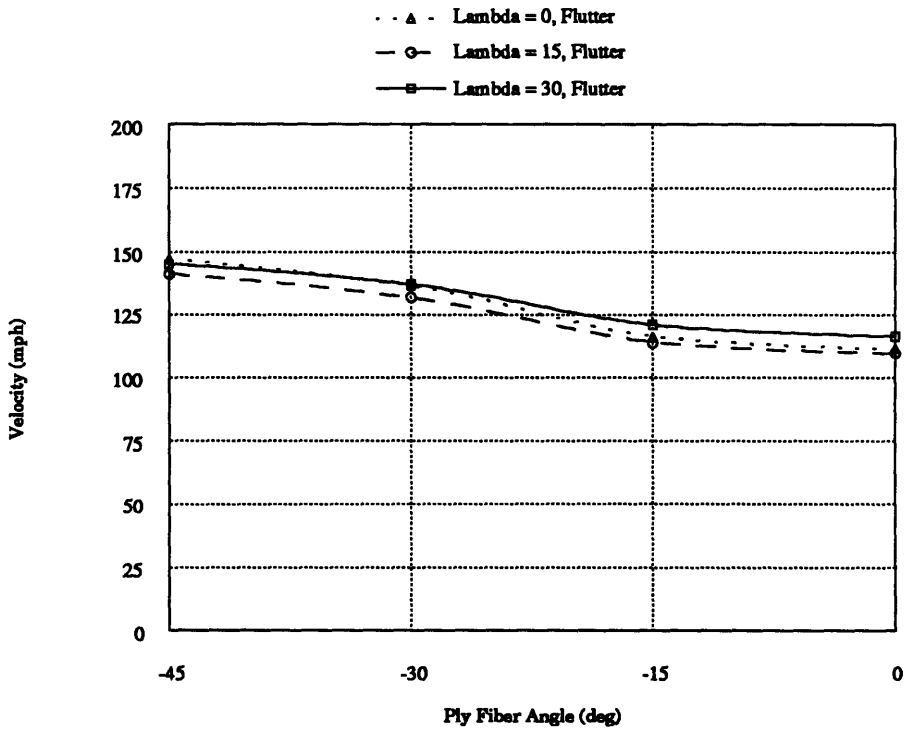

Figure 5.5 Flutter and divergence speeds for the ply fiber angle vs. structural sweep angle trade. Wing model.

A further requirement is that the flutter mechanism will be a first mode/second mode coalescence [PR5]. The root loci can be examined to verify this requirement. For a given fiber sweep angle, the root loci and, therefore,

the flutter mechanism do not change appreciably for a change in geometric sweep angle within the design subspace. Therefore, only the root loci for a geometric sweep angle of 30 degrees will be shown. Figure 5.6 shows that the flutter mechanism for a fiber sweep angle of -45 degrees is a complex three mode mechanism. Figure 5.7 shows that the flutter mechanism for a fiber sweep angle of -15 degrees is a coalescence of the first two modes. This pattern is representative of fiber sweep angles of 0 and -30 degrees. Based on these root loci, the -45 degree fiber sweep angle will be eliminated from further consideration and the remaining trade space contains fiber sweep angles of 0, -15, and -30 degrees and geometric sweep angles of 0, 15, and 30 degrees. Since all of these cases have shown desirable stability characteristics, their effect on actuator authority may be considered before making the final choice.

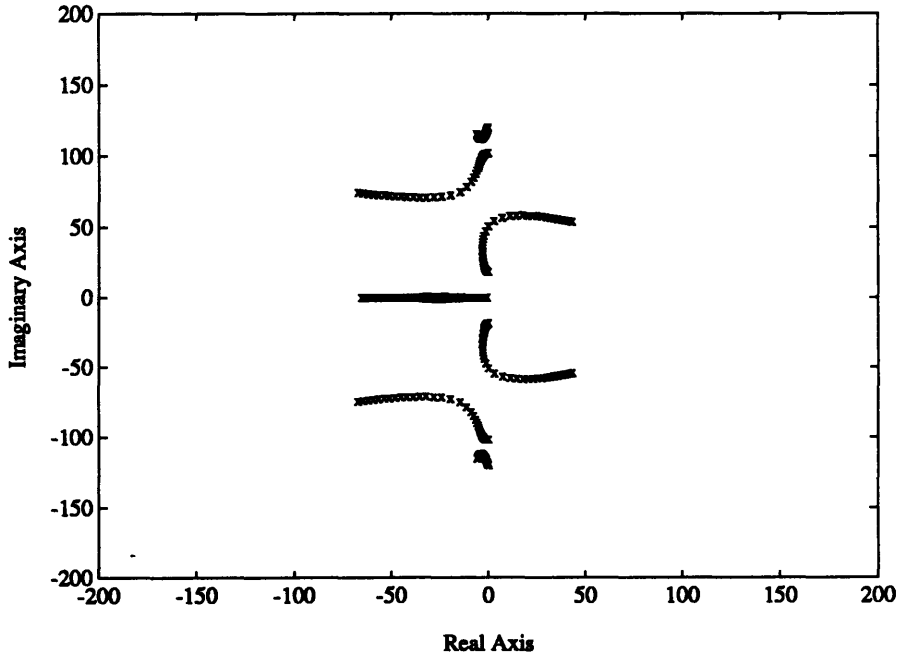

Figure 5.6 Pole locus for a ply fiber angle of -45 degrees and a structural sweep angle of 30 degrees. U = 0 to 100 m/s.

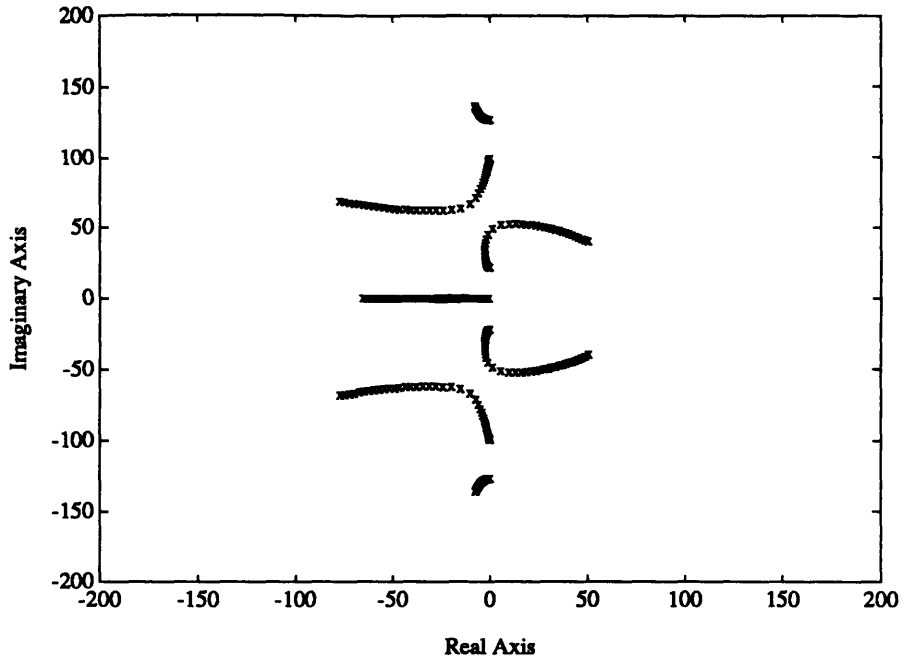

Figure 5.7 Pole locus for a ply fiber angle of -15 degrees and structural sweep angle of 30 degrees. U = 0 to 100 m/s.

5.5 Application to Wing Model: Actuation Issues

In this section, the effect of the ply fiber angle and structural sweep angle on the actuation authority of the wing model will be studied. One of the primary reasons for designing the composite laminate is to create bend-twist coupling to enhance the piezoelectric authority on the torsional mode. This must be done without reducing the authority of the trailing edge flap. In order to prevent this, the laminate must be designed such that the torsional node line does not cross the trailing edge near the flap, thereby reducing its effectiveness.

In the analysis below, the trailing edge flap will be modelled and a reference placement chosen. Then the piezoelectric actuation will be modelled and a reference grouping or placement of actuator groups will be established. Finally, some preliminary controllers will be designed using the

Linear Quadratic Regulator method to examine the effect of fiber sweep angle and geometric sweep angle on the actuation authority.

Trailing edge flap modelling and placement

To model the generalized forces due to the flap, its sectional aerodynamic forces must be calculated. The influence of the flap will be included in the aerodynamics, but the flap dynamics will not be considered as an additional mode in the Rayleigh-Ritz analysis. To implement the flap forces in the same manner as the aerodynamic forces in Section 5.2, the flap forces must be placed into the form shown.

$$\begin{aligned} L &= \frac{1}{2}\rho U^2 b\left[B_{2E}\bar{p}^2 + B_{1E}\bar{p} + B_{0E} + \frac{B_{3E}\bar{p}}{\bar{p}+0.15}\right]\beta\cos\Lambda \\ M &= \frac{1}{2}\rho U^2 b^2\left[B_{2F}\bar{p}^2 + B_{1F}\bar{p} + B_{0F} + \frac{B_{3F}\bar{p}}{\bar{p}+0.15}\right]\beta\cos\Lambda \end{aligned} \tag{5.15}$$

Taking the original equations for lift and moment from Theodorsen [1935] and extracting the contribution from a trailing edge flap, the following expressions are obtained.

$$\begin{aligned} L &= \rho b^2\left(-UT_4\dot{\beta} - T_1 b\ddot{\beta}\right) + 2\pi\rho UbC(k)\left\{\frac{1}{\pi}T_{10}U\beta + b\frac{1}{2\pi}T_{11}\dot{\beta}\right\} \\ M &= -\rho b^2\left[(T_4+T_{10})U^2\beta + \left(T_1 - T_8 - cT_4 + \frac{1}{2}T_{11}\right)Ub\dot{\beta} - (T_7 + cT_1)b^2\ddot{\beta}\right] \\ &\quad + \rho Ub^2\pi C(k)\left\{\frac{1}{\pi}T_{10}U\beta + b\frac{1}{2\pi}T_{11}\dot{\beta}\right\} \end{aligned} \tag{5.16}$$

Using the appreximation of Theodorsen's function and the Laplace variable from Section 5.2 , the lift and moment can be placed into the form of Equations 5.15 with the coefficients B.

$$
\begin{aligned}
B_{2E} &= -2T_1 \\
B_{1E} &= -2T_4 + 1.1T_{11} \\
B_{0E} &= 4T_{10} \\
B_{3E} &= -1.8T_{10} + 0.135T_{11} \\
B_{2F} &= 2T_7 + 2c_f T_1 \\
B_{1F} &= -2T_1 + 2T_8 + 2c_f T_4 - 0.45T_{11} \\
B_{0F} &= -2T_4 \\
B_{3F} &= -0.9T_{10} + 0.0675T_{11}
\end{aligned}
\tag{5.17}
$$

The distance from the midchord to the flap hinge line normalized by the semichord is represented in Equations 5.17 as c_f. The expressions for T_i's are in Appendix A and are the same as for the typical section.

Now the generalized aerodynamic forces due to the flap may be derived. The additional lift and moment due to the flap from Equations 5.15 are substituted into the generalized aerodynamic force equation (Equation 5.6).

$$
Q_i = \frac{1}{2}\rho U^2 \left\{ \begin{aligned} &\int_{l_1}^{l_2} b\gamma_{o_i}\left[B_{2E}\overline{p}^2 + B_{1E}\overline{p} + B_{0E} + \frac{B_{3E}\overline{p}}{\overline{p}+0.15}\right]\beta dx \\ &+\int_{l_1}^{l_2} b^2\alpha_{o_i}\left[B_{2F}\overline{p}^2 + B_{1F}\overline{p} + B_{0F} + \frac{B_{3F}\overline{p}}{\overline{p}+0.15}\right]\beta dx \end{aligned} \right\} \cos\Lambda \tag{5.18}
$$

In contrast to aerodynamic forces of Section 5.2, the integration limits are established by the spanwise location and size of the flap(see Figure 5.8).

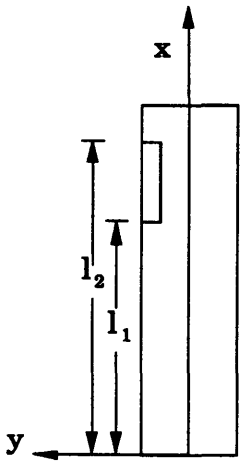

Figure 5.8 Inclusion of flap in wing model

For computational ease, the wing is divided into ten spanwise sections as in Section 5.2 and concentrated forces are calculated for each section. A vector multiplication weights each force by the modal displacement at the center of the section. The summation of the weighted forces is the total modal force. The modal force is returned to the time domain for incorporation into the equations of motion.

$$Q_i = \frac{1}{2}\rho U^2 \left[A_{2\bar{\beta}_i}\left(\frac{b}{U}\right)^2 \ddot{\bar{\beta}} + A_{1\bar{\beta}}\left(\frac{b}{U}\right)\dot{\bar{\beta}} + A_{0\bar{\beta}}\bar{\beta} + A_{3\bar{\beta}} y_{\bar{\beta}} \right]$$

$$\dot{y}_{\bar{\beta}} + 0.15\frac{U}{b} y_{\bar{\beta}} = \dot{\bar{\beta}} \tag{5.19}$$

where $A_{2\bar{\beta}_i} = \begin{bmatrix} \gamma_{o_{i_1}} & \cdots & \gamma_{o_{i_{10}}} & \alpha_{o_{i_1}} & \cdots & \alpha_{o_{i_{10}}} \end{bmatrix} \begin{Bmatrix} F_{2E_1} \\ \vdots \\ F_{2E_{10}} \\ F_{2F_1} \\ \vdots \\ F_{2F_{10}} \end{Bmatrix}$

$$F_{2E_n} = B_{2E}\Delta x b f_n (\cos\Lambda)^2$$

$$F_{2F_n} = B_{2F}\Delta x b^2 f_n (\cos\Lambda)^2$$

$$f_n = \begin{cases} 1 & \text{flap on nth section} \\ 0 & \text{no flap on nth section} \end{cases}$$

similar for $\mathbf{A}_{1\bar{\beta}}, \mathbf{A}_{0\bar{\beta}}$, and $\mathbf{A}_{3\bar{\beta}}$

There are two geometric sweep corrections (cos Λ) incorporated into the forces in Equation 5.19. One is a corrrection on the lift curve slope and the other is a correction on the flap angle, β ($\beta = \bar{\beta}\cos\Lambda$, where $\bar{\beta}$ is the flap angle referenced to the wing fixed axes). It is also important to note that b is the semichord referenced to the wind axes and Δx is the length of each spanwise strip referenced to the wind axes and that these two lengths change with change in geometric sweep.

The mass normalized aerodynamic forces are then incorporated into the equations of motion.

$$\begin{aligned}
&\mathbf{M}^*\ddot{\eta}(t)+\mathbf{B}^*\dot{\eta}(t)+\mathbf{K}^*\eta(t)+\mathbf{G}^*\hat{\mathbf{y}}(t)+ \\
&\qquad \mathbf{A}_{2\bar{\beta}}{}^*\ddot{\bar{\beta}}(t)+\mathbf{A}_{1\bar{\beta}}{}^*\dot{\bar{\beta}}(t)+\mathbf{A}_{0\bar{\beta}}{}^*\bar{\beta}(t)+\mathbf{A}_{3\bar{\beta}}{}^*\mathbf{y}_{\bar{\beta}}(t)=0 \\
&\dot{\hat{\mathbf{y}}}(t)+0.15\frac{U}{b}\hat{\mathbf{y}}(t)=\dot{\eta}(t) \\
&\dot{y}_{\bar{\beta}}(t)+0.15\frac{U}{b}y_{\bar{\beta}}(t)=\dot{\bar{\beta}}(t)
\end{aligned} \tag{5.20}$$

$$\text{where}\quad \mathbf{A}_{2\bar{\beta}}{}^* = -\frac{1}{2}\rho U^2\left(\frac{b}{U}\right)^2\mathbf{E}^{\mathrm{T}}\mathbf{A}_{2\bar{\beta}}$$

$$\mathbf{A}_{1\bar{\beta}}{}^* = -\frac{1}{2}\rho U^2\left(\frac{b}{U}\right)\mathbf{E}^{\mathrm{T}}\mathbf{A}_{1\bar{\beta}}$$

$$\mathbf{A}_{0\bar{\beta}}{}^* = -\frac{1}{2}\rho U^2\mathbf{E}^{\mathrm{T}}\mathbf{A}_{0\bar{\beta}}$$

$$\mathbf{A}_{3\bar{\beta}}{}^* = -\frac{1}{2}\rho U^2\mathbf{E}^{\mathrm{T}}\mathbf{A}_{3\bar{\beta}}$$

The flap forces are now expressed as forces on the natural, uncoupled modes in the structural axes. There is one additional lag state for the flap dynamics.

Since the aerodynamic forces are dependent on the trailing edge flap velocity and acceleration, in addition to its position, there must be a model of the flap dynamics. For simplicity, it will be assumed that the trailing edge flap has perfect oscillatory dynamics (no damping or phase shift) with

$\overline{\beta} = \overline{\beta}_o e^{i\omega t}$. Using this approximation, the flap forces can be expressed solely as a function of the commanded flap angle. In this manner, the overall system no longer includes the dynamics of the flap and the flap forces may be considered a non-homogeneous force. Now the flap dynamics and lag has been incorporated into the state space input matrix and the total number of states in the homogeneous problem remains at twelve.

$$\begin{Bmatrix} \dot{\eta} \\ \ddot{\eta} \\ \dot{\hat{\mathbf{y}}} \end{Bmatrix} = \begin{bmatrix} \mathbf{0} & \mathbf{I} & \mathbf{0} \\ -\mathbf{M}^{*-1}\mathbf{K}^* & -\mathbf{M}^{*-1}\mathbf{B}^* & -\mathbf{M}^{*-1}\mathbf{G}^* \\ \mathbf{0} & \mathbf{I} & -0.15\frac{U}{b}\mathbf{I} \end{bmatrix} \begin{Bmatrix} \eta \\ \dot{\eta} \\ \hat{\mathbf{y}} \end{Bmatrix} + \begin{bmatrix} 0 & 0 \\ \mathbf{B}_p & \mathbf{B}_{\overline{\beta}} \\ 0 & 0 \end{bmatrix} \begin{Bmatrix} v_p \\ \overline{\beta} \end{Bmatrix} \tag{5.21}$$

$$\text{where } \mathbf{B}_{\overline{\beta}} = -\mathbf{M}^{*-1}\left[-\omega^2 \mathbf{A}_{2\overline{\beta}}{}^* + i\omega \mathbf{A}_{1\overline{\beta}}{}^* + \mathbf{A}_{0\overline{\beta}}{}^* + \frac{i\omega}{i\omega + 0.15\frac{U}{b}} \mathbf{A}_{3\overline{\beta}}{}^* \right]$$

A reference frequency, ω, and velocity, U, must be chosen for the flap input matrix. The dominant term is that due to the static deflection of the flap, $A_{o_{\overline{\beta}}}{}^*$.

The reference flap design will cover 20% of the span and 20% of the chord as shown in figure 5.9. The reference location of the flap will be from 60% to 80% of the span. The location was chosen to place the flap in an area of large modal displacement, but far enough from the tip so that aerodynamic effectiveness is not lost.

Piezoelectric actuation modelling and grouping

The piezoelectric actuators are modelled as layers of the laminated plate. The forcing matrix is found by treating the piezoelectric induced strain as thermal strain and determining the effect on the assumed shapes. The forcing matrix must then be mass normalized to find the effect on the coupled modes.

To choose basic groupings and locations for the piezoelectric actuators, the strain contours of the first two in vacuo natural modes will be examined. Attention will be focused on curvature-induced strain and, therefore, curvature contours will be examined in place of strain contours. Figure 5.9, 5.10, and 5.11 show the deflection and curvature contours for the wings with fiber sweep angles of 0, -15, and -30 degrees, respectively. In each figure, the top half of the page shows the first mode's deflection and curvature contours and the bottom half shows the second mode's. There are four subplots dedicated to each mode, the deflection contour and spanwise bending, chordwise bending, and twist curvature contours. Each subplot represents the wing, cantilevered on the left with the leading edge on the bottom. The aspect ratio of each subplot is not equivalent to the actual wing aspect ratio.

The isotropic piezoelectrics can only exert extensional strain and not shear strain. The top and bottom layers of piezoelectrics may act as a bending pair, with the top compressing and the bottom extending or vice versa. Therefore, the curvature contours on which the piezoelectrics can operate are the spanwise and chordwise bending curvature contours. Because the spanwise bending curvature is roughly two orders of magnitude greater than the chordwise bending curvature, attention will be focused only on the spanwise bending curvature contour.

Examining the spanwise bending curvature contours, it is apparent that the inboard portion of the wing is high in strain. Piezoelectrics are strain actuators and should logically be placed in areas of high strain for maximum effectiveness. For these reasons, the piezoelectric actuators will cover from the root to 60% of the span.

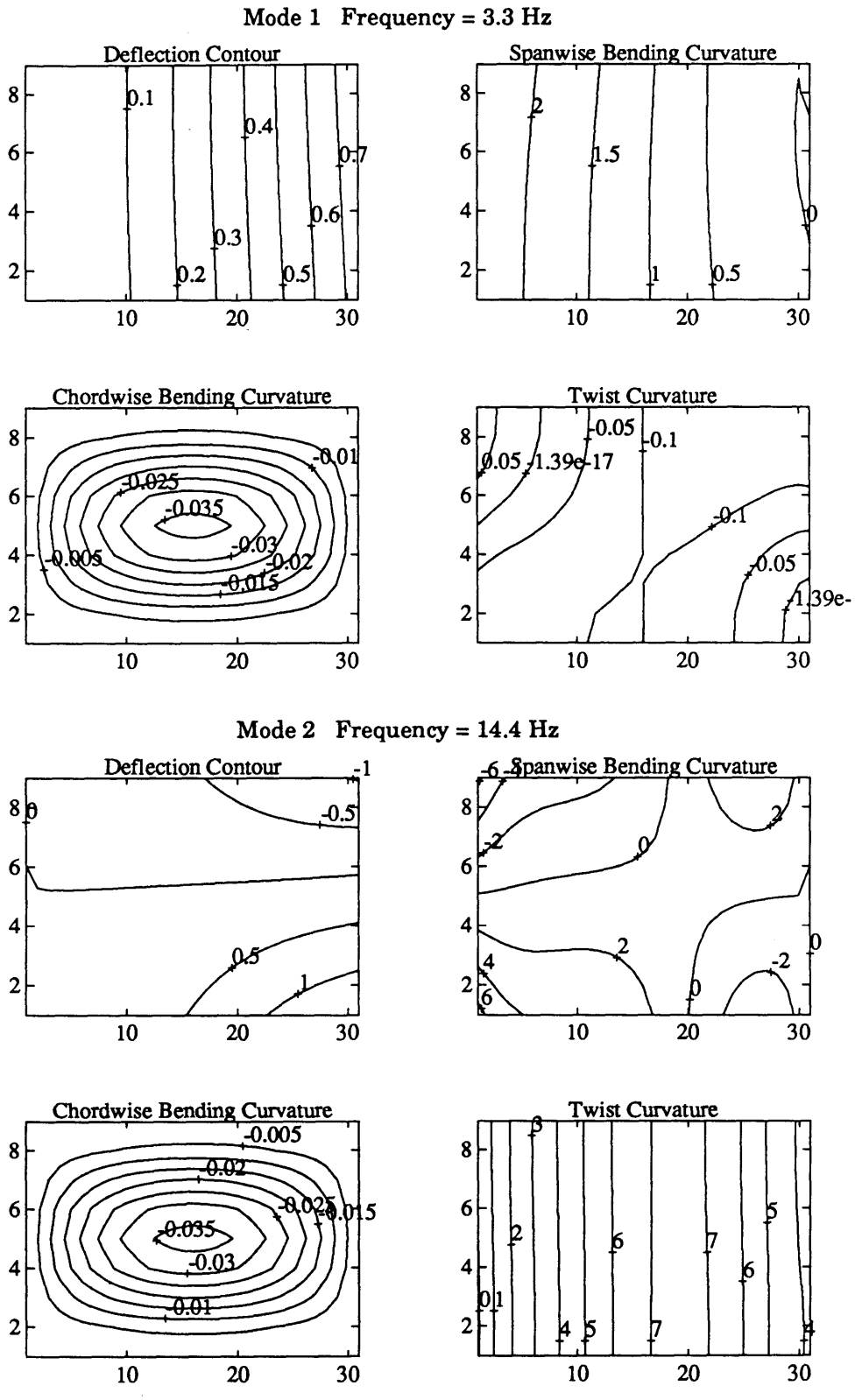

Figure 5.9 Deflection and curvature contours for the two primary modes of wing model with a [0/0/90]s laminate.

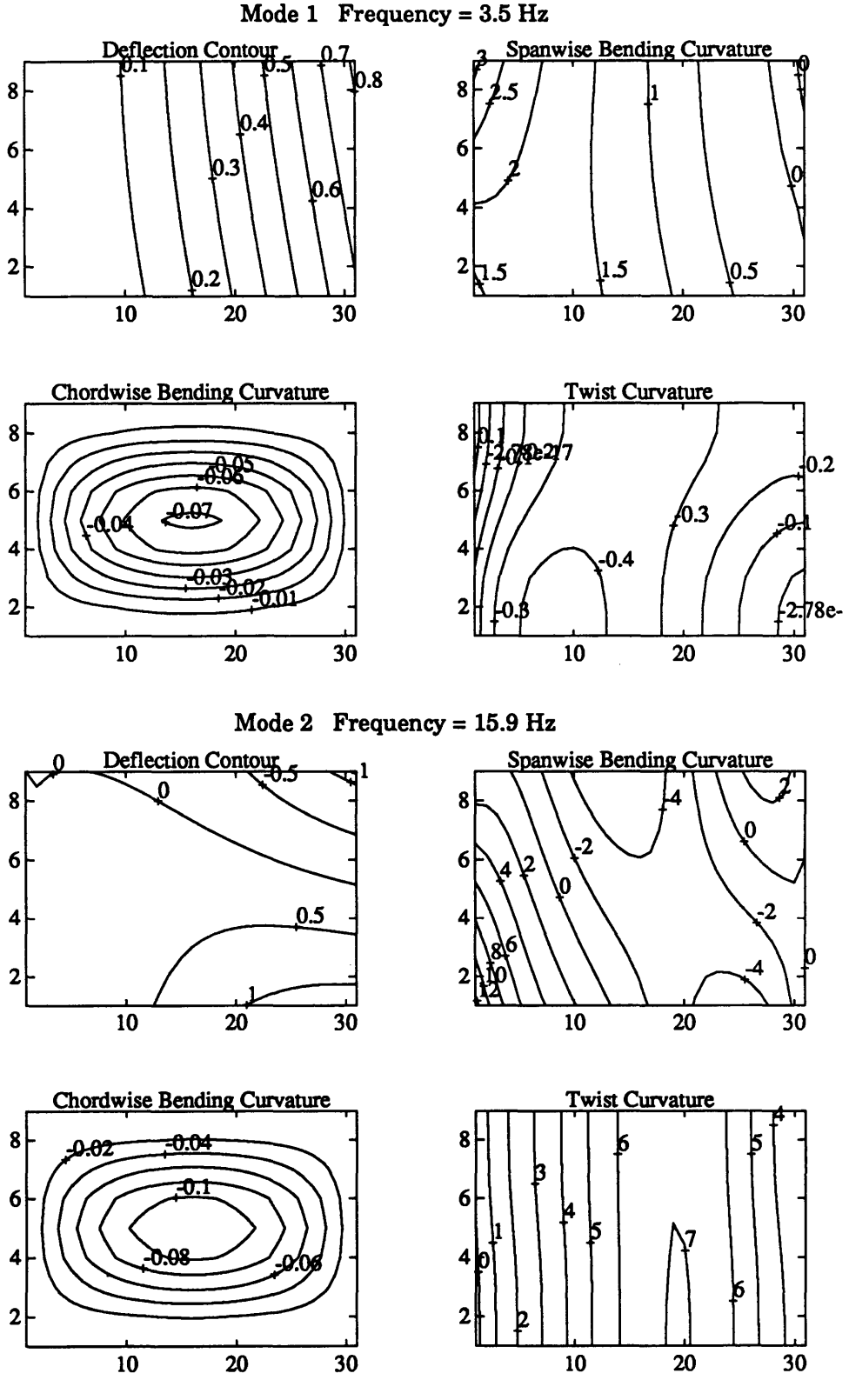

Figure 5.10 Deflection and curvature contours for the two primary modes of wing model with a [-15/-15/0]s laminate.

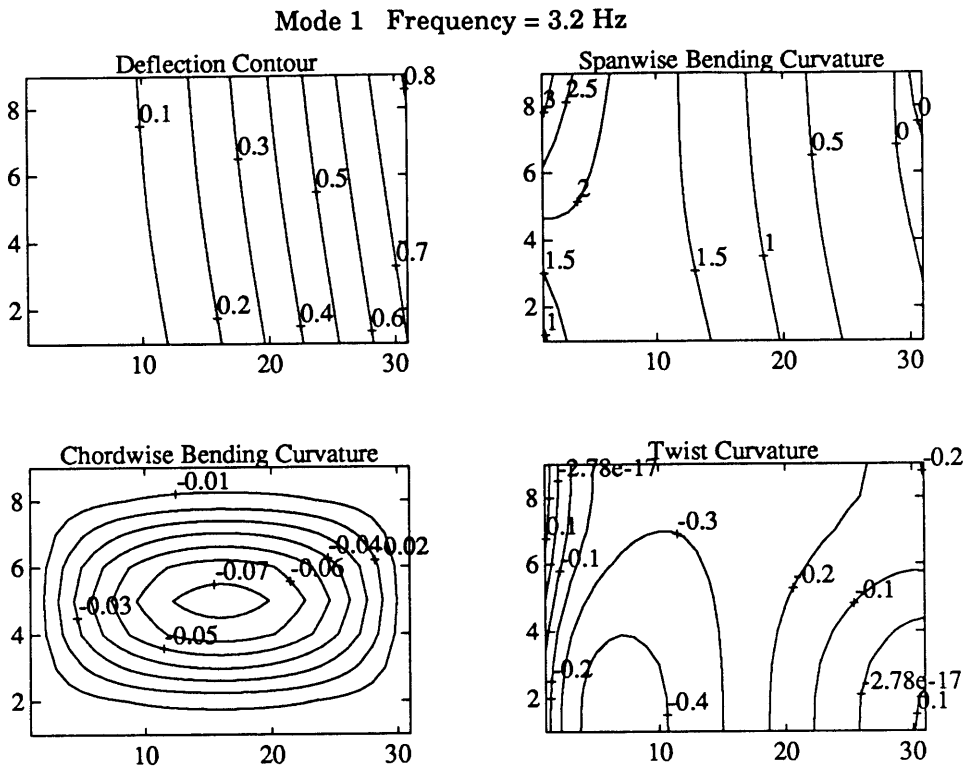

Figure 5.11 Deflection and curvature contours for the two primary modes of wing model with a [-30/-30/0]s laminate.

For a fiber sweep angle of zero degrees (Figure 5.9), the only spanwise bending curvature in the second mode is concentrated in the corners of the root and are due to root warping. For fiber sweep angles of -15 and -30 degrees (Figures 5.10 and 5.11), there are higher levels of spanwise bending curvature in the second mode due to the bend-twist coupling. This implies that the piezoelectrics will be able to exert more effective control over the second mode for these fiber sweep angles than for the zero degree fiber sweep angle. Because of this increased authority over the second mode, attention will be focused on the fiber sweep angles of -15 and -30 degrees.

For the present purposes, the piezoelectric coverage will be divided into two areas of actuator effectiveness. In the typical section analyses of Chapter 2, it has been shown that at least two independent actuators are necessary to provide effective aeroelastic control. For the fiber sweep angles of -15 and -30 degrees (Figures 5.10 and 5.11), there is a curvature nodeline in the spanwise bending curvature of the second mode at roughly 30% of the span. This indicates that dividing the piezoelectric coverage in half spanwise would create two "actuators" that can control the first two modes independently: acting together to actuate the first mode and opposing each other to actuate the second. This defines the inboard piezoelectric bank to cover from the root to 30% of the span and the outboard piezoelectric bank to cover from 30% to 60% of the span.

Full state feedback: Linear Quadratic Regulator designs

The final step of this trade study is to design a series of full state feedback controllers. Controllers will be designed using each of the actuators, the two piezoelectric actuation areas and the trailing edge flap, alone and all three actuators together. First, the fiber sweep angle will be varied and then

the geometric sweep angle will be varied. The performance of the different actuators relative to one another will be evaluated, as well as the performance of the three actuators together, and the trends across sweep angles will be examined.

The LQR method described in the typical section analyses in Chapter 2 will be used to design the controllers. For all cases, the state penalty is on the displacement states of the first two modes, which will be weighted equally. All other states are weighted at zero. The controls are weighted with representative maximum values: 200V for the piezoelectric banks and +/- 1 degree for the trailing edge flap. The 200V is approximately the coercive field of the piezoelectric.

Since the aeroelastic plant changes with change in airspeed, a reference velocity is chosen at which to evaluate the plant. The reference velocity for each of the cases is the flutter velocity determined for that particular case in Section 5.4. It is the wing at this velocity which is used in the controller designs. The flap forcing matrix, derived earlier in this section, for each case uses the flutter speed and frequency for that case as its reference speed and frequency.

As in the typical section analyses of Chapter 2, cost curves will be used to compare the controllers. The covariance of the weighted states comprises the state cost and the covariance of the weighted control inputs comprises the control cost. To compute the covariance, a disturbance is created by implementing an angle of attack variation using steady aerodynamics. The disturbance intensity is 0.1 degrees RMS.

Using a structural sweep angle of 30 degrees, the effect of fiber sweep angle on actuator authority can be seen in Figure 5.12. For each fiber sweep angle, it can be seen that the inboard piezoelectric actuation area has the best

performance. For the maximum control values assumed in this problem, the trailing edge flap and the outboard piezoelectric actuation area have nearly equivalent performance and the inboard piezoelectric actuation area performs significantly better than both the trailing edge flap and the outboard piezoelectric actuation area.

The relative performance of the piezoelectric actuators as compared to the trailing edge flap in Figure 5.12 matches the relative performance of the actuators in the typical section analysis in Figure 2.12. However, there are some significant differences. A comparison of the typical section with the current analysis shows that the trailing edge flap of the typical section was a 10 % flap with a maximum deflection of 5 degrees, whereas the trailing edge flap in the current analysis is a 20 % flap with a maximum deflection of 1 degree. A maximum deflection of 1 degree for the flap is more realistic for aeroelastic applications. In addition, the reduced frequency ($\frac{\omega b}{U}$) is decreased from 0.5 in the typical section to approximately 0.2 in the current design. The trailing edge flap demonstrates better performance for a lower reduced frequency, due to the effect of the aerodynamic lags. Finally, the piezoelectric actuation areas defined in the current analysis do not precisely parallel the piezoelectric force and moment of the typical section. The typical section piezoelectric force and moment assume piezoelectric coverage from the root to the 75 % span as compared to the 30 % span coverage of each piezoelectric actuation area in the current design. A more precise parallel would sum the effects of the two piezoelectric actuation areas for the piezoelectric "force," for maximum authority on the first mode, and difference the effects of the two actuation areas for the piezoelectric "moment," for maximum authority on the second mode.

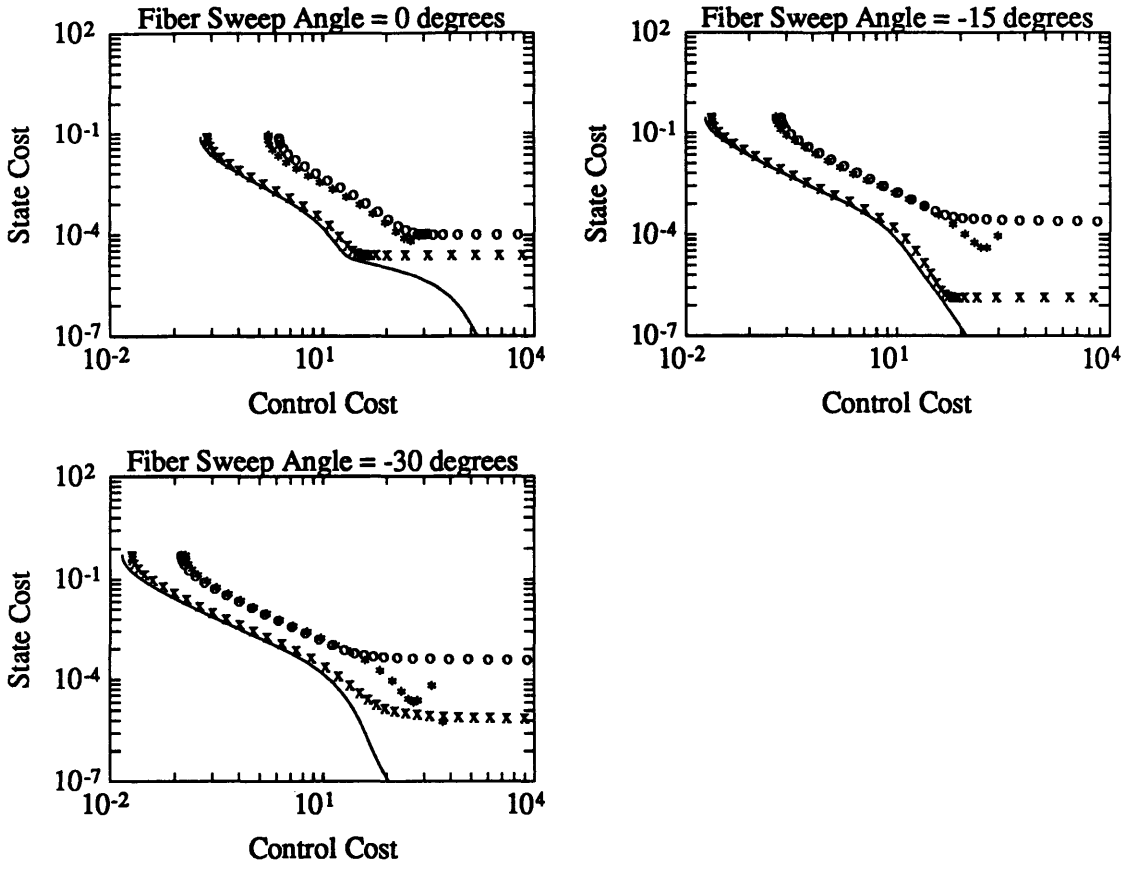

Figure 5.12 Cost curves for the wing model at a geometric sweep angle of 30 degrees for varying ply fiber angles. All cases evaluated at calculated flutter speed.

Another discrepancy with the typical section work is the performance of the controller using all three actuators. In the typical section, the controller using all three actuators performed significantly better than any of the single actuator controller designs over all control cost regions (Figure 2.12). In Figure 5.12 it can be seen that the controller using all three actuators performs only slightly better than the best single actuator controller design in the low control cost region. This can be explained by

examining the different flutter mechanisms. The typical section has a perfect two mode coalescence (Figures 2.3 and 2.4) in contrast to the coalescence of the current design (Figure 5.7). In the current design, the flutter mechanism is dominated by the first mode. For the typical section, it was important to be able to exert effective control over both of the modes because of the classic coalescence. For the current design, it is more important to be able to exert effective control over the first mode. The single actuators are capable of exerting effective control over the first mode alone and, therefore, evidence a better performance relative to the combination of all three actuators in the current design as compared to the typical section.

Although the single actuators perform well in the low control cost region, each of the single actuator curves has a horizontal asymptote in the high control cost region. In contrast, the combination of three actuators has no such limit. This inherent performance limit of a single actuator has been seen in the typical section analyses (Chapter 2) and demonstrates that effective high authority aeroelastic control requires at least two actuators.

The cost curve comparison reiterates the benefit of the bend-twist coupling introduced by the fiber sweep angles of -15 and -30 degrees. The single actuator curves of the zero degree fiber sweep angle show equivalent performance to the single actuator curves of the -15 and -30 degree fiber sweeps. However, the strain contours demonstrated that effective control of the second mode requires the two piezoelectric actuation areas acting in opposition. This indicates that the single actuator cases are only controlling the first mode effectively. The benefit of bend-twist coupling is most clearly seen in the curves of the three actuators working together. The three actuator curve of the zero degree fiber sweep angle does not have the performance limitation of the single actuator curves, but it does not improve

the performance beyond this limit as well as the corresponding curve for fiber sweep angles of -15 and -30 degrees.

These same results may also be seen in comparison of the structural sweep angles at a ply fiber angle of -15 degrees (see Figure 5.13). The single actuator performance limitations are shown with the same relative actuator authorities. As before, when more than one actuator is used, the performance becomes unlimited.

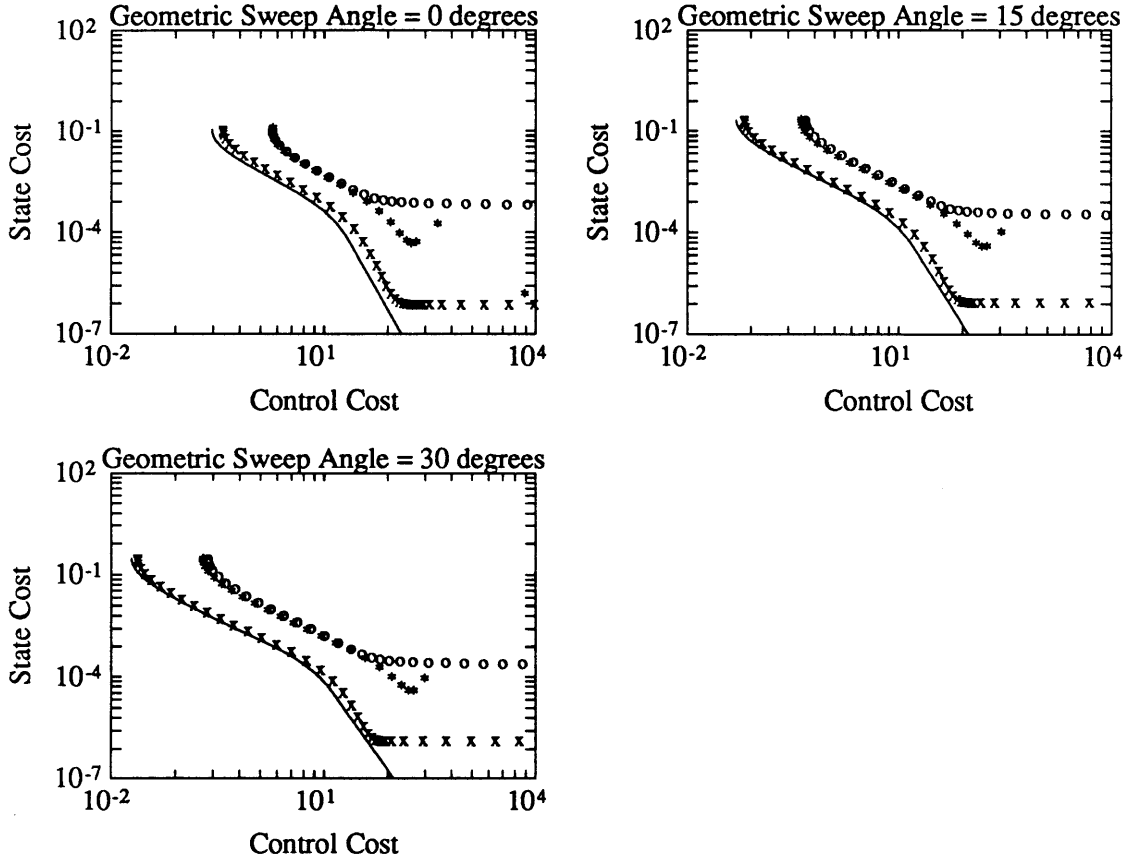

Figure 5.13 Cost curves for the wing model with a [-15/-15/0]s laminate for varying geometric sweep angles. All cases are analyzed at the calculated flutter speed.

5.6 Summary

The original trade space of fiber sweep angles of -45, -30, -15, 0, 15, 30, and 45 degrees and geometric sweep angles of -30, -15, 0, 15, and 30 degrees was reduced based on performance requirements and the analyses outlined in this chapter. The wing model must flutter before it diverges [PR4]. To satisfy this requirement, the trade space was reduced to fiber sweep angles of 0, -15, -30, and -45 degrees and geometric sweep angles of 0, 15, and 30 degrees based on the stability analyses of a simple rectangular plate. Further stability analyses were completed on a built-up wing model. The fiber sweep angle of -45 degrees was eliminated from further consideration because it had a complex three mode flutter mechanism [PR5]. Finally, actuator analyses showed that a fiber sweep angle of 0 degrees, lacking bend-twist coupling, does not provide a means for adequate control of the second mode by piezoelectric actuators [PR14]. The remaining trade space includes fiber sweep angles of -15 and -30 degrees and geometric sweep angles of 0, 15, and 30 degrees.

The baseline fiber sweep angle and geometric sweep angle must now be chosen from the reduced trade space. The physical model goals in Chapter 3 state that the wing model should be representative of aircraft in which bending/torsion flutter is critical. Therefore, a baseline fiber sweep angle of -15 degrees will be chosen since its second mode more closely resembles a torsional mode than the second mode of the -30 degree fiber sweep angle. Likewise, a baseline geometric sweep angle of 30 degrees will be chosen for similarity based upon the survey of transport aircraft in Chapter 4. The remaining trade studies involving the flutter stopper and the taper ratio will be conducted in the following chapters using the analysis techniques developed in this chapter.

Table 5.3 Summary of current reference and baseline values for design parameters. **Bold** indicates a baseline value.

Geometrical	Span (half)	48 in.
	Aspect ratio (full span)	8
	Geometric sweep angle	**30 deg.**
	Airfoil shape	**NACA 64-012**
	Aerodynamic thickness ratio	**12 %**
	Aerodynamic taper ratio	> 0.25
Structural	Spar thickness ratio	**2 %**
	Spar taper ratio	> 0.25
	Laminate layup	**[θ / θ / 0]s**
	Fiber sweep angle	**-15 deg.**
	Facesheet material	**AS4/3501-6**
	Core material	**Aluminum honeycomb**
Actuation	Flap chord ratio	**20 %**
	Flap span ratio	**20 %**
	Flap location	**60 % to 80 % of span**
	Piezoceramic area coverage	**root to 60 % of span**
	Piezoceramic thickness	**0.020 in.**
	Piezoceramic sectioning	**root to 30 % of span**
		30 % to 60 % of span

Chapter 6: Design Trade 2: Tip Mass Flutter Stopper

6.1 Introduction

As outlined earlier in the requirements in Chapter 3, the wing model must have a mechanism which will aeroelastically stabilize the model after it has begun to flutter. This chapter discusses the basic mechanism of a tip mass flutter stopper and examines the relevant trade studies used to select design parameters to meet the requirement. The goal of a tip mass flutter stopper is to enable a change in properties of the wing model such that the wing model with the stopper deployed will have a significantly higher flutter speed than the wing model with the stopper undeployed. The flutter speed when deployed dictates the highest speed at which flutter suppression may be demonstrated, since the model will not be stabilizable at any higher speed.

Two principle mechanisms for this flutter stopper design will be examined to understand their effects on the flutter speed. The first mechanism is a change in the location of the center of gravity. Using a simplified typical section, Bisplinghoff, Ashley, and Halfman derived an expression for the flutter speed [Equation 9-22 in Bisplinghoff, et al. 1955] (Equation 6.1). The denominator of the second fraction under the radical in Equation 6.1 represents the distance of the center of gravity aft of the quarter chord, or aerodynamic center. As the center of gravity is moved closer to the quarter chord, the flutter speed increases, and as the center of gravity is moved further aft, the flutter speed decreases. It is this quality that will be exploited in the flutter stopper design.

$$\frac{U_F}{b\omega_\alpha} \cong \sqrt{\frac{m}{\pi\rho b^2}\frac{R_\alpha^2}{\left[1+2(a+x_\alpha)\right]}}$$

where $\frac{m}{\pi\rho b^2}$ is the density ratio

R_α^2 is the dimensionless radius of gyration

a is the distance of the elastic axis aft of the midchord nondimensionalized by b

x_α is the distance of the center of gravity aft of the elastic axis nondimensionalized by b

ω_α is the uncoupled natural torsional frequency

b is the semichord (6.1)

The second principle flutter stopper mechanism to be studied is the torsional inertia. A decrease in the torsional inertia should, in turn, increase the torsional frequency and increase the frequency separation. The increase in the frequency separation should delay coalescence and raise the flutter speed. The torsional moment of inertia due to the flutter stopper may be separated into two components.

$$I = I_{C.G.} + mr^2 \tag{6.2}$$

The first, distributed, component is the moment of inertia about the center of gravity of the device. The second, parallel-axis, component is the moment of inertia due to the displacement of the center of gravity from the reference axis. A change in one or both of these terms can be exploited in the design of a flutter stopper. Here the appropriate reference axis is the elastic axis of the wing (see Equation 2.18 and Figure 2.15).

This chapter discusses the design trades studied to obtain a flutter stopper design which will achieve the desired flutter speed margin of 1.3. The initial design uses a distributed mass attached to the wing spar at two

points, one a hinge and the other a retractable pin. When deployed, the pin retracts and the mass will be free to rotate about the hinge point. This design takes advantage of changes in the torsional inertia and a change in the center of gravity location. First, the hinge location will be optimized to achieve the highest flutter speed ratio. Using the optimal hinge location, the mass of the flutter stopper will be varied to understand its effects and to choose an appropriate mass. Finally, the length of the flutter stopper will be varied and the effects of this parameter studied.

6.2 Variation in hinge position

Based upon the wing model described in the previous chapter (Section 5.4), the effects of the hinge location of the deployed flutter stopper on the flutter speed are examined in this section. The trade study will consider the baseline layup of [-15/-15/0]s and the baseline geometric sweep angle of 30 degrees. The model with the undeployed flutter stopper is exactly the wing model described in chapter 5, a rectangular wing with an aerodynamic chord of 15.6 in. and span of 48 in. and with an evenly distributed mass attached to the tip with a 15.6 in. chord and 3 in. span (see Figure 5.5). The deployed flutter stopper will be represented by the flutter stopper mass concentrated in a 3 in. by 3 in. area centered on the actual hinge location (Figure 6.1). Five different hinge locations are to be examined: the leading edge (y centroid of -5.1 in.), the midchord (y centroid of 1.2 in.), the trailing edge (y centroid of 7.5 in.), and two intermediary positions with y centroids of -3.6 in. and -2.1 in. The mass of the tip mass flutter stopper for the current trade is the reference value of 2.2 lbs (1 kg).

Using the structural and aerodynamic analysis of Chapter 5 (Section 5.2), the flutter speed of the wing model with the flutter stopper undeployed

and the flutter speeds of the deployed flutter stopper at the five different hinge locations are found. Figure 6.2 shows the flutter speeds for the various configurations and Figure 6.3 shows the flutter speed and dynamic pressure ratios. Clearly, the leading edge hinge position provides the largest increase in flutter speed. The change in flutter speed is remarkably linear with hinge position.

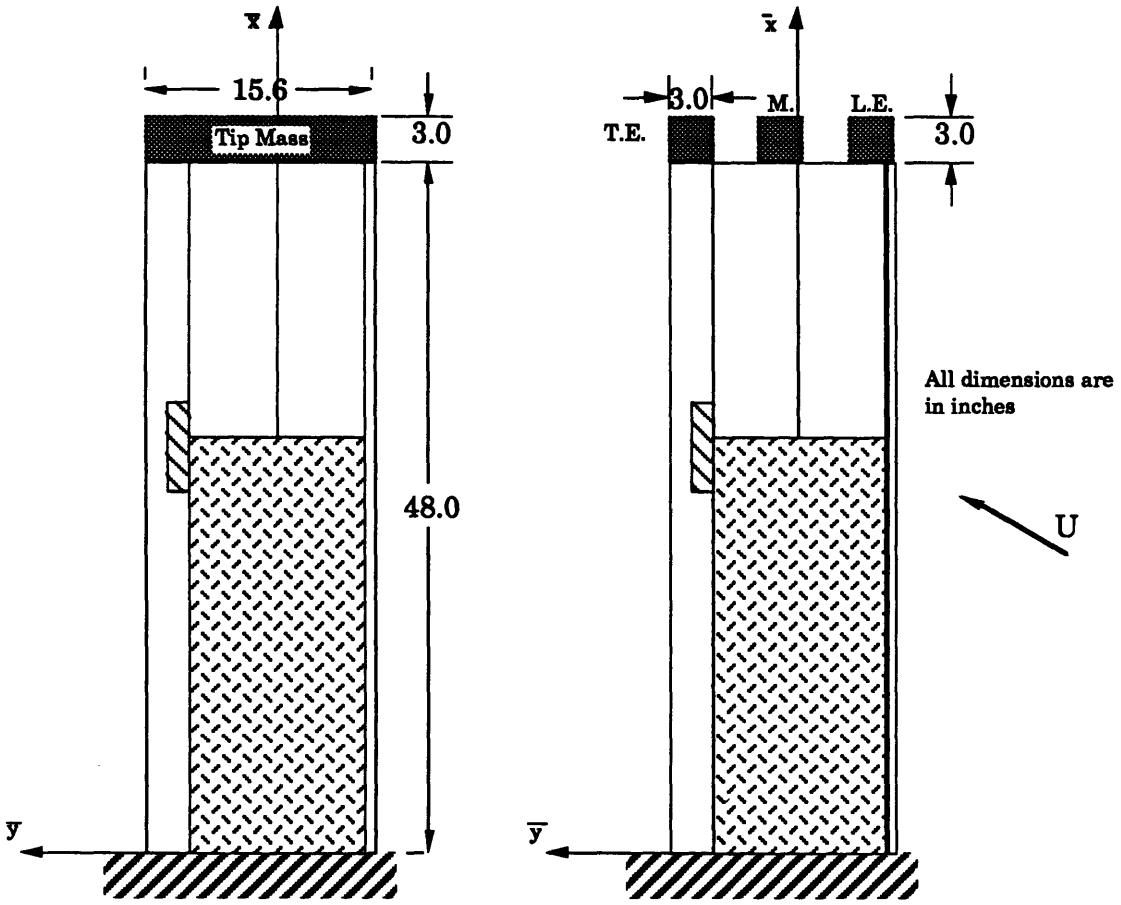

Figure 6.1 Schematics of nominal wing model and wing model with typical flutter stopper deployed positions. Only leading edge, trailing edge, and middle locations shown for clarity.

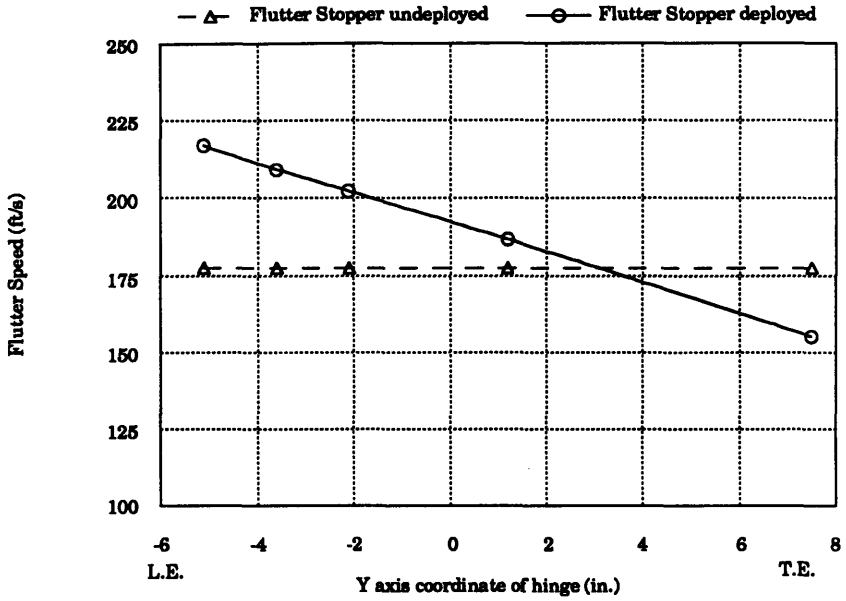

Figure 6.2 Fixed and deployed flutter speeds for hinge position trade. Midpoint of deployed area used as y axis coordinate of hinge. Mass is 2.2 lbs (1 kg). Undeployed length is 15.6 in.

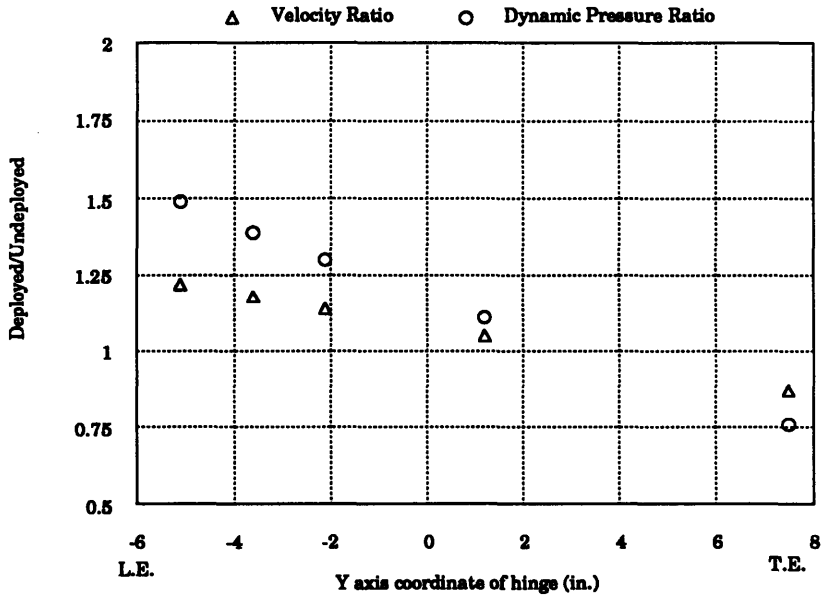

Figure 6.3 Deployed/undeployed flutter speed and dynamic pressure ratios for hinge position trade. Midpoint of deployed area used as y axis location. Mass is 2.2 lbs (1 kg). Undeployed length is 15.6 in.

Comparing the flutter speeds of the various deployed positions changes both the parallel-axis component of the torsional inertia and the location of the wing center of gravity. The mass concentrated at the leading edge provides the lowest torsional inertia being located the closest to the elastic axis as defined in Chapter 2. It also moves the center of gravity of the wing the furthest forward and, therefore, the closest to the quarter chord. Lowering the torsional inertia should raise the torsional frequency. However, Figure 6.4 demonstrates that the torsional (second mode) frequency is not increased from the distributed flutter stopper mass to the concentrated mass at the leading edge. This implies that the dominant effect is the change in the wing center of gravity.

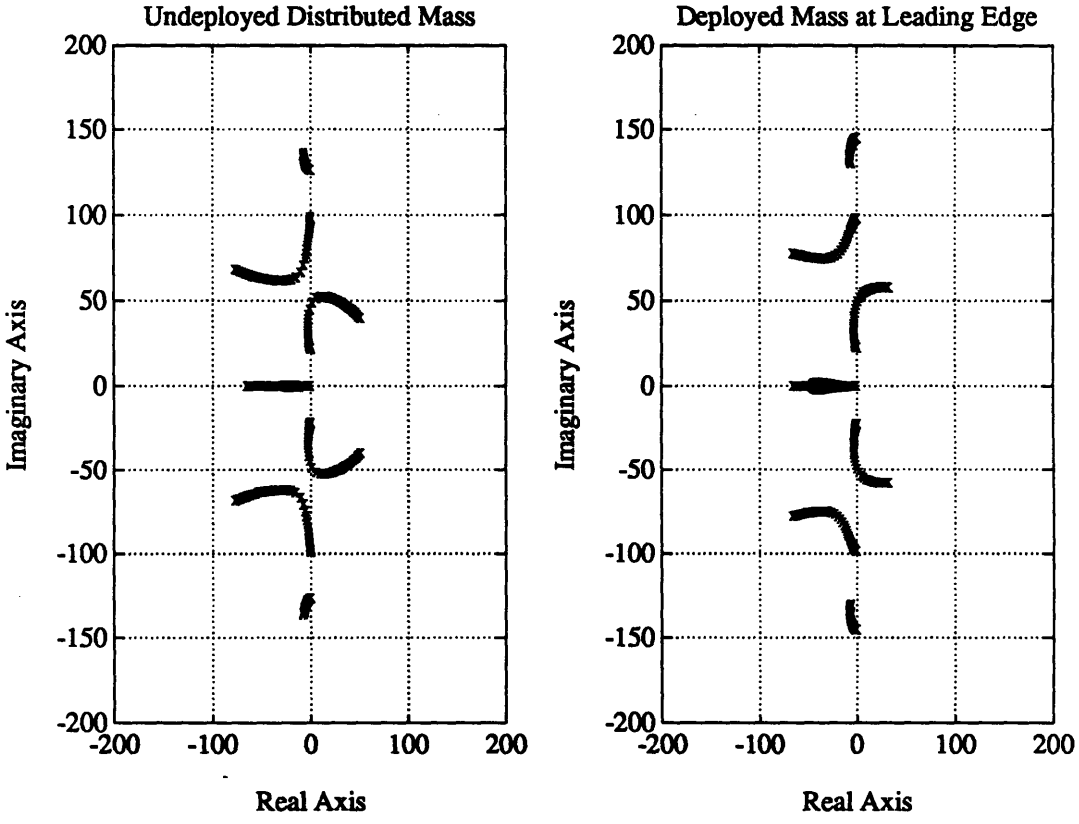

Figure 6.4 Pole loci for the undeployed flutter stopper and the deployed flutter stopper at the leading edge hinge position. (U = 0 to 100 m/s) Mass is 2.2 lbs (1 kg) and undeployed length is 15.6 in.

Comparing the flutter speeds of the distributed mass to the concentrated mass at the midchord isolates the effect of changing the torsional inertia. Reducing the distribution of mass reduces the torsional inertia and, therefore, increases the flutter speed (Figure 6.2). However, the increase in flutter speed due to this change in torsional inertia is fairly small, specifically when compared to the effect of changing the center of gravity location. In fact, moving the concentrated mass slightly aft of the midchord achieves the same effect as the change in distribution, as indicated by the intersection of the two lines in Figure 6.2. Thus the important parameter in raising the flutter speed is the change in the location of the center of gravity of the wing and the forward most position of the concentrated mass is optimal. This is chosen as the baseline hinge position.

6.3 Variation in mass

Now that the hinge position has been optimized, the effects of increasing the mass will be studied. The models of the undeployed stopper mechanism will use the distributed mass model and the models of the deployed stopper mechanism will use a mass concentrated in a 3 in. by 3 in. area at the leading edge. The mass will be increased from 2.2 lbs (1 kg) to 5.5 lbs (2.5 kg) in increments of 0.55 lbs (0.25 kg). As before, the baseline layup and geometric sweep angle will be used.

The same analysis techniques will be used to determined the flutter speeds. For this trade study, the undeployed models' flutter speeds must be recalculated as the mass has changed from the reference model studied in Chapter 5. The flutter speeds may be seen in Figure 6.5 and the speed and dynamic pressure ratios may be seen in Figure 6.6.

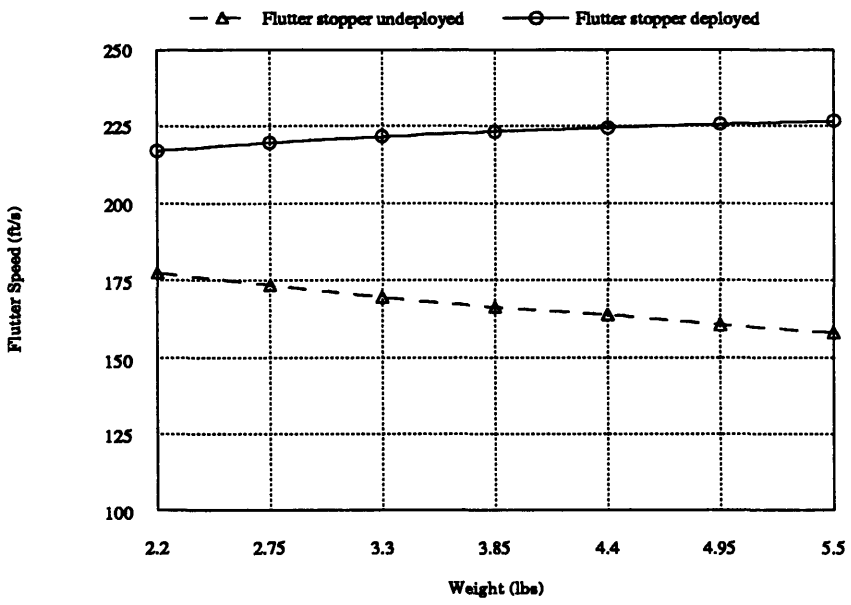

Figure 6.5 Undeployed and deployed flutter speeds for mass trade. Leading edge hinge position used for deployed stopper. Undeployed length is 15.6 in.

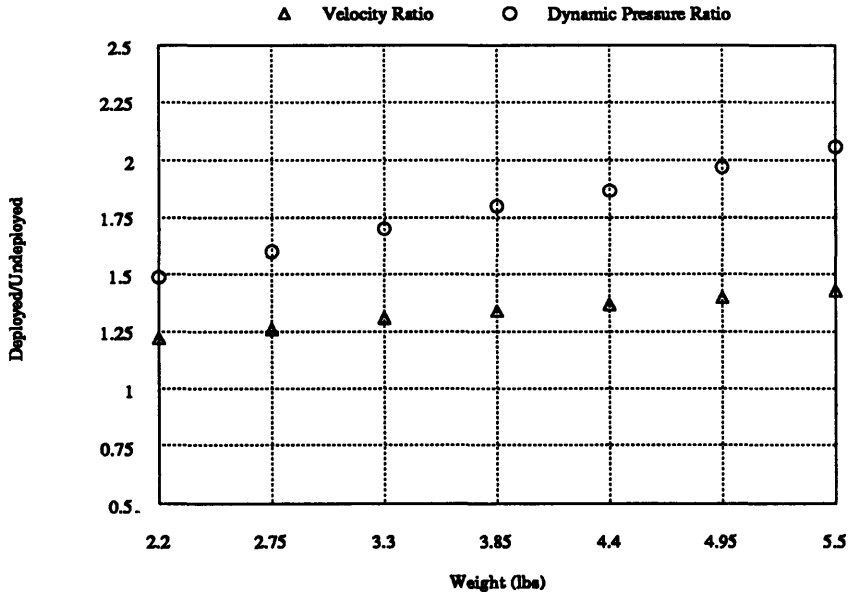

Figure 6.6 Deployed/undeployed flutter speed and dynamic pressure ratios for mass trade. Leading edge hinge position used for deployed stopper. Undeployed length is 15.6 in.

The increase in tip mass amplifies the tip mass' effect on the location of the center of gravity. This is due to the fact that the mass of the flutter stopper relative to the mass of the wing is larger and the movement of the center of gravity of the flutter stopper will, therefore, have more effect on the center of gravity of the wing as a whole. The increase in mass affects both the undeployed and deployed flutter speeds.

The end result is that the flutter speed ratio increases with increasing tip mass. However, this is due not only to an increase in the flutter speed of the deployed model, but also to a decrease in the flutter speed of the undeployed model. It is generally undesirable to lower the nominal flutter speed, or the undeployed flutter speed and the tip mass should not be increased indiscriminately. Therefore, to achieve the goal flutter speed ratio of 1.3 without adding large amounts of mass, the baseline mass will be 3.3 lbs (1.5 kg).

6.4 Variation in length

As a final trade, a change in the length of the flutter stopper will be examined. Since the wing is to resemble a transport type wing, which sometimes have extensions behind their tips but rarely in front, the length extension will only be extended behind the trailing edge. The reference length is 15.6 in., the aerodynamic chord length of the wing. The range of lengths to be studied is 15.6 in. to 27.6 in. in increments of 3 in. The baseline layup and baseline geometric sweep angle are used and the mass of the flutter stopper is kept constant at the reference 2.2 lbs (1 kg). The deployed state is a mass concentrated in a 3 in. by 3 in. area centered on the baseline leading edge hinge position. Figures 6.7 and 6.8 show the flutter speeds and ratios achieved by the variation in length.

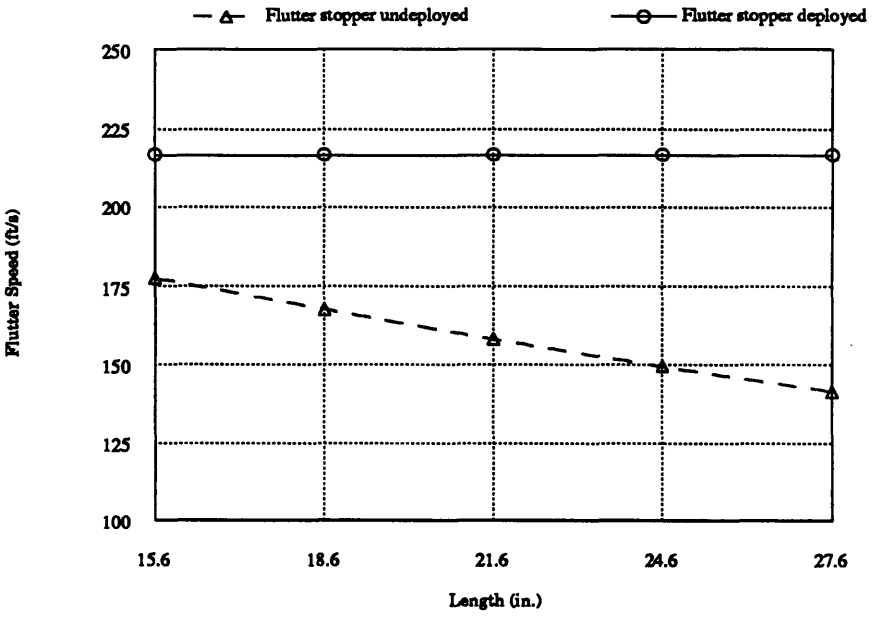

Figure 6.7 Undeployed and deployed flutter speeds for length trade. Leading edge hinge position used for deployed stopper. Mass is 2.2 lbs (1 kg).

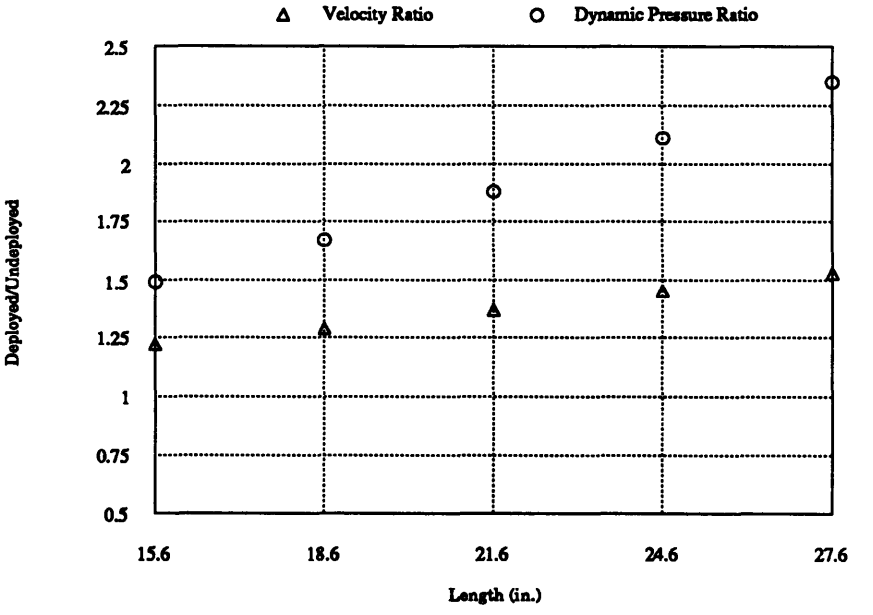

Figure 6.8 Deployed/undeployed flutter speed and dynamic pressure ratios for length trade. Leading edge hinge position used for deployed stopper. Mass is 2.2 lbs (1 kg).

The increase in the flutter speed ratio is solely due to the decrease in flutter speed with the stopper undeployed. The flutter speed of the deployed state does not change, since the change in length only affects the wing properties when the stopper is fixed to the spar. Increasing the length moves the center of gravity of the flutter stopper, and, therefore, the wing center of gravity, further aft of the quarter chord. This decreases the flutter speed of the undeployed model. Since the deployed model's flutter speed is constant, the speed ratio increases. Since it is much less desirable to achieve the desired speed ratio by decreasing the flutter speed of the nominal plant and the extension behind the trailing edge is somewhat unrealistic, no extension will be baselined.

6.5 Final design

Based on the trade studies on hinge position, mass, and length, the flutter stopper design has been baselined. The hinge position chosen is at the leading edge since it provides the largest change in flutter speed. The mass is set at 3.3 lbs (1.5 kg) to achieve a flutter speed ratio of 1.3. The length will remain as the chordlength to maintain realism.

Having examined the trades, an alternative flutter stopper mechanism is proposed. It has been observed that the movement of the center of gravity dominates the change in flutter speed. A less complicated design uses a movable mass rather than a hinged mass [Hwang, et al. 1980]. In this manner, the mechanism may remain fixed to the wing even when deployed. This eliminates concerns about the dynamics of the hinged mass after deployment. The same flutter speed ratio as the current design may be obtained by simply making the initial position of the mass slightly aft of the midchord and the final position the leading edge. The baseline mass will be

3.3 lbs (1.5 kg). The aeroelastic influence of the movable mass is the same as the hinged design. The dynamics of the movable mass are more fully understood and, in fact, better represented by the models made in this section. It is therefore recommended as the baseline design.

Chapter 7: Design Trade 3: Taper Ratio

7.1 Introduction

The final trade that will be examined in this design process is a taper ratio trade. Typical transport wings have tip chords which are considerably smaller than the root chords. The survey of Chapter 4 indicated typical taper ratios range from 0.30 to 0.16. The taper ratios examined in this chapter will range from 1 to 0.5. These taper ratios are intended to resemble a taper ratio of a transport wing if the trailing edge angle in the outer wing panel is continued to the root and exclude the extra wing area often included at the trailing edge/fuselage junction area.

To choose a nominal taper ratio for the wing design, the taper ratios and the changes they induce will be studied. The preliminary step defines the models and the changes that are required in the aerodynamic analysis. Then, using the modified models, the flutter speeds and frequencies will be calculated. Finally, it will be seen how the taper ratio affects the authority of the actuators.

7.2 Structural and aerodynamic models

The only change in the structural model from the nominal wing is the taper ratio. The wing will have the baseline layup of [-15/-15/0]s and the baseline geometric sweep angle of 30 degrees. The tip mass will remain as it was modelled in the reference model of Chapter 5, a 2.2 lbs (1 kg) distributed weight. The taper ratio will be introduced by holding the tip chord of the spar constant and altering the root chord accordingly. The aspect ratio will be

reduced by a small amount because of the introduction of taper in this manner. Figure 7.1 shows a typical taper ratio model with a taper ratio 0.67. Taper ratios of 0.5, 0.67, and 0.75 will be studied.

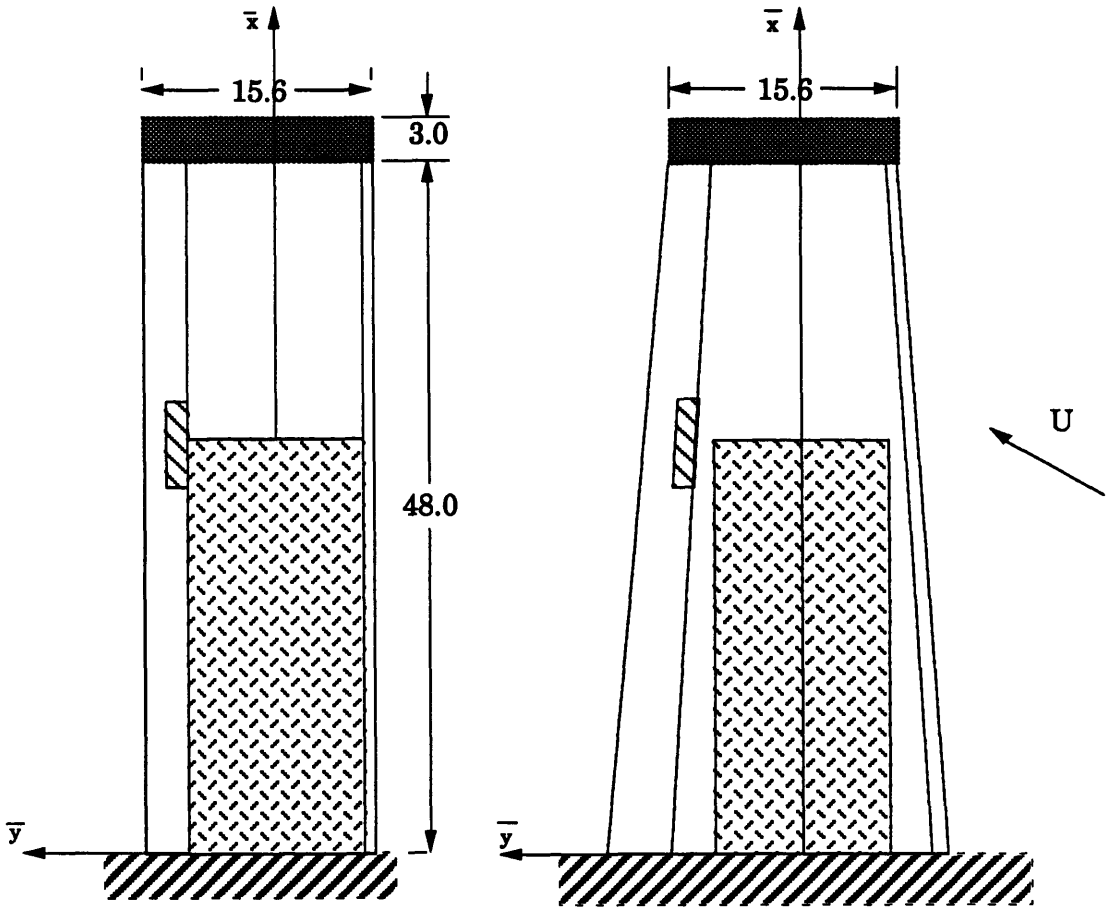

Figure 7.1 Schematic of wing model with taper. Taper ratio of 0.67 shown.

The structural model for the Rayleigh-Ritz method includes the extra skin and spar introduced by the taper. Due to limitations in the integration code used, the taper is actually approximated by four 12 in. spanwise steps for the leading edge and four 12 in. spanwise steps for the trailing edge. The step height is roughly determined by the height of the tapered edge at the midpoint of the step. A total of eight steps model the additional skin mass and eight steps model the additional spar area. The additional spar area has

mass and stiffness properties. No piezoelectrics are modelled on the additional spar area.

The aerodynamic model must also account for the tapered chord. A reference chord is chosen at the 3/4 span point. The wing is again divided into ten spanwise strips for the two dimensional strip theory analysis. The generalized aerodynamic forces on each strip use the semichord of the midpoint of that strip. The equations with the taper included may be seen in Appendix D.

7.3 Flutter analysis

Before performing the stability analysis, the natural modes will be determined. The frequencies of the first three modes are listed in Table 7.1.

Table 7.1 Natural frequencies for first three modes of tapered and nominal wing models. (Hz)

	Taper Ratio			
Mode	0.5	0.67	0.75	1.0
1B	4.1	3.8	3.7	3.5
2B	21.1	20.6	20.6	20.3
1T	15.5	15.7	15.7	15.9

It is apparent that the change in frequencies is not large when the taper ratio is changed. Likewise, the order in which the modes appear is maintained. The larger the taper ratio, the closer the behavior is to the non-tapered model.

Incorporating the aerodynamics and analyzing the stability of the aeroelastic system, it becomes apparent that the incorporation of taper ratio

affects the aeroelastic behavior very little. The flutter speeds for the different taper ratios are listed in Table 7.2.

Table 7.2 Flutter speeds and frequencies for tapered and nominal wing models.

	Taper Ratio			
Flutter	0.5	0.67	0.75	1.0
Speed (m/s)	55.1	54.1	54.0	54.1
Frequency (Hz)	8.3	7.8	7.7	7.5

The overall change in flutter speed is insignificant. Similarly, the pole loci for the tapered wing models closely resemble the non-tapered model (see Figure 5.8) and a representative pole loci may be seen in Figure 7.2.

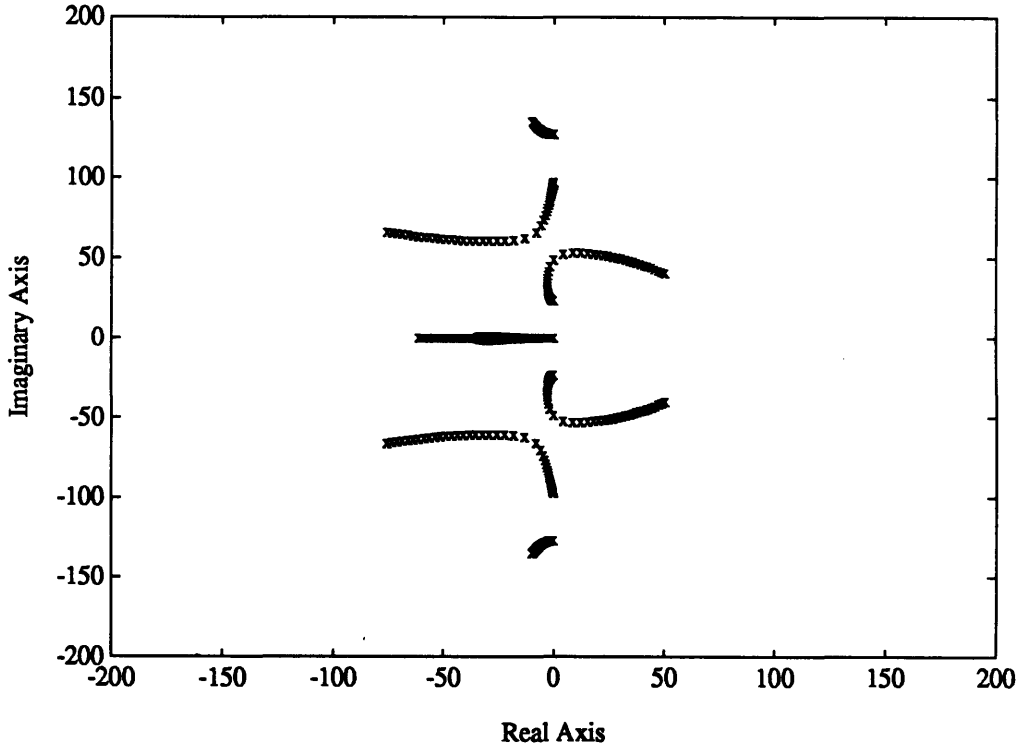

Figure 7.2 Pole locus for wing model with a taper ratio of 0.67. Fiber sweep angle is -15 degrees, geometric sweep angle is 30 degrees. U = 0 to 100 m/s

Part of this robustness to change in taper ratio is due to the manner in which the taper was introduced. By maintaining the tip dimensions, the effect of the change in taper has been limited. Clearly, the tip and its properties are dominant in determining the dynamic and aeroelastic behavior of the wing. Adding material near the root has little effect on the behavior and the desired dynamics have been maintained. For a representative taper ratio with a realistic transport wing profile, a taper ratio of 0.67 is chosen as a reference taper ratio.

7.4 Effect on actuation

As a final step in ensuring that the addition of taper has not altered the wing design appreciably, the effect on the actuator authority will be observed for the reference taper ratio of 0.67. First, the curvature contours will be reproduced to verify that the definition of the primary banks of piezoelectrics is still appropriate. Then controllers will be designed using the Linear Quadratic Regulator method and the cost curves will be examined.

Like the non-tapered wing model in Chapter 5, the curvature contours of the first two modes of the tapered wing model are examined to determine a rough grouping of piezoelectric actuators. As discussed in Section 5.5, the goal of the grouping is to enable independent control of the first two modes. Since the piezoelectrics being used are in-plane isotropic, twist curvature can not be induced. As a result, the piezoelectrics only actuate through the bending curvature. As the curvature contours in Figure 7.3 show, only the spanwise bending curvature is significant. The reference piezoelectric coverage is from the root to 60 % of the span and the actuation areas are defined from the root to 30 % of the span and 30 % to 60 % of the span. The division of the piezoelectric actuation areas is roughly defined by the position

of the curvature nodeline in the second mode. Examining Figure 7.3, these groupings will still provide the independent control needed: acting together to actuate the first mode and acting oppositely to actuate the second mode.

The final step is to design the LQR controllers and check the cost curves for trends similar to those of the non-tapered wing model. The controllers are designed using the same weightings as before and under the same disturbance. The cost curves in Figure 7.4 closely resemble those for the non-tapered wing model (upper right corner of Figure 5.12). The inboard piezoelectric actuation area and the flap are well matched in authority as for the non-tapered wing model. The inboard piezoelectric bank proves again to be the most effective but is still fairly well matched by the flap and the outboard piezoelectric bank.

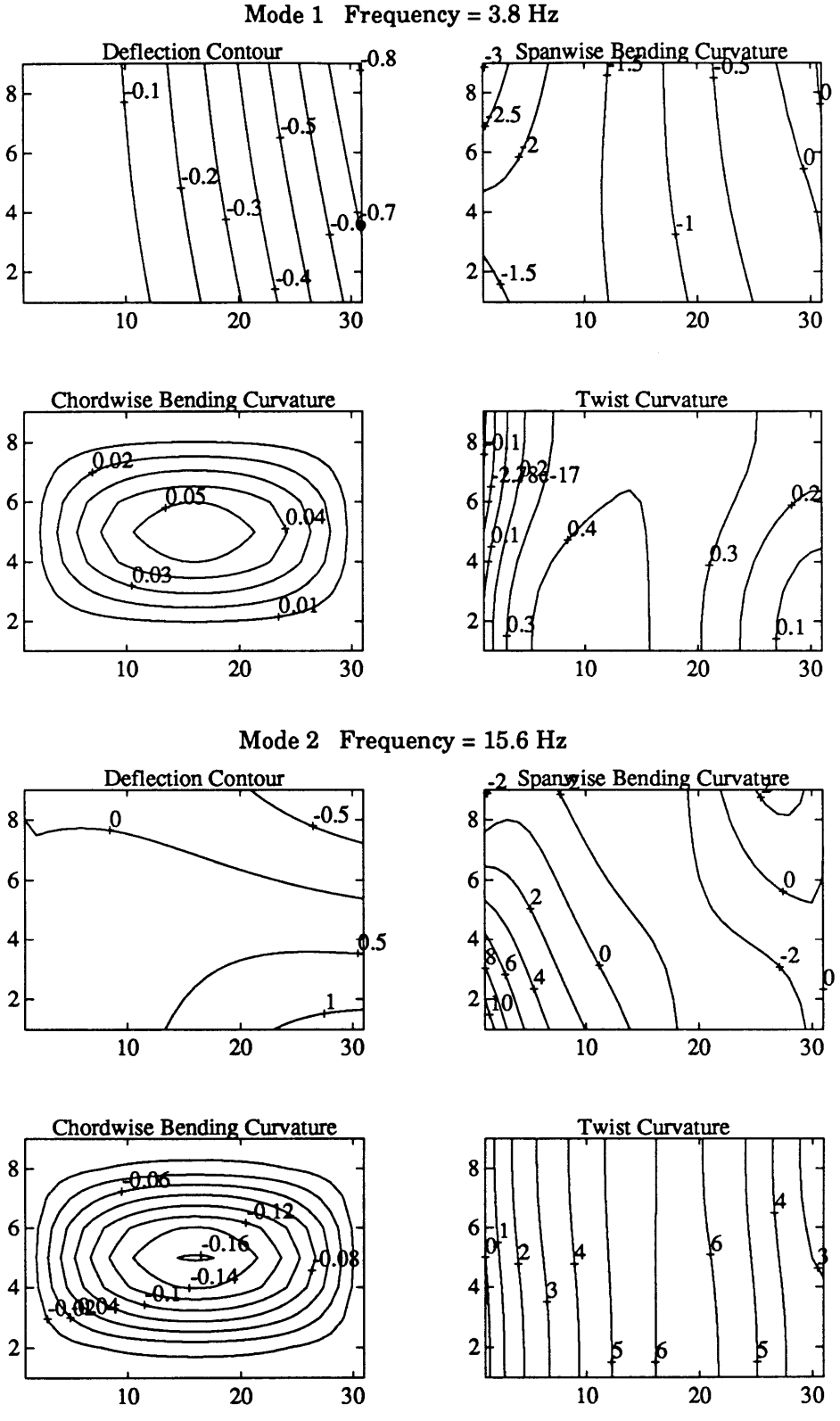

Figure 7.3 Curvature contours for wing model with a taper ratio of 0.67. Fiber sweep angle is -15 degrees.

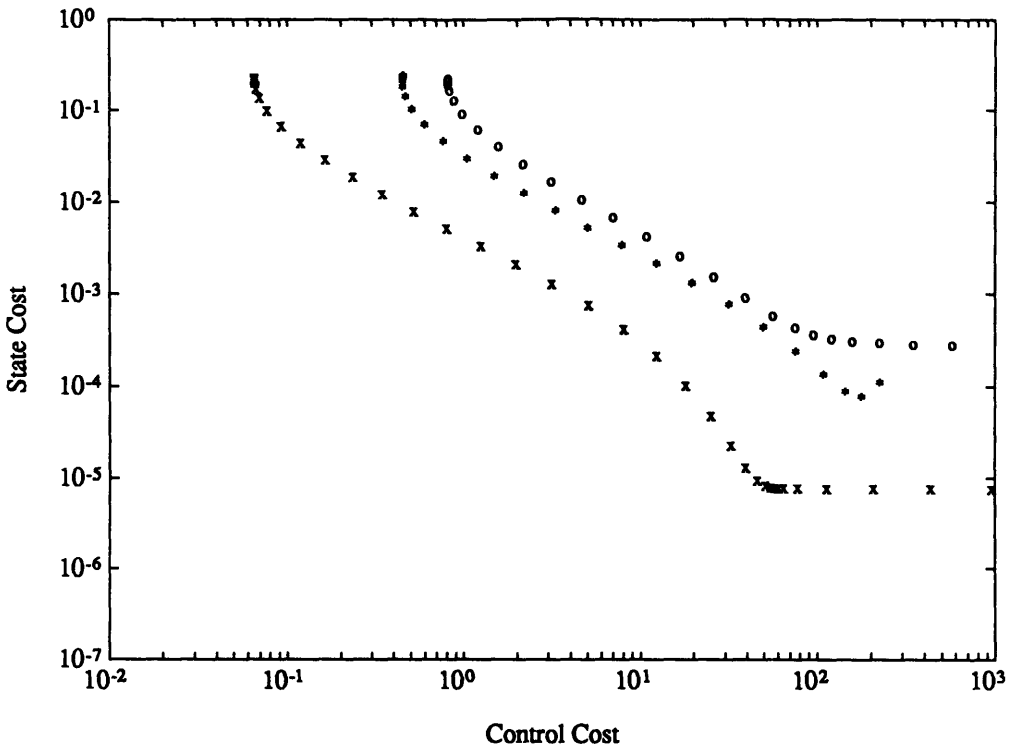

Figure 7.4 Cost curve for wing model with a taper ratio of 0.67. Fiber sweep angle is -15 degrees, geometric sweep angle is 30 degrees. Evaluated at the calculated flutter speed and frequency.

Throughout all of the analyses, the tapered wing models have behaved in a very similar manner to the non-tapered models. The natural frequencies and flutter speeds are barely affected. Likewise, the control analysis shows that the actuators have the same performance trends. Much of this similarity is due to the manner in which the taper has been introduced: by keeping the tip chord constant. Due to these results and similarity to a transport wing, a taper ratio of 0.67 will be included in the final design.

Conclusion

Chapter 8

8.1 Summary of final design

The main purpose of this study has been to understand the important issues in strain actuated aeroelastic control. In the process, a wing model has been designed for aeroelastic control wind tunnel experiments. This wing model employs both strain actuators and a conventional flap actuator. In Chapter 3, the functional requirements and design parameters for such a model have been outlined. Through a series of non-parametric and parametric studies discussed in Chapters 4 through 7, baseline design parameters have been chosen for the wing model and are summarized in Table 8.1.

Table 8.1 Baseline design parameters

Geometrical	Span (half)	51 in.
	Aspect ratio (full)	8
	Geometric sweep angle	30 deg.
	Airfoil shape	NACA 64-012
	Aerodynamic thickness ratio	12 %
	Aerodynamic taper ratio	0.67
Structural	Spar thickness ratio	2 %

	Spar taper ratio	0.67
	Laminate layup	[θ / θ / 0]s
	Fiber sweep angle	-15 deg.
	Facesheet material	AS4/3501-6
	Core material	Aluminum honeycomb
Actuation	Flap chord ratio	20 %
	Flap span ratio	20 %
	Flap location	60 % to 80 % of span
	Piezoceramic area coverage	root to 60 % of span
	Piezoceramic thickness	0.020 in. top and bottom
	Piezoceramic sectioning	root to 30 % of span
		30 % to 60 % of span

The half span refers to the unswept length of the structural box and includes the 3 in. span of the flutter stopper.

In addition to the above design parameters, a baseline design for a tip mass flutter stopper has been determined. The basic flutter stopper mechanism is a moving mass of 3.3 lbs fixed to the wing tip. Initially, the mass will be held slightly aft of the midchord. When flutter is encountered, the mass will be quickly moved to a position at the leading edge of the wing. The operating design principle uses a change in the location of the wing center of gravity to increase the flutter speed.

These studies and their results comprise the preliminary design phase of the strain actuation demonstration experiments. Understandably, in the detailed design process, these values may be slightly altered. However, to maintain design integrity and continue to satisfy the functional requirements, the design parameters shall only be incrementally changed.

8.2 Summary of Scientific Issues

Throughout the course of this design process, several important principles have been determined for strain actuated aeroelastic control. The majority of these conclusions may be grouped into the following categories: design of the passive structure, implementation of piezoelectric actuators, and design of active controllers. The remaining few are related to the flutter stopper mechanism and the addition of taper to the wing design.

The design of the passive structure with fiber and geometric sweep was addressed in Chapters 2 and 5. There are two significant, related conclusions. The first is that a model with a combination of aft geometric sweep and forward fiber sweep can be guaranteed to flutter and that the flutter speed will be robust to small changes in geometric or fiber sweep. The second is that a model with a combination of forward geometric sweep and aft fiber sweep can be guaranteed to diverge and that the divergence speed will be robust to small changes in geometric or fiber sweep. In addition, it is important to note the remarkable agreement of the simplified two mode typical section analysis with the more complicated five mode analysis and the experimental results in Landsberger and Dugundji [1985].

The next important topic is the implementation of the piezoelectric actuators which was addressed in Chapters 4 and 5. First, it has been shown that incorporating bend-twist coupling enables isotropic piezoelectric actuators to exert independent control on the torsional mode as well as the bending mode (Chapter 5). Second, the scaling study in Chapter 4 demonstrated that there is an optimal piezoelectric thickness for torsional authority. In contrast to the bending authority, where increased piezoelectric thickness always produced increased bending authority, the torsional authority reached a maximum at a piezoelectric thickness of 0.020 in.

Further increasing the piezoelectric thickness reduced the bend-twist coupling necessary for torsional control because the isotropy of the thicker piezoelectrics began to dominate the anisotropy of the laminate.

The third principle area of study was the design of aeroelastic controllers. Both the typical section analyses of Chapter 2 and the Rayleigh-Ritz analyses of Chapter 5 demonstrated several important guiding principles. Controllers using a single actuator and full state feedback were shown to have a fundamental performance limitation for high control costs. Aeroelasticity involves the interaction of two modes and a single actuator is not capable of effectively controlling both modes. Furthermore, when the system is allowed only one measurement, the performance limitation is increased. The use of multiple actuators in combination removed the performance limitation, as both modes could be independently controlled. It should be noted that, through typical section parameter variations, these results were proven to be robust to changes in the sectional properties, given that the center of gravity remains aft of the elastic axis and the elastic axis remains aft of the center of pressure.

An interesting contrast between the typical section analyses and the Rayleigh-Ritz analyses was the relative performance of the multiple actuator controllers and the single actuator controllers. The typical section's flutter mechanism was a perfect two mode coalescence. Therefore, the multiple actuator controllers performed better in both the low control cost and high control cost regions, because the single actuator controllers could not effectively control both modes, as necessary. In comparison, the wing model's flutter mechanism was dominated by the first, predominantly bending mode. Because the flutter mechanism was dominated by a single mode, the single actuators, which were able to effectively control that mode, performed as well

as the actuator combinations in the low control cost region, when control effort is "expensive." In the high control cost region, the inability of the single actuator controllers to effectively control the second mode still limits their performance.

Finally, the last two trade studies on the tip mass flutter stopper and the addition of taper to the wing provided two main conclusions. The flutter stopper trades indicated that the dominant effect on the flutter speed is the change in the wing center of gravity. The change in torsional inertia provided only a secondary increase in the flutter speed. The taper ratio study demonstrated that when the tip dimensions are held constant, the dynamics will not alter appreciably.

The primary purpose of this study was to examine the use of strain actuators in aeroelastic control. While this study, as well as previous work, establishes a solid foundation for strain actuated aeroelastic control, much work remains to be done. The strain actuated aeroelastic control technology will benefit greatly from material advances and enhanced strain capability. Along with the material advances, the use of current anisotropic strain actuators and the design of new anisotropic strain actuators to enhance torsional authority should be examined. Finally, before this technology can enter practical usage, the current demonstration phase must be brought to fruition and the technology must be further verified in a realistic monocoque wing structure.

Appendix A

Parameters for Nominal Typical Section

Section Geometry

$a = -0.2$

$x_\alpha = 0.2$

$R_\alpha^2 = 0.25$

$\mu = 20$

$\overline{\omega}_h = 0.2$

$c_\beta = 0.8$

$c_\xi = 0.8$

Aerodynamic Coefficients

$C_{L_\alpha} = 2\pi$

$C_{L_\beta} = 2.487$

$C_{L_\xi} = -0.087$

$C_{M_\alpha} = 1.885$

$C_{M_\beta} = -0.3339$

$C_{M_\xi} = -0.146$

Airfoil Parameters

$$\frac{t}{2b} = 0.01$$

$$\frac{L}{b} = 3.92$$

State and Control Weighting Matrices

$$Q = \begin{bmatrix} Q_{hh} & 0 \\ 0 & Q_{\alpha\alpha} \end{bmatrix} = \begin{bmatrix} \dfrac{1}{(0.406)^2} & 0 \\ 0 & \dfrac{1}{(0.282)^2} \end{bmatrix}$$

$$R = \begin{bmatrix} R_{hh} & 0 & 0 & 0 \\ 0 & R_{\alpha\alpha} & 0 & 0 \\ 0 & 0 & R_{\beta\beta} & 0 \\ 0 & 0 & 0 & R_{\xi\xi} \end{bmatrix} = \begin{bmatrix} \dfrac{1}{(0.0429)^2} & 0 & 0 & 0 \\ 0 & \dfrac{1}{(0.0215)^2} & 0 & 0 \\ 0 & 0 & \dfrac{1}{(0.0873)^2} & 0 \\ 0 & 0 & 0 & \dfrac{1}{(0.0436)^2} \end{bmatrix}$$

Full Equations of Motion with Unsteady Åerodynamics

$$\hat{\mathbf{M}}\dot{\mathbf{x}} + \hat{\mathbf{K}}\mathbf{x} = \hat{\mathbf{F}}\mathbf{u} + \hat{\mathbf{D}}\alpha_o$$

$$\hat{\mathbf{M}} = \begin{bmatrix} 1 & 0 & 0 & 0 & 0 & 0 & 0 & 0 & 0 \\ 0 & 1 & 0 & 0 & 0 & 0 & 0 & 0 & 0 \\ 0 & 0 & 1 & 0 & 0 & 0 & 0 & 0 & 0 \\ 0 & 0 & 0 & \frac{1}{R_\alpha^2} + \frac{\bar{q}}{U_\alpha^2} C_{L_{\ddot{h}}} & \frac{x_\alpha}{R_\alpha^2} + \frac{\bar{q}}{U_\alpha^2} C_{L_{\ddot{\alpha}}} & \frac{\bar{q}}{U_\alpha^2} C_{L_\beta} & \frac{\bar{q}}{U_\alpha} C_{L_{\dot{h}}} & \frac{\bar{q}}{U_\alpha} C_{L_{\dot{\alpha}}} & \frac{\bar{q}}{U_\alpha} C_{L_{\dot{\beta}}} \\ 0 & 0 & 0 & \frac{x_\alpha}{R_\alpha^2} - \frac{\bar{q}}{U_\alpha^2} C_{M_{\ddot{h}}} & 1 - \frac{\bar{q}}{U_\alpha^2} C_{M_{\ddot{\alpha}}} & -\frac{\bar{q}}{U_\alpha^2} C_{M_\beta} & -\frac{\bar{q}}{U_\alpha} C_{M_{\dot{h}}} & -\frac{\bar{q}}{U_\alpha} C_{M_{\dot{\alpha}}} & -\frac{\bar{q}}{U_\alpha} C_{M_{\dot{\beta}}} \\ 0 & 0 & 0 & 0 & 0 & 1 & 0 & 0 & 0 \\ 0 & 0 & 0 & 0 & 0 & 0 & 1 & 0 & 0 \\ 0 & 0 & 0 & 0 & 0 & 0 & 0 & 1 & 0 \\ 0 & 0 & 0 & 0 & 0 & 0 & 0 & 0 & 1 \end{bmatrix}$$

$$\hat{\mathbf{K}} = \begin{bmatrix} 0 & 0 & 0 & -1 & 0 & 0 & 0 & 0 & 0 \\ 0 & 0 & 0 & 0 & -1 & 0 & 0 & 0 & 0 \\ 0 & 0 & 0 & 0 & 0 & -1 & 0 & 0 & 0 \\ \frac{\bar{\omega}_h^2}{R_\alpha^2} & \bar{q} C_{L_\alpha} & \bar{q} C_{L_\beta} & \frac{\bar{q}}{U_\alpha} C_{L_{\dot{h}}} & \frac{\bar{q}}{U_\alpha} C_{L_{\dot{\alpha}}} & \frac{\bar{q}}{U_\alpha} C_{L_{\dot{\beta}}} & 0 & \bar{q} C_{L_{\dot{\alpha}}} & \bar{q} C_{L_{\dot{\beta}}} \\ 0 & 1 - \bar{q} C_{M_{\dot{\alpha}}} & -\bar{q} C_{M_\beta} & -\frac{\bar{q}}{U_\alpha} C_{M_{\dot{h}}} & -\frac{\bar{q}}{U_\alpha} C_{M_{\dot{\alpha}}} & -\frac{\bar{q}}{U_\alpha} C_{M_{\dot{\beta}}} & 0 & -\bar{q} C_{M_{\dot{\alpha}}} & -\bar{q} C_{M_{\dot{\beta}}} \\ 0 & 0 & 4900 & 0 & 0 & 98.994 & 0 & 0 & 0 \\ 0 & 0 & 0 & -1 & 0 & 0 & 0.1902 U_\alpha & 0 & 0 \\ 0 & 0 & 0 & 0 & -1 & 0 & 0 & 0.1902 U_\alpha & 0 \\ 0 & 0 & 0 & 0 & 0 & -1 & 0 & 0 & 0.1902 U_\alpha \end{bmatrix}$$

$$\hat{\mathbf{F}} = \begin{bmatrix} 0 & 0 & 0 \\ 0 & 0 & 0 \\ 0 & 0 & 0 \\ 1 & 0 & 0 \\ 0 & 1 & 0 \\ 0 & 0 & 4900 \\ 0 & 0 & 0 \\ 0 & 0 & 0 \\ 0 & 0 & 0 \end{bmatrix} \quad \hat{\mathbf{D}} = \begin{Bmatrix} 0 \\ 0 \\ 0 \\ -\bar{q} C_{L_\alpha} \\ \bar{q} C_{M_\alpha} \\ 0 \\ 0 \\ 0 \\ 0 \end{Bmatrix} \quad \mathbf{x} = \begin{Bmatrix} \bar{h} \\ \alpha \\ \beta \\ \dot{\bar{h}} \\ \dot{\alpha} \\ \dot{\beta} \\ \hat{h} \\ \hat{\alpha} \\ \hat{\beta} \end{Bmatrix} \quad \mathbf{u} = \begin{Bmatrix} u_h \\ u_\alpha \\ u_\beta \end{Bmatrix}$$

Unsteady Aerodynamic Coefficients

$$C_{L_{\frac{\dot{h}}{V}}} = \pi \qquad C_{M_{\frac{\dot{h}}{V}}} = a\pi = -0.6283$$

$$C_{L_{\dot{\alpha}}} = -\pi a = 0.6283 \qquad C_{M_{\dot{\alpha}}} = -\pi\left(\tfrac{1}{8} - a^2\right) = -0.2670$$

$$C_{L_{\beta}} = -T_1 = 0.0132 \qquad C_{M_{\beta}} = T_7 + (c-a)T_1 = -0.0087$$

$$C_{L_{\frac{h}{V}}} = 2\pi \qquad C_{M_{\frac{h}{V}}} = 2\pi\left(a + \tfrac{1}{2}\right) = 1.8850$$

$$C_{L_{\alpha}} = \pi + 2\pi\left(\frac{1}{2} - a\right) = 7.5398 \qquad C_{M_{\alpha}} = -\pi\left(\tfrac{1}{2} - a\right) + 2\pi\left(a + \tfrac{1}{2}\right)\left(\tfrac{1}{2} - a\right) = -0.8796$$

$$C_{L_{\beta}} = -T_4 + T_{11} = 0.4974 \qquad C_{M_{\beta}} = -T_1 + T_8 + (c-a)T_4 - \tfrac{1}{2}T_{11} + \left(a + \tfrac{1}{2}\right)T_{11} = -0.1583$$

$$C_{L_{\alpha}} = 2\pi \qquad C_{M_{\alpha}} = 2\pi\left(a + \tfrac{1}{2}\right) = 1.8850$$

$$C_{L_{\beta}} = 2T_{10} = 2.487 \qquad C_{M_{\beta}} = -T_4 - T_{10} + 2T_{10}\left(a + \tfrac{1}{2}\right) = -0.3339$$

$$C_{L_{\frac{\dot{h}}{V}}} = 2\pi(-0.4544) = -2.8551 \qquad C_{M_{\frac{\dot{h}}{V}}} = 2\pi\left(a + \tfrac{1}{2}\right)(-0.4544) = -0.8565$$

$$C_{L_{\dot{\alpha}}} = -0.4544 \qquad C_{M_{\dot{\alpha}}} = 2\pi\left(a + \tfrac{1}{2}\right)\left(\tfrac{1}{2} - a\right)(-0.4544) = -0.5996$$

$$C_{L_{\dot{\beta}}} = T_{11}(-0.4544) = -0.1517 \qquad C_{M_{\dot{\beta}}} = \left(a + \tfrac{1}{2}\right)T_{11}(-0.4544) = -0.0455$$

$$C_{L_{\dot{\alpha}}} = 2\pi(-0.4544) = -2.8551 \qquad C_{M_{\dot{\alpha}}} = 2\pi\left(a + \tfrac{1}{2}\right)(-0.4544) = -0.8565$$

$$C_{L_{\dot{\beta}}} = 2T_{10}(-0.4544) = -1.1301 \qquad C_{M_{\dot{\beta}}} = 2T_{10}\left(a + \tfrac{1}{2}\right)(-0.4544) = -0.3390$$

$$T_1 = -\tfrac{1}{3}\sqrt{1-c^2}\left(2 + c^2\right) + ca\cos c$$

$$T_4 = -a\cos c + c\sqrt{1-c^2}$$

$$T_7 = -\left(\tfrac{1}{8} + c^2\right)a\cos c + \tfrac{1}{8}c\sqrt{1-c^2}\left(7 + 2c^2\right)$$

$$T_8 = -\tfrac{1}{3}\sqrt{1-c^2}\left(2c^2 + 1\right) + ca\cos c$$

$$T_{10} = \sqrt{1-c^2} + a\cos c$$

$$T_{11} = (a\cos c)(1-2c) + \sqrt{1-c^2}\,(2-c)$$

$$c = c_{\beta}$$

Expressions for T's are obtained from Theodorsen and Garrick

Appendix B

Graphite/Epoxy AS1/3501-6

Property	Standard Values		"Flexural" Values	
	(N/m^2)	(lb/in^2)	(N/m^2)	(lb/in^2)
E_L	130×10^9	18.85×10^6	98×10^9	14.21×10^6
E_T	10.5×10^9	1.52×10^6	7.9×10^9	1.15×10^6
ν_{LT}	0.28	0.28	0.28	0.28
G_{LT}	6.0×10^9	0.87×10^6	5.6×10^9	0.81×10^6

Ply thickness (t_p) 0.134×10^{-3} m (5.28×10^{-3} in.)

Density (ρ_g) 1520 kg/m^3 (1.71×10^{-3} $slug/in^3$)

Graphite/Epoxy AS4/3501-6

Property	Standard Values	
	(N/m^2)	(lb/in^2)
E_L	142×10^9	20.59×10^6
E_T	9.8×10^9	1.42×10^6
ν_{LT}	0.3	0.3
G_{LT}	6.0×10^9	0.87×10^6

Ply thickness (t_p) 0.134×10^{-3} m (5.28×10^{-3} in.)

Density (ρ_g) 1530 kg/m^3 (1.72×10^{-3} $slug/in^3$)

Appendix C

Rayleigh-Ritz Assumed Modes

$$\overline{w}(\overline{x},\overline{y},t)=\sum_{i=1}^{5}\overline{\phi}_i(\overline{x})\overline{\psi}_i(\overline{y})q_i(t)$$

Mode	$\overline{\phi}_i(\overline{x})$	$\overline{\psi}_i(\overline{y})$
1	$\cosh\left(\beta_1\frac{\overline{x}}{\overline{l}}\right)-\cos\left(\beta_1\frac{\overline{x}}{\overline{l}}\right)-\sigma_1\left[\sinh\left(\beta_1\frac{\overline{x}}{\overline{l}}\right)-\sin\left(\beta_1\frac{\overline{x}}{\overline{l}}\right)\right]$	1
2	$\cosh\left(\beta_2\frac{\overline{x}}{\overline{l}}\right)-\cos\left(\beta_2\frac{\overline{x}}{\overline{l}}\right)-\sigma_2\left[\sinh\left(\beta_2\frac{\overline{x}}{\overline{l}}\right)-\sin\left(\beta_2\frac{\overline{x}}{\overline{l}}\right)\right]$	1
3	$C_{11}\cos\left(g_1\frac{\overline{x}}{\overline{l}}\right)+C_{12}\sin\left(g_1\frac{\overline{x}}{\overline{l}}\right)+C_{13}\cosh\left(f_1\frac{\overline{x}}{\overline{l}}\right)+C_{14}\sinh\left(f_1\frac{\overline{x}}{\overline{l}}\right)$	$-\frac{\overline{y}}{2\overline{b}}$
4	$C_{21}\cos\left(g_2\frac{\overline{x}}{\overline{l}}\right)+C_{22}\sin\left(g_2\frac{\overline{x}}{\overline{l}}\right)+C_{23}\cosh\left(f_2\frac{\overline{x}}{\overline{l}}\right)+C_{24}\sinh\left(f_2\frac{\overline{x}}{\overline{l}}\right)$	$-\frac{\overline{y}}{2\overline{b}}$
5	$\frac{\overline{x}}{\overline{l}}\left(1-\frac{\overline{x}}{\overline{l}}\right)$	$\cosh\lambda_1\left(\frac{\overline{y}}{2\overline{b}}+0.5\right)+\cos\lambda_1\left(\frac{\overline{y}}{2\overline{b}}+0.5\right)-\xi_1\left[\sinh\lambda_1\left(\frac{\overline{y}}{2\overline{b}}+0.5\right)+\sin\lambda_1\left(\frac{\overline{y}}{2\overline{b}}+0.5\right)\right]$

Mode Shape Constants

Bending Modes (modes 1 and 2)

$\beta_1 = 1.875104$ $\quad\quad$ $\sigma_1 = 0.734096$

$\beta_2 = 4.694091$ $\quad\quad$ $\sigma_2 = 1.018467$

Chordwise Modes (mode 5)

$\lambda_1 = 4.730041$

$\xi_1 = 0.982502$

Torsional Modes (modes 3 and 4) 3" by 12" plates

Parameter	[0/0/90]s	[15/15/0]s	[30/30/0]s	[45/45/0]s
g_1	1.8076926	1.7430329	1.6754004	1.6415197
f_1	6.9579725	9.6855170	15.776150	23.128775
C_{11}	-0.2357027	-0.1715679	-0.1048742	-0.0704409
C_{12}	0.9067800	0.9533305	0.9833190	0.9925122
C_{13}	0.2357028	0.1715679	0.1044268	0.0704409
C_{14}	-0.2355829	-0.1715640	-0.1044268	-0.0704409
g_2	5.0397936	5.0479786	4.9784612	4.9085024
f_2	8.3991159	10.782076	16.457978	23.586840
C_{21}	-0.3869624	-0.3486014	-0.2661564	-0.1953181
C_{22}	0.6450945	0.7467364	0.8772607	0.9384233
C_{23}	0.3869624	0.3496014	0.2653672	0.1952906
C_{24}	-0.3870816	-0.3496089	-0.2653672	-0.1952906

Torsional Modes (modes 3 and 4) Wing Model

Parameter	[0/0/90]s	[15/15/0]s	[30/30/0]s	[45/45/0]s
g_1	1.7841521	1.7628371	1.7005716	1.6722790
f_1	7.7841721	8.6788188	12.796221	16.246035
C_{11}	-0.2123133	-0.1911872	-0.1294523	-0.1013201
C_{12}	0.9261321	0.9411888	0.9740835	0.9843152
C_{13}	0.2123133	0.1911872	0.1294523	0.1013201
C_{14}	-0.2122718	-0.1911738	-0.1294522	-0.1013201
g_2	5.0496840	5.0521022	5.0150805	4.9730101
f_2	9.1054624	9.8862550	13.638268	16.907630
C_{21}	-0.3762331	-0.3640053	-0.3043933	-0.2597920
C_{22}	0.6785082	0.7123485	0.8277837	0.8832612
C_{23}	0.3762331	0.3640053	0.3043933	0.2597920
C_{24}	-0.3762854	-0.3640264	-0.3043936	-0.2597920

Aerodynamic Strip Theory Constants

$B_{2A} = -2\pi$
$B_{1A} = -2.2\pi$
$B_{0A} = 0$
$B_{3A} = -0.27\pi$
$B_{2C} = 0$
$B_{1C} = -1.1\pi$
$B_{0C} = 0$
$B_{3C} = -0.135\pi$

$B_{2B} = 0$
$B_{1B} = 3.1\pi$
$B_{0B} = 4\pi$
$B_{3B} = -1.675\pi$
$B_{2D} = -0.25\pi$
$B_{1D} = -0.45\pi$
$B_{0D} = 2\pi$
$B_{3D} = -0.8325\pi$

Properties and Dimensions of Wing Model

Structural Box		
Span	48 in.	1.2192 m.
Chord	12 in.	0.3048 m.
Thickness	0.24 in.	6.096×10^{-3} m
Graphite/Epoxy plates		
Thickness	0.0317 in.	0.804×10^{-3} m.
Honeycomb		
Thickness	0.177 in.	4.488×10^{-3} m.
Density	0.10×10^{-3} slug/in^3	91 kg/m^3
Modelled Stiffness:		
E	0.29×10^{6} lb/in^2	2.0×10^{9} N/m^2
ν	0.3	0.3
G	0.11×10^{6} lb/in^2	0.77×10^{9} N/m^2
Aerodynamic Shell		
Span	48 in.	1.2192 m.
Chord	15.6 in.	0.39624 m.
Thickness	0.040 in.	1.016×10^{-3}
Density	2.85×10^{-3} slug/ft^3	2540 kg/m^3
Leading edge extends past structural box		
	0.6 in.	0.01524 m.
Trailing edge extends past structural box		
	3 in.	0.0762 m.

Piezoelectric Coverage

Span	28.8 in.	0.73152 m.
Chord	12 in.	0.3048 m.
Thickness per side	0.020 in.	0.508×10^{-3} m.
Stiffness:		
E	8.7×10^{6} lb/in^2	60.0×10^{9} N/m^2
ν	0.3	0.3
G	3.2×10^{6} lb/in^2	22×10^{9} N/m^2

Piezoelectrics cover both sides of the structural box

Flap

Span	9.6 in.	0.24384 m.
Chord	3 in.	0.0762 m.

Extends from 60% to 80% of the structural box span and from the edge of the structural box to the trailing edge

Extra mass for motors, bearings, etc.

Mass	15.5×10^{-3} slugs	0.226 kg
Span	6 in.	0.1524 m.
Chord	1.5 in.	0.0381 m.

Adjacent to the immediate inboard side of the flap and to the edge of the structural box

Aeroelastic Data

Data for 3" by 12" plates. All speeds are in meters/second. All angles are in degrees

F indicates flutter, D indicates divergence.

Numbers in parantheses are flutter frequencies in Hz.

Sweep Angle	Ply Fiber Angle						
	-45	-30	-15	0	15	30	45
-30	15.7 D	34.7 D	28.4 F (26.5)	16.6 D	10.8 D	8.5 D	7.4 D
-15	34.3 F (27.9)	30.1 F (28.3)	24 F (26.7)	17.9 D	11.1 D	9 D	8.2 D
0	29.3 F (26.4)	26.9 F (28)	22.2 F (26.9)	21.1 F (23.9)	12.5 D	10.6 D	10.4 D
15	27.2 F (25.4)	26 F (27.8)	22.1 F (27.2)	21 F (23.9)	15.7 D	14.6 D	18.6 D
30	27.1 F (24.6)	26.9 F (27.6)	23.6 F (27.8)	22.5 F (24.1)	25 D	42.2 F (35.9)	38.6 F (38.2)

Data for wing model. All cases exhibit flutter first. All angles are in degrees.

All speeds are in m/s [mph].

Numbers in parantheses are flutter frequencies in Hz.

Sweep Angle	Ply Fiber Angle			
	-45	-30	-15	0
0	65.8 [147.2] (8.5)	61 [136.5] (8.2)	52 [116.3] (7.6)	49.9 [111.6] (7.2)
15	63.1 [141.2] (8.3)	58.9 [131.8] (8)	51 [114.1] (7.5)	49.1 [109.8] (7.1)
30	64.9 [145.2] (8.1)	61.3 [137.1] (7.9)	54.1 [121.0] (7.5)	52.1 [116.5] (7.1)

Appendix D

The following changes have been made for the tapered wing:

All modeshapes are defined using a reference chord length c_{ref}.

The reference chord length is taken at the 3/4 span point.

The aerodynamic forces then take the form

$$A_{2_{ij}} = \left[\bar{\gamma}_{o_{i_1}} \cdots \bar{\gamma}_{o_{i_{10}}} \bar{\alpha}_{o_{i_1}} \cdots \bar{\alpha}_{o_{i_{10}}}\right] \left[\begin{array}{ccc|ccc} \frac{b^2}{b_{ref}^2} B_{2A} \Delta x \cos\Lambda & & 0 & \frac{b^3}{b_{ref}^2} B_{2B} \Delta x \cos\Lambda & & 0 \\ & \ddots & & & \ddots & \\ 0 & & \frac{b^2}{b_{ref}^2} B_{2A} \Delta x \cos\Lambda & 0 & & \frac{b^3}{b_{ref}^2} B_{2B} \Delta x \cos\Lambda \\ \hline \frac{b^3}{b_{ref}^2} B_{2C} \Delta x \cos\Lambda & & 0 & \frac{b^4}{b_{ref}^2} B_{2D} \Delta x \cos\Lambda & & 0 \\ & \ddots & & & \ddots & \\ 0 & & \frac{b^3}{b_{ref}^2} B_{2C} \Delta x \cos\Lambda & 0 & & \frac{b^4}{b_{ref}^2} B_{2D} \Delta x \cos\Lambda \end{array}\right] \left\{\begin{array}{c} \bar{\gamma}_{o_{j_1}} \\ \vdots \\ \bar{\gamma}_{o_{j_{10}}} \\ \bar{\alpha}_{o_{j_1}} \\ \vdots \\ \bar{\alpha}_{o_{j_{10}}} \end{array}\right\}$$

$b = \frac{\bar{b}}{\cos\Lambda}$, $b_{ref} = \frac{\bar{b}_{ref}}{\cos\Lambda}$, and $\Delta x = \Delta\bar{x}\cos\Lambda$

Similar for $A_{1_{ij}}, A_{0_{ij}}, A_{3_{ij}}$

and the equations of motion are

$$\ddot{\eta}(t) + \mathbf{E}^T\mathbf{K}\mathbf{E}\eta(t) = \frac{1}{2}\rho U^2\left(\frac{b_{ref}}{U}\right)^2 \mathbf{E}^T\mathbf{A}_2\mathbf{E}\ddot{\eta}(t) + \frac{1}{2}\rho U^2\left(\frac{b_{ref}}{U}\right)\mathbf{E}^T\mathbf{A}_1\mathbf{E}\dot{\eta}(t) + \frac{1}{2}\rho U^2\mathbf{E}^T\mathbf{A}_0\mathbf{E}\eta(t) + \frac{1}{2}\rho U^2\mathbf{E}^T\mathbf{A}_3\mathbf{E}\hat{\mathbf{y}}(t)$$

$$\dot{\hat{\mathbf{y}}}(t) + 0.15\frac{U}{b_{ref}}\hat{\mathbf{y}}(t) = \dot{\eta}(t)$$

The flap forces are altered in the same manner.

Bibliography

Bisplinghoff, Raymond L., Holt Ashley, and Robert L. Halfman. *Aeroelasticity.* Reading, Massachusetts: Addison-Wesley Publishing Company, 1955.

Blevins, Robert D. *Formulas for Natural Frequency and Mode Shape.* Malabar, Florida: Robert E. Krieger Publishing Company, 1984.

Chen, Gun-Shing and John Dugundji. "Experimental Aeroelastic Behavior of Forward-Swept Graphite/Epoxy Wings with Rigid-Body Freedom." *Journal of Aircraft,* Vol. 24, No. 7, July 1987, pp 454-462.

Crawley, Edward F. and Eric H. Anderson. "Detailed Models of Piezoceramic Actuation of Beams." *Journal of Intelligent Material Systems and Structures,* Vol. 1, January 1990, pp. 4-25.

Crawley, E. F. and J. Dugundji. "Frequency Determination and Non-Dimensionalization for Composite Cantilever Plates." *Journal of Sound and Vibration,* Vol. 72, No. 1, 8 September 1980, pp. 1-10.

Crawley, E. F. and K. B. Lazarus. "Induced Strain Actuation of Isotropic and Anisotropic Plates." *AIAA Journal,* Vol. 29, No. 6, June 1991, pp. 944-951.

Ehlers, S. M. and T. A. Weisshaar. "Static Aeroelastic Behavior of an Adaptive Laminated Piezoelectric Composite Wing." AIAA Paper No. 90-1078, Proceedings of the 31st Structures, Structural Dynamics, and Materials Conference, Long Beach, CA, May 1990, pp. 1611-1623.

Heeg, Jennifer. "An Analytical and Experimental Investigation of Flutter Suppression via Piezoelectric Actuation." AIAA Paper No. 92-2106, Proceedings of the AIAA Dynamics Specialists Conference, Dallas, TX, April 1992, pp. 237-247.

Hollowell, Steven J. and John Dugundji. "Aeroelastic Flutter and Divergence of Stiffness Coupled, Graphite/Epoxy, Cantilevered Plates." *Journal of Aircraft,* Vol. 21, January 1984, pp. 69-76.

Hwang, C., et al. "Wind Tunnel Test of a Fighter Aircraft Wing/Store Flutter Suppression System - An International Effort." AGARD-R-689, April 1980.

Hwang, C., E. H. Johnson, and W. S. Pi. "Recent Development of the YF-17 Active Flutter Suppression System." *Journal of Aircraft,* Vol. 18, No. 7, July 1981, pp. 537-545.

Jane's All the World's Aircraft 1991-92. Jane's Information Group. London, England: Butler & Tanner Ltd., 1991.

Jensen, D. W., E. F. Crawley, and J. Dugundji. "Vibration of Cantilevered Graphite/Epoxy Plates with Bending-Torsion Coupling." *Journal of Reinforced Plastics and Composites,* Vol. 1, July 1982, pp. 254-269.

Jones, Robert M. *Mechanics of Composite Materials.* New York: Hemisphere Publishing Corporation, 1975.

Kuethe, Arnold M. and Chuen-Yen Chow. *Foundations of Aerodynamics: Bases of Aerodynamic Design.* New York: John Wiley & Sons, 1986.

Kwakernaak, Huibert and Raphael Sivan. *Linear Optimal Control Systems.* New York: Wiley-Interscience, 1972.

Landsberger, Brian J. and John Dugundji. "Experimental Aeroelastic Behavior of Unswept and Forward-Swept Cantilever Graphite/Epoxy Wings." *Journal of Aircraft,* Vol. 22, No. 8, August 1985, pp 679-686.

Langley Working Paper 799 [LWP-799]. "The Langley Transonic Dynamics Tunnel." NASA Langley Research Center, Hampton, VA, September 23, 1969.

Lazarus, Kenneth B. and Edward F. Crawley. "Induced Strain Actuation of Composite Plates." GTL Report # 197, Massachusetts Institute of Technology, Cambridge, MA, 1989.

Lazarus, Kenneth B. and Edward F. Crawley. "Multivariable High-Authority Control of Plate-Like Active Lifting Surfaces." SERC Report # 14-92, Massachusetts Institute of Technology, Cambridge, MA, June 1992a.

Lazarus, Kenneth B. and Edward F. Crawley. "Multivariable High-Authority Control of Plate-Like Active Structures." AIAA Paper No. 92-2529, Proceedings of the 33rd SDM Conference, Dallas, TX, April 1992b.

Langley Handbook [LHB 1710.15]. "Wind-Tunnel Model Systems Criteria." NASA Langley Research Center, Hampton, VA, May 1992.

Meirovitch, Leonard. *Elements of Vibration Analysis.* New York: McGraw-Hill Book Company, 1986.

Perry, Boyd III, et al. "Digital-Flutter-Suppression-System Investigations for the Active Flexible Wing Wind-Tunnel Model" AIAA Paper No. 90-1074, Proceedings of the 31st Structures, Structural Dynamics, and Materials Conference, Long Beach, CA, May 1990, pp. 1571-1581.

Sandford, Maynard C., Irving Abel, and David L. Gray. "Development and Demonstration of a Flutter Suppression System Using Active Controls." NASA TR R-450, December 1975.

Shirk, Michael H., Terrence J. Hertz, and Terrence A. Weisshaar. "Aeroelastic Tailoring - Theory, Practice, and Promise." *Journal of Aircraft,* Vol. 23, No. 1, January 1986, pp. 6-18.

Suh, Nam P. *The Principles of Design.* New York: Oxford University Press, 1990.

Theodorsen, Theodore. "General Theory of Aerodynamic Instability and the Mechanism of Flutter." NACA Report No. 496, 1935.

Theodorsen, Theodore and I. E. Garrick. "Nonstationary Flow about a Wing-Aileron-Tab Combination Including Aerodynamic Balance." NACA Report No. 736, 1942.

Weisshaar, Terrence A. and Brian L. Foist. "Vibration Tailoring of Advanced Composite Lifting Surfaces." *Journal of Aircraft,* Vol. 22, No. 2, February 1985, pp. 141-147.